DEVELOPMENT OF THREE-DIMENSIONAL FLOW MODEL CONSIDERING SURFACE AND SEEPAGE FLOWS IN A GENERALIZED CURVILINEAR COORDINATE SYSTEM AND ITS APPLICATION IN HYDRAULIC ENGINEERING

QIYUN PANG

2024

Abstract

This comprehensive research endeavor advances the field of hydraulic modeling by introducing a sophisticated three-dimensional computational fluid dynamics model, aiming to substantially improve the predictive understanding of river flow behavior and its consequential effects on levee stability and morphological changes of riverbeds. Recognizing rivers as a vital component that have continuously shaped both natural ecosystems and human civilization, the study underscores the intricate nature of river flow systems, whose influences span from providing essential water resources to posing severe flood risks and contributing to environmental contamination issues. Considering the inadequacies observed in conventional modeling techniques, this investigation integrates a refined Reynolds-averaged Navier-Stokes (RANS) methodology with a nonlinear $k-\varepsilon$ turbulence model, operating within a curvilinear coordinate system. This approach is meticulously engineered to decode the complex three-dimensional flow patterns present in riverine environments.

The dissertation unfolds systematically across a series of six chapters. The Chapter 1 lays the foundational context, underscoring the critical demand for advanced tools capable of enhancing flood defense mechanisms and enriching disaster management resources. In Chapter 2, the exposition of the numerical techniques that construct the core of the model, articulating the formulations of coordinate transformations and tensor analysis, which converge to facilitate a rigorous derivation of the governing Navier-Stokes equations in a curvilinear coordinate system. Chapter 3 is devoted to the application to the open channel flows with side weir of the model, evaluating its performance against established benchmarks, including the simulation of secondary flow phenomena within river bends. Chapters 4 and 5 explore the extension of the model to simulate surface and seepage flows, drawing upon dam-break flow over permeable porous beds to check the model's robustness. Additionally, these chapters incorporate sediment transport dynamics into the numerical model, allowing for the prediction of riverbed evolution in response to fluid movement a critical component for understanding and managing sediment erosion, deposition, and overall geomorphology. Chapter 6 concludes the document throughout the study. It affirms the sophisticated model's proficiency in not just elevating the accuracy of flood risk appraisals but also in offering

tangible enhancements to the practices of river management. The shift from two-dimensional analyses to a more intricate three-dimensional simulation presents a significant advancement.

Acknowledgments

Time flies fast, and as the years flow like a river, I find myself spending six years living and studying in Japan. The completion of this thesis would not have been possible without the assistance and support of many individuals. I extend my deepest apologies to those whom I may have inadvertently failed to acknowledge.

First and foremost, I express my heartfelt gratitude to my supervisor, Associate Professor Dr. **Shinichiro Onda**. Throughout the three and a half years of my doctoral program, Onda sensei has not only guided my research and thesis writing with utmost care and responsibility but also meticulously reviewed and revised each paper I published. In daily research activities, Onda-sensei patiently addressed every query I raised, provided relevant materials, and figured out many significant details in learning and working that I had previously overlooked. It is through Onda-sensei's guidance that I was able to complete this study and gradually become an independent researcher. Onda-sensei is the most appreciated and important person in my academic journey.

Next, I wish to extend my thanks to Emeritus Professor Dr. **Takashi Hosoda**, now retired. Upon my arrival in Japan, Hosoda-sensei warmly led us, three international students from the lab, on a visit to the Lake Biwa Canal Museum in Kyoto and the water engineering facilities near Nanzen-ji Temple. During my master's program, Hosoda-sensei offered immense academic guidance and support in my personal life in Japan.

My special thanks go to my examiners, Professor Dr. **Hitoshi Gotoh**, Professor Dr. **Eiji Harada** and Professor Dr. **Michio Sanjou** for their valuable discussions and suggestions.

I also wish to acknowledge my senior and colleagues from my master's program, Mr. **Feng Ye**, Mr. **Shotaro Kurita**, and Mr. **Masaharu Yasuba**. When I first arrived in Japan, they warmly introduced me to life in Japan, taught me much about the Japanese spoken in Kansai, and helped me gain an initial understanding of life in Japan.

I also appreciate to Mr. **Naoto Komori**, the laboratory technician, who greatly assisted me in hydraulic experiments. He not only explained many technical terms in Chinese but also significantly aided my Japanese learning.

Lastly, I express my sincere gratitude to my parents, Mr. **Pang Jun** and Mrs. **Wang Li.** Without their support and encouragement, it would have been impossible for me to complete my studies alone in a foreign land. I am also profoundly thankful to my wife **Siqi Du**, who has been my constant companion, providing immense emotional support at every moment.

Table of Contents

Chapter 6 Conclusions

List of Figures

List of Tables

Chapter 1

Introduction

1.1 Background

Historically, rivers, as natural watercourses, have been intricately woven into the tapestry of human civilization's evolution. From the Nile in ancient Egypt to the Yellow River in China, the presence of rivers has not only nourished local civilizations but has also conferred countless benefits upon humanity. These rivers, whether vast or modest, have irrigated our farmlands, supplied potable water to our cities, facilitated transportation and communication, and even emerged as cradles of culture and religion. Rivers also play a pivotal role in ecosystems, offering habitats for a myriad of species.

Beyond these apparent advantages, rivers have also endowed societies with abundant water resources, serving as the lifeblood of agriculture, industry, and daily life. The waters of these rivers breathe life into countless ecosystems, from estuarine wetlands to the high mountains at their sources, providing sanctuaries for countless organisms on our planet.

However, besides the great benefits rivers bring, they also present many challenges and threats. Historically, river disasters have caused countless serious disasters. For example:

(1) Floods and droughts

Floods and droughts represent two of the most destructive river-related natural phenomena on a global scale, exerting extensive and profound impacts on human life and the environment. Floods can result in loss of life, damage, or destruction of infrastructure, stalling of economic activities, and bring long-term socio-economic challenges. They may also lead to the contamination of drinking water sources, triggering public health crises and adversely affecting the mental health of survivors. Furthermore, floods can have severe environmental consequences, including soil erosion and ecosystem degradation. Conversely, droughts lead to water scarcity, posing threats to human survival and agricultural productivity, thereby impacting food security and economic stability. Droughts can also result in the decline of ecosystem services and loss of biodiversity.

(2) Sediment transport and water pollution

Humanity has utilized the patterns of sediment transport in meandering rivers long time ago, drawing water from concave banks and sand from convex ones. However, with the advancement of human society and the expansion of industrial and agricultural activities, the pollutants in these processes have markedly increased. Sediments frequently serve as carriers for a variety of contaminants, including heavy metals, pesticides, and organic compounds. These contaminants can adhere to sediment particles and be transported in significant distances. When such sediments are disturbed or resuspended, the pollutants may be released into the river, posing a substantial risk to water quality. Moreover, these pollutants can enter the food chain, affecting the entire riverine ecosystem's health.

(3) Impact of river sediment transport on hydraulic engineering

Erosion near riverbanks can undermine flood control facilities such as embankments and levees, leading to their collapse and other hazardous situations. The scouring and deposition of riverbeds, along with the meandering of channels, can adversely affect the normal use and safety of bridges. Scouring can expose the foundations of bridge piers, compromising structural integrity, while sedimentation can reduce the clearance height beneath bridge decks. Changes in the river channel may also result in bridge instability. In meandering rivers, the angle between the direction of the water flow velocity and the perpendicular to the bridge axis can create navigational challenges. If the flow velocity within the navigation channel is too great or the angle too sharp, vessels may struggle to control their direction in time to avoid collision with bridge piers.

The impact of rivers on human societies extends far beyond what has been mentioned. To analyze and predict these effects accurately, a correct understanding and effective forecasting of the flow structure, material transport, and channel evolution are essential. Centuries of research have yielded significant insights into the structure of flows in curved channel and the bed deformation of meandering rivers, developing numerous theories, experimental methods, and numerical approaches. However, theoretical, and experimental studies often focus on the simple scenarios, such as single bends, while the conditions and limitations of widely used numerical methods can be easily overlooked.

When the geometry of a bend becomes complex, the flow structure may be significantly more intricate than that within a simple bend, a phenomenon that has been confirmed in some experiments. Yet, many related issues remain to be further investigated, such as how the flow structure in the meandering channels varies compared to the flow around a single bend. The complexity of the flow structure is a primary driver for the complex evolution of river channels. Furthermore, the complexity of channel evolution arises from the diversity in physical properties of sediments, leading to variations in density, and settling, as well as from anthropogenic influences.

Presently, theoretical analyses based on single-bend geometry, numerical models of fluid motion calibrated with simple flow fields, sediment transport and riverbed evolution models grounded on conventional sediment motion, and meander analysis models predicated on idealized channels must all undergo rigorous new testing when applied to complex natural conditions characterized by continuous bends, fine sediment transport, and human-induced constraints. Improvements or even complete reconstructions may be necessary. Therefore, research into the flow structure and channel evolution of meandering rivers under complex conditions and the sediment transport process is not only necessary but critical for advancing our understanding and management of these dynamic natural systems. To adeptly deal with these challenges, engineers and scientists across generations have conducted on extensive research and practical endeavors.

1.2 Three-dimensional simulations for open channel flows

The open channel flow in natural rivers is predominantly turbulent, exhibiting unsteady and three-dimensional characteristics with physical parameters such as velocity and pressure undergoing stochastic variations in time and space. Despite the complexity of turbulent motions, the unsteady Navier-Stokes equations remain applicable for the instantaneous behavior of turbulence. In early research, simplifications were often made by introducing certain assumptions and neglecting minor factors, reducing the problem to one-dimensional or two-dimensional flow for solution, for instance, the shallow water equations. With the continuous advancement in computational capabilities, three-dimensional numerical simulation has become an essential technical approach for studying hydrodynamics.

Currently, the primary numerical simulation methods for the turbulent flow include

the following three approaches:

(1) DNS, Direct Numerical Simulation

A direct numerical simulation (DNS) is a simulation in which the Navier–Stokes equations are numerically solved without any turbulence model[1)]. The advantage of DNS is its minimal error, but a significant drawback is the high computational costs. DNS requires a computational grid with resolution equal to or finer than the scale of the smallest eddies. For instance, within a flow region measuring 0.1 by 0.1 square meters, representing all scales of eddies in high Reynolds number turbulence could necessitate a grid with between 10^9 and 10^{12} nodes. With current computing capabilities, DNS is more commonly utilized for studying fundamental theories of fluid dynamics under low Reynolds numbers and ideal boundary conditions, rather than practical engineering computations.

(2) LES, Large Eddy Simulation[2)]

In turbulent flows, alongside the presence of numerous small-scale eddies characterized by significant randomness, there exists a well-developed of large-scale eddies. The small-scale turbulent motions are minimally influenced by flow boundary conditions and are approximately isotropic. The bulk of mass, momentum, or energy transport within the flow predominantly comes from the motion of these larger eddies. Consequently, if the dynamics of eddies larger than the computational grid are directly computed through numerical solutions, while the effects of smaller eddies below the grid scale are represented using turbulence models, the computation provided by the model occupies only a minor fraction of the overall simulation. This approach minimizes the final result's dependence on the turbulence model, thereby enhancing computational accuracy. This concept underpins the fundamental principle of Large Eddy Simulation. In applying LES to open channel turbulent flows, Booij[3)] conducted an LES study of flow within a mild curved open channel and successfully replicated the secondary currents of the second kind, which are induced by the anisotropy of turbulence[4)].

Similar to DNS, LES is constrained by current computational capabilities. As a result, the work in the domain of LES is relatively limited and primarily focused on fundamental research. Consequently, LES has not yet reached a practical stage for routine application in engineering computations.

(3) RANS, Reynolds-averaged Navier–Stokes equations

The Reynolds averaging approach involves time-averaging of the unsteady Navier-Stokes equations, resulting in a set of unclosed equations characterized by time-averaged physical quantities and the time-averaged products of fluctuating quantities, such as Reynolds Stress. Closure of the system is achieved by introducing additional equations that describe the time-averaged products of fluctuating quantities, which, in conjunction with the time-averaged N-S equations, comprise a closed set of equations that describe turbulent motion.

The most representative is the standard $k-\varepsilon$ model, which is now widely employed across various models and simulations. Nevertheless, given that the standard $k-\varepsilon$ model does not account for the anisotropy of turbulence, Kimura et al. [5), 6)] have demonstrated that only non-linear models are capable of capturing the outer-bank cell and accurately reproducing velocity and Reynolds stress profiles in curved open channel flows.

The aforementioned analysis reveals that the primary difficulties associated with both LES and DNS are not only due to computational limitations, but also stem from inherent issues within the methods themselves. Under current computational speeds, it is unlikely that the complex and large flow problems in engineering will be solved using these methods in a short term. Given that solving the Reynolds-averaged Navier-Stokes equations usually suffice for the precision required in practical applications, and considering that the primary goal of this study is practical application, this study will predominantly focus on the analysis and research of numerical simulations based on the RANS equations with a non-linear $k-\varepsilon$ model.

1.3 Sediment transport models

Within the current sediment transport models, two-dimensional flow models coupled with the sediment transport model are the most widely utilized. These models have successfully simulated a variety of riverbed alteration phenomena, such as the formation of sandbars in meandering channels[7)] and the breach of dike[8), 9)]. However, two-dimensional flow models face challenges in capturing the intricacies of three-dimensional flow structures, such as secondary currents in bends. These structures arise not only from

the curvature of the channel but also interact with upstream secondary flows to form more complex flow dynamics. Such interactions can significantly influence riverbed changes.

Hence, the development of three-dimensional flow model with sediment transport models that more accurately reflect real-world conditions is necessitated. With advancements in computational technology, the application of three-dimensional models has become possible and represents a trend in the evolution of mathematical models. Furthermore, despite the current computational inefficiency and time-consuming nature of three-dimensional models, investigating effective methods to enhance computational efficiency holds significant practical importance for advancing the development and application of three-dimensional numerical simulations of river channel evolution.

1.4 Research content and objectives

To more precisely simulate and predict river flow dynamics, as well as to probe into the mechanisms of levee failures and riverbed deformation, this study introduces a three-dimensional RANS flow model with sediment transport model using a general curvilinear coordinate system. The inception of this model seeks to address the limitations of traditional two-dimensional models under intricate terrains and flow regimes.

The utilization of the general curvilinear coordinate system aims to closely mirror the actual contours of river channels, thereby bolstering the model's accuracy and reliability. Grounded in this coordinate system, this model can not only depict the three-dimensional dynamics of rivers with precision but also possesses the capability to simulate secondary flows in bends, transverse flow phenomena, and riverbed deformation.

Specifically, this paper is structured into six chapters:

Chapter 2: Numerical Methods - This chapter offers an in-depth exploration of the mathematical methodologies employed in the model, encompassing coordinate transformations, various tensor differential operations, and the derivation of the Navier-Stokes equations within the generalized curvilinear coordinate system. Additionally, it elucidates key techniques such as the pressure correction algorithm, interface capture algorithm, and boundary condition settings.

Chapter 3: Model Application - The model is initially applied to simulate side weir flow phenomena in a straight and a curved channel, aiming to study the complex flow

characteristics around the side weir and the impact of side weir flow on secondary flows in curved channel, further validating the model's reliability.

Chapter 4: Model Extension - By integrating the porous medium method, this chapter broadens the model's applicability, enabling it to simulate both surface and seepage flows. The focus is on simulating dam-break flows over porous riverbeds and simulations with suction riverbeds, validating the model's accuracy in simulating surface and seepage flows.

Chapter 5: Further Model Extension - In this chapter, the model is further augmented with a sediment transport model, enabling it to simulate riverbed deformation, sandbar formations, and dike breaching problem. By comparing simulation results with experimental data, the model's efficacy is validated.

Chapter 6: Finally, conclusions and some recommendations are made in this chapter.

Figure 1.1 illustrates the summary of each chapter.

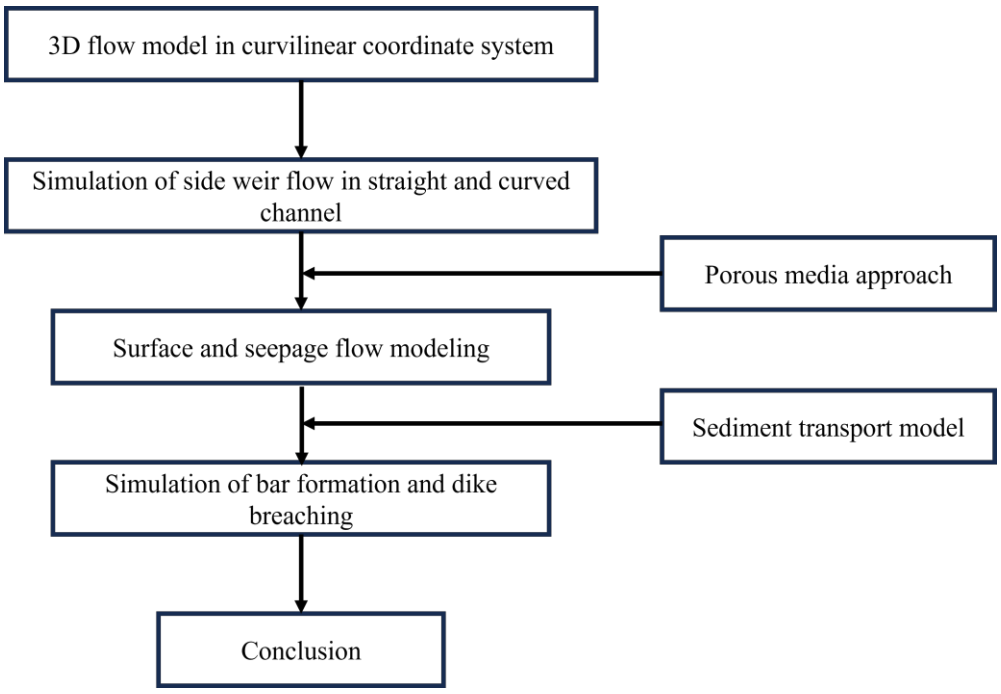

Figure 1.1 Flow chart of the study

Reference

1) Orszag, S. A. : Analytical theories of turbulence. *Journal of Fluid Mechanics*. Vol. 41, No. 2, pp. 363-386, 1970.
2) Deardorff, J. W. : A numerical study of three-dimensional turbulent channel flow at large Reynolds numbers, *Journal of Fluid Mechanics*, Vol.41, No. 2, pp. 453-480, 1970.
3) Booij, R. : Measurements and large eddy simulations of the flows in some curved flumes, *Journal of Turbulence*, Vol. 4, No. 1, pp.1-17, 2003.
4) Christensen, B., Gislason, K. and Fredsoe, J. : Secondary turbulent flow in an infinite bend, *1st RCEM Symp.*, Genova, Italy, vol. 1, pp. 543-553, 1999.
5) Kimura, I. and Hosoda, T. : A non-linear $k-\varepsilon$ model with realizability for prediction of flows around bluff bodies, *International Journal for Numerical Methods in Fluids*, Vol. 42, No. 8, pp. 813-837, 2003.
6) Kimura, I., Uijttewaal, W. S. J., Hosoda, T. and Balen, W. A. : RANS computations of mild curved open channel flows focusing on an outer-bank cell, *Proceedings of hydraulic engineering*, Vol. 52, pp. 1009-1014, 2008. (in Japanese)
7) Nishimoto, N., Shimizu, Y. and Aoki, K. : Numerical simulation of bed variation considering the curvature of stream line in a meandering channel, *Japanese Journal of JSCE*, Vol.1992, Vol. 456, pp. 11-20, 1992. (in Japanese)
8) Mizutani, H., Nakagawa, H., Yoden, T., Kawaike, K. and Zhang, H. : Numerical modelling of river embankment failure due to overtopping flow considering infiltration effects, *Journal of Hydraulic Research*, IAHR, Vol. 51, No. 6, pp. 681-695, 2013.
9) Kakinuma, T. and Shimizu, Y. : Large-scale experiment and numerical modeling of a riverine levee breach, *Journal of Hydraulic Engineering*, ASCE, Vol. 140, No. 9, pp. 1-9, 2014.

Chapter 2

Governing equations of a 3D numerical flow model in the generalized curvilinear coordinate system

2.1 Preliminaries

In natural river channels, the river flow dynamics predominantly show three-dimensional characteristics. Consequently, the most precise representation of the river flow should be approached through three-dimensional simulations. Moreover, natural river channels are almost sinuous and meandering. Using rectangular grids to mesh such channels requires an extra number of grids to approximate the channel boundaries, leading to increased computational costs and necessitating special treatment for boundary conditions. On the other hand, the use of a moving generalized curvilinear coordinate system has also been extensively employed in open channel flow simulations. This approach, which represents the motion of the free surface through the movement of the grid, can yield satisfactory simulation results[1), 2)]. However, this method is only suitable for flows where the liquid surface undergoes mild changes. In cases of intense flow variations accompanied by various air bubbles, such as hydraulic jumps, overflows, and other complex flow phenomena, it is not feasible to represent the phase interface only through grid movement. Therefore, to simulate sophisticate flow phenomena, the density function method is applied to capture the interface between air and water in this study.

Therefore, a 3D model based on the generalized curvilinear coordinate system with interface capturing method is employed in this study. In this chapter, a comprehensive exposition of the 3D numerical model for multi-phase flow is presented below.

2.2 Coordinate transformation

2.2.1 Coordinate definition

In this numerical model, the coordinate transformation is performed between the Cartesian coordinate system and the curvilinear coordinate system. Assumed that (x, y, z) is the Cartesian coordinate system (physical space), and the curvilinear coordinates (computational space) can be defined as:

$$\xi^i = \xi^i(x, y, z), \qquad (i = 1,2,3) \tag{2.1}$$

According to the chain rule, the coordinate transformation between the curvilinear coordinate system and the Cartesian coordinate system is expressed as:

$$\frac{\partial}{\partial \xi^i} = \frac{\partial x^j}{\partial \xi^i}\frac{\partial}{\partial x^j}, \qquad \frac{\partial}{\partial x^i} = \frac{\partial \xi^j}{\partial x^i}\frac{\partial}{\partial \xi^j} \tag{2.2}$$

Therefore, the $d\xi^i$ and dx^i has the following transformation:

$$d\xi^j = \frac{\partial \xi^j}{\partial x^i}\, dx^i \tag{2.3}$$

$\left[\frac{\partial \xi^j}{\partial x^i}\right]$ is the transformation matrix and its determinate J is expressed as:

$$J = \left|\frac{\partial \xi^j}{\partial x^i}\right| = \begin{vmatrix} \frac{\partial \xi^1}{\partial x^1} & \frac{\partial \xi^2}{\partial x^1} & \frac{\partial \xi^3}{\partial x^1} \\ \frac{\partial \xi^1}{\partial x^2} & \frac{\partial \xi^2}{\partial x^2} & \frac{\partial \xi^3}{\partial x^2} \\ \frac{\partial \xi^1}{\partial x^3} & \frac{\partial \xi^2}{\partial x^3} & \frac{\partial \xi^3}{\partial x^3} \end{vmatrix} \tag{2.4}$$

J is called Jacobian and represents the ratio of the volume of the cell between the curvilinear coordinate system and the Cartesian coordinate system.

2.2.2 Dual basis vector in curvilinear coordinate system

In three-dimensional space, two pairs of the basis vectors called the dual basis vector are usually utilized in a curvilinear coordinate system. Firstly, assuming a vector $\boldsymbol{r}(\xi^i)$, the covariant basis vector $\boldsymbol{e}_i$ can be defined as:

$$\boldsymbol{e}_i = \frac{\partial \boldsymbol{r}}{\partial \xi^i} \tag{2.5}$$

Obviously, $\boldsymbol{e}_i$ is tangent to ξ^i coordinate and then computing the volume of

the hexahedron $\sqrt{g}$ formed by these three basis vectors, the expression is as follows:

$$\sqrt{g} = \boldsymbol{e}_1 \cdot (\boldsymbol{e}_2 \times \boldsymbol{e}_3) \tag{2.6}$$

where g is the determinate of metric tensor and is expressed in Chapter 2.2.3.

According to equation (2.5), contravariant basis vector $\boldsymbol{e}^i$ can be defined as:

$$\boldsymbol{e}^1 = \frac{1}{\sqrt{g}}(\boldsymbol{e}_2 \times \boldsymbol{e}_3), \boldsymbol{e}^2 = \frac{1}{\sqrt{g}}(\boldsymbol{e}_3 \times \boldsymbol{e}_1), \boldsymbol{e}^3 = \frac{1}{\sqrt{g}}(\boldsymbol{e}_1 \times \boldsymbol{e}_2) \tag{2.7}$$

Through equation (2.4) and (2.5), the relationship between $\boldsymbol{e}^i$ and $\boldsymbol{e}_j$ can easily be concluded as:

$$\boldsymbol{e}^i \cdot \boldsymbol{e}_j = \delta^i{}_j = \begin{cases} 1, & i = j \\ 0, & i \neq j \end{cases} \tag{2.8}$$

where $\delta^i{}_j$ is Kronecker delta.

2.2.3 Metric tensor

Metric tensor $\boldsymbol{g}$ is defined by the dual basis vector $\boldsymbol{e}^i$ and $\boldsymbol{e}_j$, and can be written as:

$$\begin{gathered} \boldsymbol{g} = g_{ij}\boldsymbol{e}^i\boldsymbol{e}^j = g^{ij}\boldsymbol{e}_i\boldsymbol{e}_j \\ g_{ij} = \boldsymbol{e}_i \cdot \boldsymbol{e}_j = g_{ji} \\ g^{ij} = \boldsymbol{e}^i \cdot \boldsymbol{e}^j = g^{ji} \\ g = \det[g^{ij}] \end{gathered} \tag{2.9}$$

where g^{ij}, g_{ij}: contravariant components and covariant components of metric tensor, respectively.

Metric tensor $\boldsymbol{g}$ dictates the geometric properties of the space and provides the information how to measure spatial distance as well as areas, volumes, etc. For instance, the "square of the length ds" of an infinitesimal displacement $d\boldsymbol{r}(= \boldsymbol{e_i} d\xi^i)$ in a curvilinear coordinate system can be expressed as:

$$ds^2 = d\boldsymbol{r} \cdot d\boldsymbol{r} = g_{ij} d\xi^i d\xi^j \tag{2.10}$$

As an example, in the three-dimensional space with Cartesian coordinate system, because g_{ij} is equal to δ_{ij}, the line element ds is

$$\begin{aligned} ds^2 &= \delta_{ij} dx^i dx^j = dx^i dx^i \\ &= (dx)^2 + (dy)^2 + (dz)^2 \end{aligned} \tag{2.11}$$

Therefore, the length, area, and volume of the infinitesimal element within the curvilinear coordinate system $\xi^i(x^i)$ can be easily expressed using metric tensor as:

infinitesimal displacement $d\boldsymbol{s}_i$ and its magnitude ds_i

$$\begin{cases} d\boldsymbol{s}_1 = \boldsymbol{e_1} d\xi^1 \\ d\boldsymbol{s}_2 = \boldsymbol{e_2} d\xi^2, \\ d\boldsymbol{s}_3 = \boldsymbol{e_3} d\xi^3 \end{cases} \qquad \begin{cases} ds_1 = \sqrt{g_{11}} d\xi^1 \\ ds_2 = \sqrt{g_{22}} d\xi^2 \\ ds_3 = \sqrt{g_{33}} d\xi^3 \end{cases} \tag{2.12}$$

normal vector $d\boldsymbol{a}_i$ and its magnitude da_i

$$\begin{cases} d\boldsymbol{a}_1 = d\boldsymbol{s}_2 \times d\boldsymbol{s}_3 = \sqrt{g} d\xi^2 d\xi^3 \boldsymbol{e}^1 \\ d\boldsymbol{a}_2 = d\boldsymbol{s}_3 \times d\boldsymbol{s}_1 = \sqrt{g} d\xi^1 d\xi^3 \boldsymbol{e}^2 \\ d\boldsymbol{a}_3 = d\boldsymbol{s}_1 \times d\boldsymbol{s}_2 = \sqrt{g} d\xi^1 d\xi^2 \boldsymbol{e}^3 \end{cases}$$

$$\begin{cases} da_1 = \sqrt{g}\sqrt{g^{11}} d\xi^2 d\xi^3 = \sqrt{g_{22}g_{33} - {g_{23}}^2} d\xi^2 d\xi^3 \\ da_2 = \sqrt{g}\sqrt{g^{22}} d\xi^1 d\xi^3 = \sqrt{g_{11}g_{33} - {g_{13}}^2} d\xi^1 d\xi^3 \\ da_3 = \sqrt{g}\sqrt{g^{33}} d\xi^1 d\xi^2 = \sqrt{g_{11}g_{22} - {g_{12}}^2} d\xi^1 d\xi^2 \end{cases} \tag{2.13}$$

volume element $d\sigma$

$$d\sigma = d\boldsymbol{s}_1 \cdot (d\boldsymbol{s}_2 \times d\boldsymbol{s}_3) = \sqrt{g} d\xi^1 d\xi^2 d\xi^3 \tag{2.14}$$

From the aforementioned discussion, a metric defines a specific geometry, particularly in terms of prescribing measurements for distances. However, different metrics can indeed delineate the same geometry, especially those metrics interconnected through coordinate transformations. Importantly, the determination of distances should remain invariant regardless of the chosen coordinate system. Hence, in this numerical model, changing coordinates from the Cartesian coordinate system (x^i) to the curvilinear coordinate system $\xi^i(x^i)$ demanding that

$$g_{ij} d\xi^i d\xi^j = \delta_{kl} dx^k dx^l \tag{2.15}$$

It is observed that, under a coordinate transformation, a metric undergoes a transformation as follows:

$$\begin{aligned} g_{ij}(x) &= \delta_{kl}(\xi) \frac{\partial x^k}{\partial \xi^i} \frac{\partial x^l}{\partial \xi^j} \\ g^{ij}(x) &= \delta^{kl}(\xi) \frac{\partial \xi^i}{\partial x^k} \frac{\partial \xi^j}{\partial x^l} \end{aligned} \tag{2.16}$$

During simulation computations, the nodes in the Cartesian coordinate system are known. Consequently, the value of g_{ij} can be computed using finite differential methods per equation (2.17). Once the value of g_{ij} is obtained, Equation (2.13), (2.14), and (2.15) can be employed to determine attributes such as the lengths, areas, and volumes

of the control volume in the curvilinear coordinate system, which facilitates the calculation of physical fluxes cross the control volume.

2.2.4 Form of Nabla operator in the curvilinear coordinate system

In the curvilinear coordinate system, Nabla operator is defined as:

$$\nabla = \boldsymbol{e}^i \frac{\partial}{\partial \xi^i} \tag{2.17}$$

(1) Gradient of scaler, vector and tensor

Obviously, the gradient of a scaler φ is

$$\nabla\varphi = \boldsymbol{e}^i \frac{\partial \varphi}{\partial \xi^i} \tag{2.18}$$

$\nabla\varphi$ is a vector, and $\frac{\partial \varphi}{\partial \xi^i}$ are the covariant components of $\nabla\varphi$.

Before delving into the expression for the gradient of a vector $\nabla \boldsymbol{V}$, firstly examine the formulation for a vector differentiation $\frac{\partial \boldsymbol{V}}{\partial \xi^j}$. According to the Leibniz rule, $\frac{\partial \boldsymbol{V}}{\partial \xi^j}$ is expressed as:

$$\frac{\partial \boldsymbol{V}}{\partial \xi^j} = \frac{\partial}{\partial \xi^j}\left(V^i \boldsymbol{e}_i\right) = \boldsymbol{e}_i \frac{\partial V^i}{\partial \xi^j} + V^i \frac{\partial \boldsymbol{e}_i}{\partial \xi^j} \tag{2.19}$$

where $\frac{\partial \boldsymbol{e}_i}{\partial \xi^j}$ represent the "twisting" the coordinate system and is defined as:

$$\begin{gathered} \frac{\partial \boldsymbol{e}_k}{\partial \xi^j} = \Gamma_{kj}^i \boldsymbol{e}_i \\ \Gamma_{kj}^i = \frac{1}{2} g^{im}\left(\frac{\partial g_{jm}}{\partial \xi^k} + \frac{\partial g_{km}}{\partial \xi^j} - \frac{\partial g_{kj}}{\partial \xi^m}\right) = \frac{\partial \xi^i}{\partial x^p}\frac{\partial^2 x^p}{\partial \xi^k \xi^j} \end{gathered} \tag{2.20}$$

where Γ_{kj}^i is the Christoffel's symbol (coefficient of connection), are the components of the connection with respect to a system of local coordinates.

Consequently, Equation (2.20) can be reformulated as:

$$\frac{\partial \boldsymbol{V}}{\partial \xi^j} = \frac{\partial}{\partial \xi^j}\left(V^i \boldsymbol{e}_i\right) = \left(\frac{\partial V^i}{\partial \xi^j} + V^k \Gamma_{kj}^i\right)\boldsymbol{e}_i \tag{2.21}$$

Especially, ∇_j is defined as the covariant derivative, $\nabla_j V^i$ is expressed as:

$$\nabla_j V^i = \frac{\partial V^i}{\partial \xi^j} + V^k \Gamma_{kj}^i \tag{2.22}$$

Hence, based on equation (2.18), (2.20), and (2.22), the expression for the vector

gradient can be derived as:

$$\begin{aligned}\nabla \boldsymbol{V} &= \boldsymbol{e}^j \frac{\partial \boldsymbol{V}}{\partial \xi^j} \\ &= \left(\frac{\partial V^i}{\partial \xi^j} + V^k \Gamma_{kj}^i\right) \boldsymbol{e}^j \boldsymbol{e}_i = \left(\frac{\partial V^i}{\partial \xi^j} + V^k \Gamma_{kj}^i\right) g^{jm} \boldsymbol{e}_m \boldsymbol{e}_i \\ &= \nabla_j V^i g^{jm} \boldsymbol{e}_m \boldsymbol{e}_i\end{aligned} \tag{2.23}$$

Similarly, for a tensor $\boldsymbol{T}$ of rank 2, its differential can be expressed in the following form:

$$\begin{aligned}\frac{\partial \boldsymbol{T}}{\partial \xi^k} &= \frac{\partial}{\partial \xi^k}\left(T^{ij} \boldsymbol{e}_i \boldsymbol{e}_j\right) = \boldsymbol{e}_i \boldsymbol{e}_j \frac{\partial T^{ij}}{\partial \xi^k} + T^{ij} \boldsymbol{e}_j \frac{\partial \boldsymbol{e}_i}{\partial \xi^k} + T^{ij} \boldsymbol{e}_i \frac{\partial \boldsymbol{e}_j}{\partial \xi^k} \\ &= \boldsymbol{e}_i \boldsymbol{e}_j \frac{\partial T^{ij}}{\partial \xi^k} + T^{ij} \Gamma_{ki}^l \boldsymbol{e}_j \boldsymbol{e}_l + T^{ij} \Gamma_{kj}^l \boldsymbol{e}_i \boldsymbol{e}_l \\ &= \boldsymbol{e}_i \boldsymbol{e}_j \frac{\partial T^{ij}}{\partial \xi^k} + T^{lj} \Gamma_{kl}^i \boldsymbol{e}_j \boldsymbol{e}_i + T^{il} \Gamma_{kl}^j \boldsymbol{e}_i \boldsymbol{e}_j \\ &= \left(\frac{\partial T^{ij}}{\partial \xi^k} + T^{jl} \Gamma_{kl}^i + T^{il} \Gamma_{kl}^j\right) \boldsymbol{e}_i \boldsymbol{e}_j\end{aligned} \tag{2.24}$$

Therefore, $\nabla_k T^{ij}$ is expressed as:

$$\nabla_k T^{ij} = \frac{\partial T^{ij}}{\partial \xi^k} + T^{jl} \Gamma_{kl}^i + T^{il} \Gamma_{kl}^j \tag{2.25}$$

(2) Divergence of vector

Assume a vector $\boldsymbol{V}$, the divergence of $\boldsymbol{V}$ is

$$\nabla \cdot \boldsymbol{V} = \nabla \cdot (V^j \boldsymbol{e}_j) \tag{2.26}$$

Based on the Leibniz rule and equation (2.7), the following expression can be derived:

$$\begin{aligned}\nabla \cdot \boldsymbol{V} &= \nabla\left(V^j\right) \cdot \boldsymbol{e}_j + V^j \nabla \cdot \boldsymbol{e}_j \\ &= \frac{\partial V^j}{\partial \xi^i} \boldsymbol{e}^i \cdot \boldsymbol{e}_j + V^j \nabla \cdot \boldsymbol{e}_j \\ &= \frac{\partial V^j}{\partial \xi^i} \delta^i{}_j + V^j \nabla \cdot \boldsymbol{e}_j \\ &= \frac{\partial V^j}{\partial \xi^j} + V^j \nabla \cdot \boldsymbol{e}_j\end{aligned} \tag{2.27}$$

In equation (2.29), $\nabla \cdot \boldsymbol{e}_j$ can be derived as

$$\begin{aligned}\nabla \cdot \boldsymbol{e}_j &= \boldsymbol{e}^i \cdot \frac{\partial \boldsymbol{e}_j}{\partial \xi^i} = \boldsymbol{e}^i \cdot \Gamma_{kj}^k \boldsymbol{e}_k \\ &= \Gamma_{ji}^i = \frac{1}{\sqrt{g}} \frac{\partial \sqrt{g}}{\partial \xi^j}\end{aligned} \tag{2.28}$$

Therefore, equation (2.28) becomes

$$\nabla \cdot \boldsymbol{V} = \frac{\partial V^j}{\partial \xi^j} + \frac{V^j}{2g} \frac{\partial g}{\partial \xi^j} = \frac{1}{\sqrt{g}} \frac{\partial \sqrt{g} V^j}{\partial \xi^j} \tag{2.29}$$

According to equation (2.25), (2.25) and (2.25), the divergence of a tensor $\boldsymbol{T}$ of rank 2 is

$$\begin{aligned}\nabla \cdot \boldsymbol{T} &= \boldsymbol{e}^k \cdot \frac{\partial}{\partial \xi^k} (T^{ij} \boldsymbol{e}_i \boldsymbol{e}_j) \\ &= \nabla_k T^{ij} \boldsymbol{e}^k \cdot \boldsymbol{e}_i \boldsymbol{e}_j = \nabla_k T^{ij} \delta^k{}_i \boldsymbol{e}_j \\ &= \nabla_i T^{ij} \boldsymbol{e}_j\end{aligned} \tag{2.30}$$

2.3 Governing equations in the curvilinear coordinate system

2.3.1 Governing equation for flow model

The governing equation of this flow model[3)] is the incompressible Navier-Stokes equation.

[continuity equation]

$$\nabla \cdot \rho \boldsymbol{V} = 0 \tag{2.31}$$

[momentum equation]

$$\frac{\partial \rho \boldsymbol{V}}{\partial t} + \nabla \cdot [\rho \boldsymbol{V} \boldsymbol{V}] = -\nabla p + \nabla \cdot \boldsymbol{\tau} + \rho \boldsymbol{G} \tag{2.32}$$

where t: time, $\boldsymbol{V}$: velocity vector, ρ: the density of the fluid, p: pressure, $\boldsymbol{\tau}$: shear stress, $\boldsymbol{G}$: gravitational acceleration.

In this numerical model, the contravariant components of the vector are adopted as the solution variables for the equations. Consequently, the continuity equation (2.33) in the vector form can be expressed as follows:

[continuity equation]

$$\frac{1}{\sqrt{g}}\frac{\partial\sqrt{g}\rho V^i}{\partial\xi^i}=0 \tag{2.33}$$

In reference to equation (2.32), $\rho\boldsymbol{VV}$ is a tensor of rank 2, the divergence of $\rho\boldsymbol{VV}$, when reformulated within a curvilinear coordinate system, is expressed as follows:"

$$\begin{aligned}\nabla\cdot[\rho\boldsymbol{VV}]&=\nabla\cdot\left(\rho V^iV^j\boldsymbol{e}_i\boldsymbol{e}_j\right)\\&=\nabla_k\rho V^iV^j\boldsymbol{e}^k\cdot\boldsymbol{e}_i\boldsymbol{e}_j=\nabla_i\rho V^iV^j\boldsymbol{e}_j\end{aligned} \tag{2.34}$$

According to equation (2.19), the gradient of the pressure ∇p is expressed as:

$$\nabla p=\boldsymbol{e}^k\frac{\partial p}{\partial\xi^k}=\boldsymbol{e}_jg^{jk}\frac{\partial p}{\partial\xi^k} \tag{2.35}$$

The divergence of $\nabla\cdot\boldsymbol{\tau}$ is expressed by the divergence of the velocity gradient as:

$$\begin{aligned}\nabla\cdot\boldsymbol{\tau}&=\nabla\cdot\mu\left(\frac{\nabla\boldsymbol{V}+\nabla\boldsymbol{V}^T}{2}\right)\\&=\boldsymbol{e}^k\cdot\frac{\partial}{\partial\xi^k}\frac{\mu}{2}\left(\nabla_jV^ig^{jm}\boldsymbol{e}_m\boldsymbol{e}_i+\nabla_iV^jg^{im}\boldsymbol{e}_m\boldsymbol{e}_j\right)\end{aligned} \tag{2.36}$$

Obviously $\nabla\boldsymbol{V}+\nabla\boldsymbol{V}^T$ is a tensor, and to simplify the expression, let equation (2.37) be equivalent to the following:

$$\begin{aligned}\nabla\cdot\boldsymbol{\tau}&=2\nabla\cdot\mu\boldsymbol{S}^{ij}\\\boldsymbol{S}^{ij}&=\frac{1}{2}\left(\nabla_jV^ig^{jm}\boldsymbol{e}_m\boldsymbol{e}_i+\nabla_iV^jg^{im}\boldsymbol{e}_m\boldsymbol{e}_j\right)\end{aligned} \tag{2.37}$$

In reference to the equation (2.32), the equation (2.38) is reformulated as follows:

$$\begin{aligned}\nabla\cdot\mu\boldsymbol{S}^{ij}&=\nabla_i\mu S^{ij}\boldsymbol{e}_j\\&=\nabla_i\left(\frac{\mu}{2}\left(\nabla_\alpha V^ig^{j\alpha}+\nabla_\beta V^jg^{i\beta}\right)\right)\boldsymbol{e}_j\end{aligned} \tag{2.38}$$

Based on the equations presented above, momentum equation (2.34) in vector form can be reformulated as follows:

$$\frac{\partial\rho V^j\boldsymbol{e}_j}{\partial t}+\nabla_i\rho V^iV^j\boldsymbol{e}_j=-g^{jk}\frac{\partial p}{\partial\xi^k}\boldsymbol{e}_j+2\nabla_i\mu S^{ij}\boldsymbol{e}_j+\rho G^j\boldsymbol{e}_j \tag{2.39}$$

Consequently, the incompressible Navier-Stokes equations, subjected to the Reynolds averaging procedure within the curvilinear coordinate system, are reformulated as follows:

[continuity equation]

$$\frac{1}{\sqrt{g}}\frac{\partial\sqrt{g}\rho V^i}{\partial\xi^i}=0 \tag{2.40}$$

[momentum equation]

$$\frac{\partial \rho V^i}{\partial t} + \nabla_j\left[\rho V^i V^j\right] = \rho G^i - g^{ij}\nabla_j p + \nabla_j\left[-\rho\overline{v^i v^j}\right] + 2\nabla_j\,\mu\,S^{ij}$$
$$S^{ij} = \frac{1}{2}(g^{i\alpha}\nabla_\alpha V^j + g^{j\beta}\nabla_\beta V^i) \tag{2.41}$$

where t: time, ξ^i: spatial coordinates of the computational space, V^i: contravariant component of velocity vector, v^i: contravariant component of the turbulent velocity vector, p: pressure, ρ: the density of the fluid, g: determinate of metric tensor, μ: viscosity coefficient of the fluid, g^{ij}, g_{ij}: contravariant components and covariant components of metric tensor, S^{ij}: contravariant components of rate of strain tensor, G^i: contravariant components of the gravity.

In the computational space, the contravariant components of the velocity vector, denoted as V^i, and the orthogonal components in the physical space, represented by U^i, are transformed using the following transformation equation, commonly referred to as the Chain Rule, and defined as:

$$V^i = \frac{\partial \xi^i}{\partial x^k}U^k,\ U^i = \frac{\partial x^i}{\partial \xi^k}V^k \tag{2.42}$$

2.3.2 Nonlinear turbulence model

In the present study, a second order nonlinear $k-\varepsilon$ turbulence model proposed by Kimura and Hosoda[4] is utilized. Compared to standard $k-\varepsilon$ turbulence model, this nonlinear $k-\varepsilon$ turbulence model takes account of the anisotropy of turbulence, offering a more accurate representation of complex turbulent flows, such as the secondary currents of the second kind. The respective k equation and ε equation in the boundary-fitted coordinate system are expressed as:

[k *equation*]

$$\frac{\partial k}{\partial t} + \nabla_j\left[kV^j\right] = -g_{ij}\overline{v^i v^j}\nabla_j V^i - \varepsilon + \nabla_j\left\{\left(\frac{D_t}{\sigma_k} + \nu\right)g^{ij}\nabla_i k\right\} \tag{2.43}$$

[ε *equation*]

$$\frac{\partial \varepsilon}{\partial t} + \nabla_j\left[\varepsilon V^j\right] = -C_{\varepsilon 1}\frac{\varepsilon}{k}g_{ij}\overline{v^i v^j}\nabla_j V^i - C_{\varepsilon 2}\frac{\varepsilon^2}{k} + \nabla_j\left\{\left(\frac{D_t}{\sigma_k} + \nu\right)g^{ij}\nabla_i \varepsilon\right\} \tag{2.44}$$

Reynolds stress $\overline{v^i v^j}$

$$-\overline{v^i v^j} = D_t S^{ij} - \frac{2}{3} k \delta_s^i g^{sj} - \frac{k}{\varepsilon}(\alpha_1 Q_1 + \alpha_2 Q_2 + \alpha_3 Q_3) \tag{2.45}$$

$$D_t = C_\mu \frac{k^2}{\varepsilon} \tag{2.46}$$

where k : turbulence energy, ε : turbulence energy dissipation rate, D_t : eddy viscosity coefficient.

Generally, C_μ is a constant of 0.09 in the standard $k-\varepsilon$ model. While in the nonlinear $k-\varepsilon$ turbulence model C_μ is defined as:

$$C_\mu = \min(0.09, \frac{0.3}{(1+0.09M^2)}) \tag{2.47}$$

$$Q_1 = S^{i\alpha} g_{\alpha l} \Omega^{lj} + S^{j\beta} g_{\beta l} \Omega^{li} \tag{2.48a}$$

$$Q_2 = S^{i\alpha} g_{\alpha l} S^{lj} - \frac{1}{3} S^{k\alpha} g_{\alpha m} S^{m\beta} g_{\beta k} \delta_l^i g^{lj} \tag{2.48b}$$

$$Q_3 = \Omega^{i\alpha} g_{\alpha l} \Omega^{lj} - \frac{1}{3} \Omega^{k\alpha} g_{\alpha m} \Omega^{m\beta} g_{\beta k} \delta_l^i g^{lj} \tag{2.48c}$$

$$S^{ij} = g^{j\alpha} \nabla_\alpha V^i + g^{i\alpha} \nabla_\alpha V^j \tag{2.48d}$$

$$\Omega^{ij} = g^{j\alpha} \nabla_\alpha V^i - g^{i\alpha} \nabla_\alpha V^j \tag{2.48e}$$

$$\alpha_1 = -0.1325 f_M, \quad \alpha_2 = 0.0675 f_M, \quad \alpha_3 = -0.0675 f_M \tag{2.48f}$$

$$f_M = (1+0.02M^2)^{-1}, M = max\,(S, \Omega) \tag{2.48g}$$

$$S = \frac{k}{\varepsilon} \sqrt{\frac{1}{2} S^{i\alpha} g_{\alpha j} S^{j\beta} g_{\beta i}} \tag{2.48h}$$

$$\Omega = \frac{k}{\varepsilon} \sqrt{\frac{1}{2} \Omega^{i\alpha} g_{\alpha j} \Omega^{j\beta} g_{\beta i}} \tag{2.48i}$$

where k : turbulence energy, ε : turbulence energy dissipation rate, D_t : eddy viscosity coefficient, S: strain parameter, Ω: rotation parameter, and model constants ($\sigma_k = 1.0,\ \sigma_\varepsilon = 1.3,\ C_{\varepsilon 1} = 1.44,\ C_{\varepsilon 2} = 1.92$)

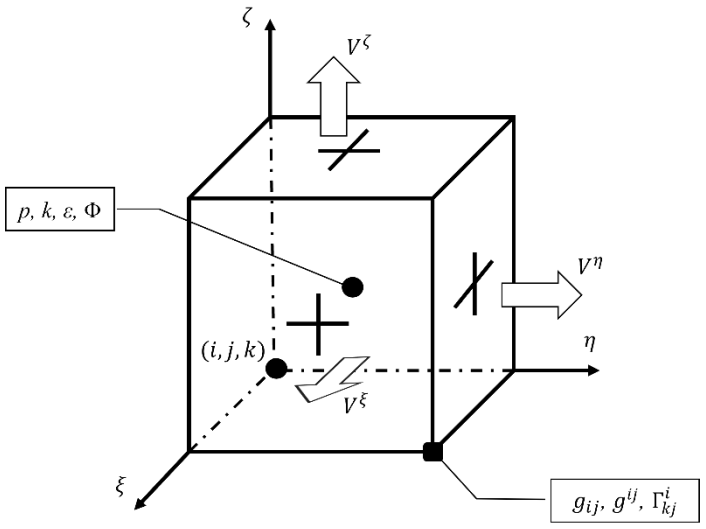

Figure 2.1 Arrangement of hydraulic quantities in a staggered grid

2.4 Numerical methods

In the present study, the governing equations are discretized using the finite volume method (FVM) on staggered grids within a curvilinear coordinate system. **Figure 2.1** shows the definition point of each physical parameter. The velocities of the flow are assigned to the central points of the grid's surface, while the pressure p, density function Φ, turbulence energy *k*, and turbulence energy dissipation ε rate are defined at the center point of the grid, which is shown in **Figure 2.1**.

2.4.1 Discretization of the convection and diffusion terms

To discretize the advection terms in the equations of motion, QUICK scheme is adopted, while central difference method is utilized for the diffusion term. For the convection terms in the *k* and ε equations, the hybrid method is employed. The time integration is explicit, employing the 2nd order Adams-Bashforth method.

2.4.2 HSMAC method for pressure iteration

The MAC method and the SMAC method are extensively employed for computing the pressure terms in incompressible flow simulation. However, since both approaches utilize implicit methods, they necessitate the solution of large-scale linear equation systems, imposing a significant computational cost. To reduce the computational

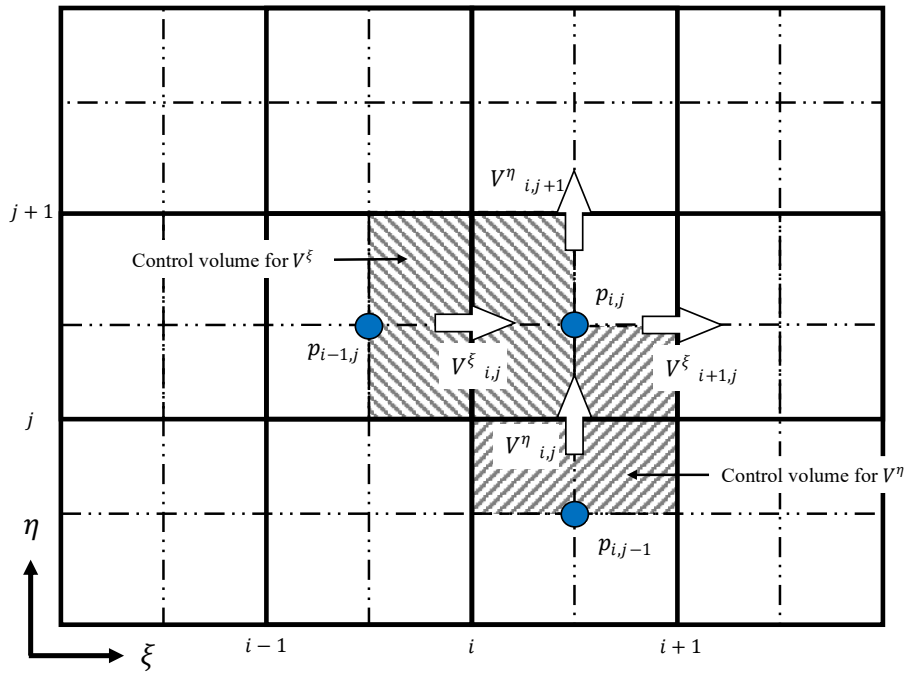

Figure 2.2 Control volumes in a staggered grid for arrangement for V^{ξ}, V^{η} and p

load, the HSMAC (Highly Simplified MAC) method[4] approximates the Poisson equation using an explicit formulation.

In the present numerical model, the HSMAC method has been extended to a general curvilinear coordinate system. Equations (2.51) and (2.52) respectively depict the expressions for the corrected pressure p^c in the two coordinate systems.

$$\Delta p^c = -\frac{\gamma \nabla \cdot \rho \boldsymbol{V^{pr}}}{2\Delta t(\frac{1}{\Delta x^2}+\frac{1}{\Delta y^2}+\frac{1}{\Delta z^2})} \tag{2.49}$$

$$\Delta p^c = -\frac{\gamma \nabla \cdot \rho \boldsymbol{V^{pr}}}{2\Delta t(\frac{g^{\xi\xi}}{\Delta \xi^2}+\frac{g^{\eta\eta}}{\Delta \eta^2}+\frac{g^{\zeta\zeta}}{\Delta \zeta^2})} \tag{2.50}$$

where Δp^c: the corrected pressure, Δt: time integral, Δx, $\Delta \xi$: the spatial integral in physical space and computational space respectively, $\boldsymbol{V^{pr}}$: the predicted velocity, γ: relaxation coefficient (= 1.7).

To minimize the effects of abnormal pressure gradients, treatment of pressure term[5] is modified the as follows:

$$g^{ij}\nabla_j p = \frac{\partial p}{\partial x_j}\frac{\partial \xi^i}{\partial x_j} \tag{2.51}$$

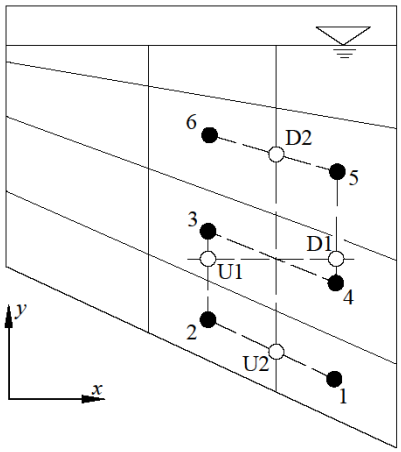

Figure 2.3 Schematic of the pressure correction method[5)]

In **Figure 2.3**, water is stored within an inclined water tank, under hydrostatic conditions. However, when the equations of motion are discretized in the curvilinear coordinate system, abnormal flows are induced by an unreasonable pressure gradient due to irregular grids. In practical scenarios, the pressure gradient $\partial p/\partial \xi_1$ at the grid surface (the surface between point 3 and 4) should be zero, but $\partial p/\partial \xi_1 \approx (p3 - p4)/\Delta\xi \neq 0$ as shown in **Figure 2.3.**

Equation (2.51) means the pressure gradient is initially discretized within the Cartesian coordinate system through the utilization of the interpolated pressure $p_{U1}$and p_{D1}, which is then subsequently transferred to the curvilinear coordinate system.

2.4.3 Free surface capturing method: density function method

The VOF (Volume of Fluid) method is a widely employed interface capturing technique, known for its robust performance and minimal computational resource requirements. However, implementing the VOF method in a generalized curvilinear coordinate system are quite intricate. Hence, in this model, the density function method, which is relatively straightforward to implement, is utilized to capture the interface between air and water.

Similar to the VOF method, the density function method defines a density function Φ that represents the volume ratio of the liquid phase in the cell (Φ=1: liquid phase, $0<\Phi<1$: gas-liquid interface, Φ=0: gas phase), and captures the gas-liquid interface by solving the convective equation (2.52) of the density function.

$$\frac{\partial \Phi}{\partial t} + \frac{1}{\sqrt{g}} \frac{\partial \sqrt{g} \Phi V^i}{\partial \xi^i} = 0 \tag{2.52}$$

The convective term in equation (2.52) is addressed using the TVD-MUSCL scheme, while the second-order Adams-Bashforth method is employed for temporal integration. Furthermore, to mitigate the blurry phenomenon of the gas-liquid interface caused by numerical diffusion, a volume correction method[7] is implemented. It should be noted that the volume correction method is specifically applied to free surface flow since numerical diffusion occurs within a gas-liquid interface in the surface flow with the high velocity.

2.4.4 Boundary conditions

In proximity to the wall region, the friction velocity u_*, turbulence kinematic energy k, and turbulence energy dissipation rate ε are assessed utilizing a wall function (smooth wall) based on the log-law, shown in equation (2.53) and (2.54).

$$\begin{gathered} \frac{V_p}{u_*} = \frac{1}{\kappa} ln \frac{u_* z_p}{\nu} + A_s \\ V_p = \sqrt{g_{\xi\xi} V^{\xi 2} + g_{\eta\eta} V^{\eta 2} + 2 g_{\xi\eta} V^{\xi} V^{\eta}} \end{gathered} \tag{2.53}$$

$$\begin{gathered} k = \frac{{u_*}^2}{\sqrt{C_\mu}} \\ \varepsilon = \frac{{u_*}^3}{\kappa z_p} \end{gathered} \tag{2.54}$$

where V_p is the velocity magnitude at center of the first layer, z_p is the distance between the wall and the center of the first layer of mesh, ν is the dynamic viscosity coefficient, κ is Kármán constant (= 0.41), C_μ is a constant (= 0.09) and A_s is a constant (= 5.5).

The Dirichlet boundary condition is applied to the velocity at the inlet boundary, while Neumann boundary condition is applied to the Φ, pressure p and velocity at the outlet boundary. At the gas-liquid interface, given that both phases are solved using the same governing equations, no additional considerations are required near the interface.

2.4.5 Procedure of the numerical model

Figure 2.4 illustrates the flow chart of how this numerical model operating.

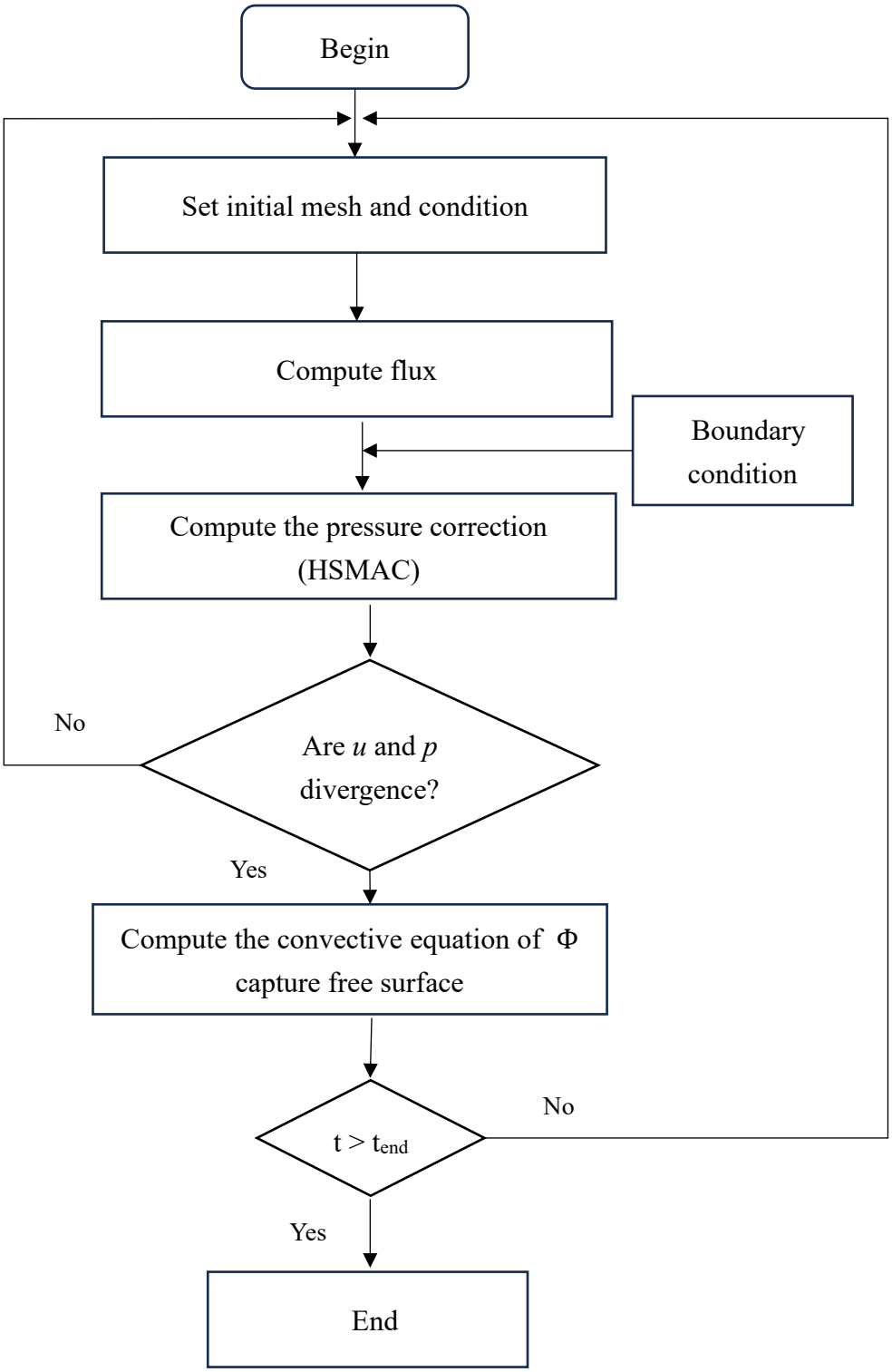

Figure 2.4 Flow chart of the numerical model

Reference

1) Ushijima, S. and Nezu, I. : Computational method for free-surface flows on collocated grid with moving curvilinear coordinates, *Japanese Journal of JSCE*, Vol. 2002, No. 698, pp. 11-19, 2002. (in Japanese)
2) Hosoda, T., Nagata, N. and Muramoto, Y. : Numerical analysis of unsteady open channel flows by means of moving boundary fitted coordinate system, *Japanese Journal of JSCE*, Vol. 1996, No. 533, pp. 267-272, 1996. (in Japanese)
3) Onda, S., Hosoda, T., Kimura, I. and Jaćimović, N. : Development and application of numerical method in open channel flow in boundary fitted coordinate system with density function method, *Journal of Japan Society of Civil Engineers*, *Ser.B1 (Hydraulic Engineering)*., Vol. 72, No. 4, pp. 505-510, 2016. (in Japanese)
4) Hirt, C. W., Nichols B. D. and Romero, N. C. : SOLA-A Numerical solution algorithm for transient fluid flows, *Los Alamos Scientific Report*, LA-5852, 1975
5) Jaćimović, N. : Numerical modeling of multiphase flows in porous media and its application in hydraulic engineering, *doctor thesis*, *Kyoto University*, 2007.
6) Kimura, I. and Hosoda, T. : A non-linear *k-ε* model with realizability for prediction of flows around bluff bodies, *International Journal for Numerical Methods in Fluids*, Vol. 42, No. 8, pp. 813-837, 2003.
7) Asai, K. and Tsubogo, K. : Study on volume correction method for free surface flow analysis using density function method, *Journal of Japan Society of Civil Engineers, Ser. B*, Vol. 62, No. 1, pp. 122-127, 2006. (in Japanese)

Chapter 3

Model applications to the open channel flows with side weir

3.1 Preliminaries

In this chapter, the numerical model is applied to simulate the overflows around the side weir in both straight and curved open channels. Side weirs, or rather lateral overflow weirs, are river hydraulic structures aimed to relieve flood risks by leading flood flows that exceed the capacity of river channels to a reservoir. To examine the characteristics of lateral overflows, side weirs set on the straight channel have been widely studied and attracted many meaningful research efforts in the past decades. De Marchi[1)] was probably the first researcher to study the weir discharge coefficient. After that, more researchers came up with different equations to estimate the discharge coefficient[2), 3), 4), 5), 6)]. The flow characteristics such as velocity distribution and water surface profile over a side weir were studied experimentally by Bagheri & Heidarpour[7)]. However, because of the topography and the limitation of urban regulations, the side weirs basically need to be constructed in the curved part of the river channel. Moreover, due to the influence of centrifugal force, secondary flow, and other factors, the hydraulic characteristics of river flows may differ from those in straight channels, so that the previous characteristics for the straight channel may no longer be applicable. More research on side weir flows in curved channels must be conducted experimentally and numerically.

Faras et al.[8)], Asai et al.[9)] and Kawamoto et al.[10), 11)] have studied the various characteristics of the side weir flows in the curved channel, such as water surface profile, velocity distribution, overflow rate, etc. through several different experiments. Akiyama et al.[11)] developed a 2D model governed by 2D shallow water equations to predict the side weir flows in a meandering channel. Though the prediction of discharge and inundation flow were satisfying and relatively accurate, the overall calculated water depth and

velocities were slightly larger than the experimental results. It was also observed that overflows around the side weir were not accurately simulated. The reason prediction errors were significant may be that the three-dimensionality of the flows near the side weir brought by impact between water and wall is strong, and it is quite difficult for a two-dimensional numerical model to simulate such sophisticated flows. In addition, the complex flow patterns, such as secondary flows, are also difficult to be accurately simulated by a 2D model. For 3D flow models, they have been wildly applied in various open channel flows. For instance, Jia et al.[13] reproduced the secondary flows using the standard $k-\varepsilon$ model and non-linear $k-\varepsilon$ model, respectively. They proved the non-linear $k-\varepsilon$ model can reproduce the secondary currents near the water surface of the outer bank in addition to the general helical flows brought in the channel bend. Kimura et al.[14] applied the 3D RANS model with 2nd and 3rd order non-linear $k-\varepsilon$ models to validate the reproductivity of secondary flows near the outer bank cell using rigid grids. However, while this model employs moving grids to depict the water surface variation, it falls short in simulating scenarios with significant water surface fluctuations, such as those encountered in overflow conditions. For the other 3D simulation of side weir flow, Bagherifar et al.[15] predicted the discharge rate, water surface profiles, specific energy, and surface velocities in a straight channel with a circular cross-section using FLOW-3D software. Though their model can predict characteristics of side weir flows with reasonable accuracy, their rectangular grids cannot fit the circular boundary completely, making them use more grids to fit the boundary shape as closely as possible.

The purpose of this chapter is to validate the model's reliability by comparing it with experimental data[10),11)], and then investigate the three-dimensional flow structure near the side weir in both straight channel and curved channel by numerical results.

3.2 Model applications

3.2.1 application to side weir flow in straight channel

(1) Experimental and computational conditions

In this study, the experiments conducted by Kawamoto et al.[10] was simulated, including Froude number ($Fr = 0.7$) in cross section of the upstream, relative weir width

(L/B), relative weir height (w_h) and relative water depth (h). The applicability of the model was verified by comparing the results of the water surface profile and velocity distribution of this case with the experimental result. Schematic view of experiment set-up and schematic view of side-weir are shown in **Figure 3.1** and **Figure 3.2**. h_1, h_2, h_3 are the water depth at center of each section respectively, and Section 1 is set as the origin $x_0/L = 0$. The experimental condition is shown in **Table 3.1**. Where Q_{IN} is inflow rate, Q_{OUT} is outflow rate, Q_{MEA} is the overflow rate, B (= 0.2 (m)) is the wilth of main channel, w is the height of side-weir and L is length of side weir. For boundary conditions, a constant flow rate Q_{IN} was given at the entrance of upstream, and the gradient of the physical quantities were set to zero at end of both the side weir channel and the main channel. Calculation time of this case is up to 200 (s), with a time step of 0.0005 (s). The computaional mesh in the horizontal plant is depicted in **Figure 3.3**, where the red mesh denotes the channel, and the yellow mesh indicates the location of the side weir. The upstream end (Section 1) of the side weir is established at $\mathbf{x} = 0$ (m). The rectangular computational mesh in streamwise ξ, transverse η, and vertical ζ directions consist of 120, 35, and 20 elements, and the mesh sizes in each direction are set to 2 (cm), 1 (cm), and 0.5 (cm), respectively.

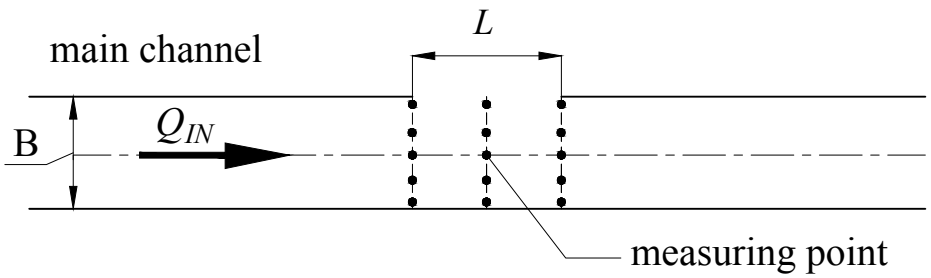

Figure 3.1 Schematic view of experiment set-up[10)]

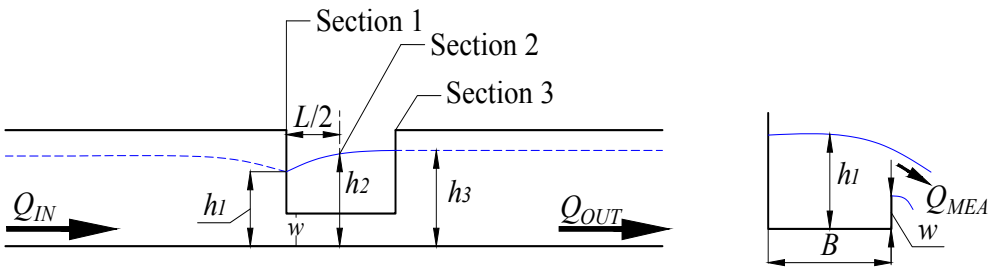

Figure 3.2 Schematic view of side-weir[10)]

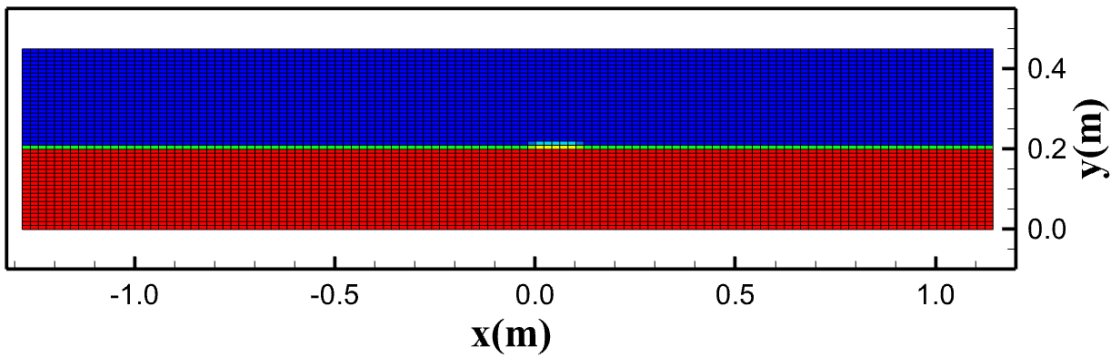

Figure 3.3 Computational mesh in the horizontal plant

Table 3.1 Experimental flow conditions[10)]

Case	Length of side-weir L (m)	Hight of side-weir w (cm)	Q_{IN} (m^3/s)
1	0.2	2.5	0.0042
2	0.1	2.5	0.0042
3	0.1	0	0.0042

(2) Comparison of water surface profile and velocity distribution in the streamwise direction for Case 1

Figure 3.4 shows the comparison between the calculated and measured water surface profiles of Case 1 at the center section along main channel. $x_0/L = 0$ represents the position of Section 1 and $x_0/L = 1$ represents position of Section 3. As shown in **Figure 3.4**, at the upstream end of the side weir, the water surface exhibits a continuous declining trend, until the central part of the side weir. Subsequently, there is a sudden rise in the water level, which reaches its peak at the downstream end of the weir before slightly decreasing to a stable condition. Compared to the experiment, a slightly higher calculated water surface profile around the side weir area was confirmed in this case, which a relatively rough gird size, 0.02 (m) compared to the channel width of 0.2 (m), might result in this situation. Thus, a finer grid will be tested in future analysis.

Figure 3.5 illustrates the non-dimensional velocity distribution at the center section along the main channel. The trend in flow velocity is correlated with the changes in the water surface profile shown in **Figure 3.4**. At the upper end of the side weir, the

flow velocity increases due to the descending water surface, in accordance with the flow continuity. Within the side weir region, the outflow results in a reduced flow rate of the main channel, leading to a decrease in flow velocity. This phenomenon is likely a contributing factor to the rise in the water surface observed downstream of the side weir.

As for the overflow rate Q_{MEA}, it was about 30% of total flow rate Q_{IN} in the experiment, while 28.7% was obtained in the numerical simulation. Overall, the results of the numerical simulation are in good agreement with experimental observations.

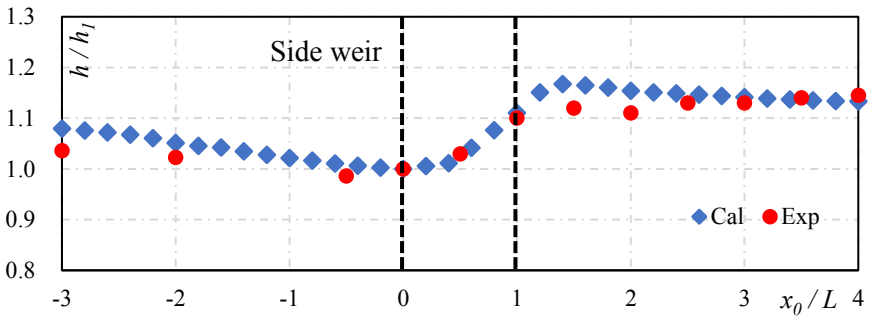

Figure 3.4 Comparison between the calculated and experimental water surface profiles

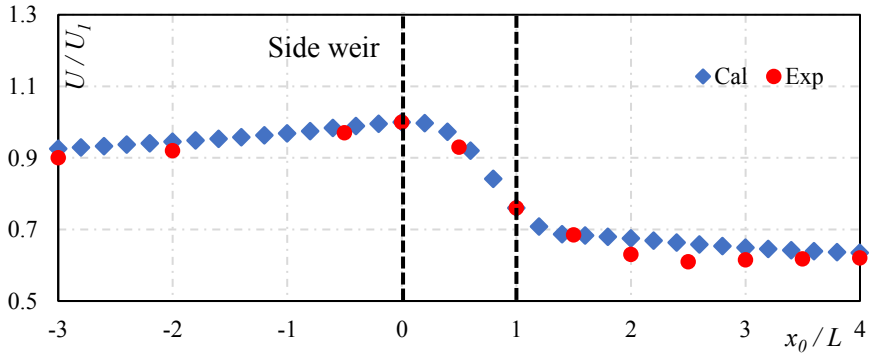

Figure 3.5 Comparison between the calculated and experimental velocity distribution

(3) Vector distributions around side weir

Figure 3.6 and Figure 3.7 illustrates the vector distribution for Case 1 in different sections. In Case 1, side weir is set between the section of $\mathbf{x} = 0$ (m) to $\mathbf{x} = 0.2$ (m). **Figure 3.6** depicted the distribution of flow velocity vectors in the streamwise direction, representing the velocity vectors at cross-sections located 1 cm and 5 cm from the side weir, respectively. The two figures clearly reveal the formation of a clockwise spiral flow at the bottom of the latter half of the side weir, specifically in the region from $\mathbf{x} = 0.1$ (m) to $\mathbf{x} = 0.2$ (m), influenced by the side weir flow. Additionally, **Figure 3.7** (a), **3.7** (b), and **3.7** (c) depict the velocity vector distributions at Section 1, 2, and 3, respectively. **Figure 3.7** (c) demonstrates that under the effect of the side weir flow, a secondary flow is generated at section 3, a phenomenon typically observed in curved channel flows.

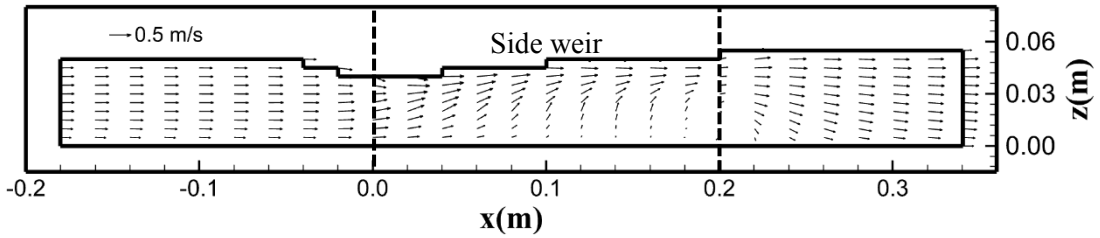

(a) Case 1, 1 (cm) from the side weir

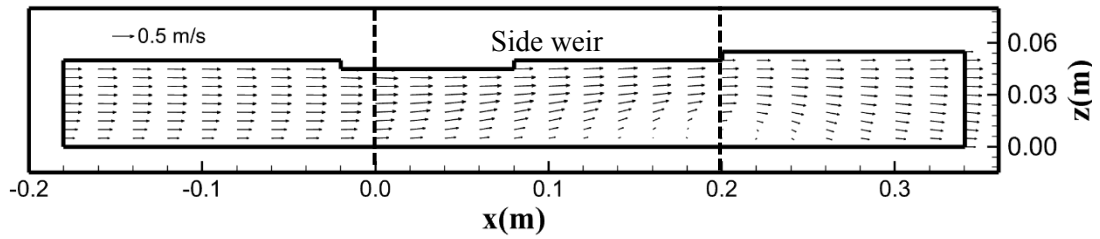

(b) Case 1, 5 (cm) from the side weir

Figure 3.6 Streamwise vector distribution for Case 1

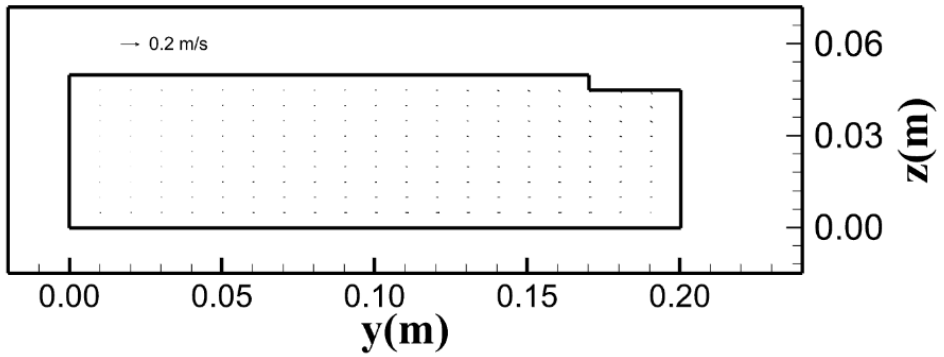

(a) Case 1, Section 1

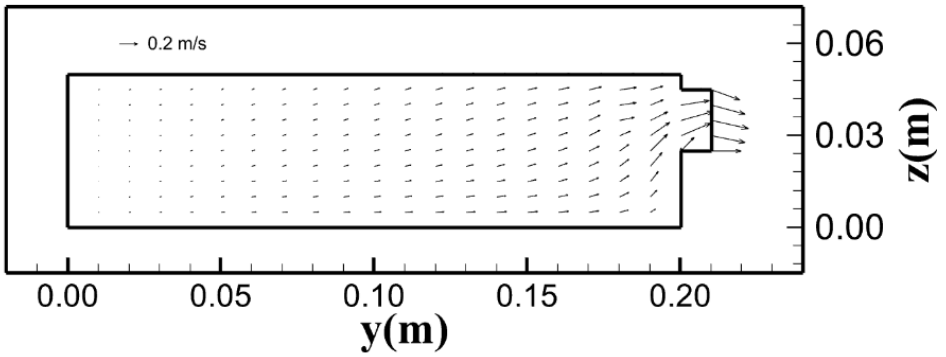

(b) Case 1, Section 2

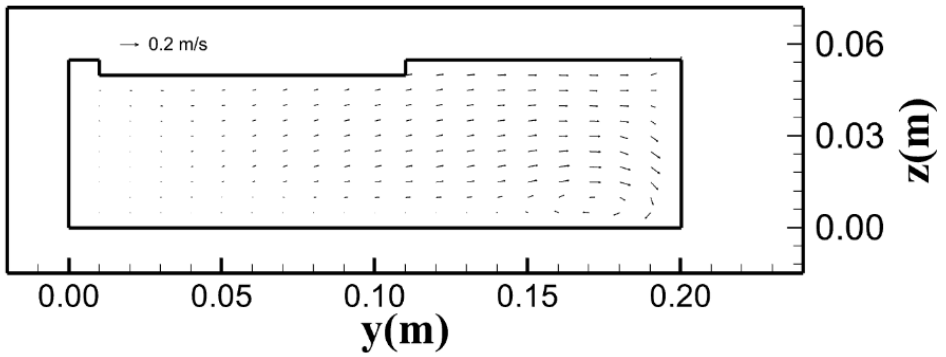

(c) Case 1, Section 3

Figure 3.7 Transverse vector distribution for Case 1

Figure 3.8 to **Figure 3.11** illustrates the vector distribution for Case 2 and Cse 3 respectivly, the positions of each figures are the same as those in **Figure 3.6** and **Figure 3.6.** In Case 2, the length of side weir is half of Case 1. **Figure 3.8** illustrates that even with the side weir's length halved, a spiral flow exists at the bottom of the latter half of the side weir, with the spiral becoming more pronounced closer to the side weir. The velocity distributions displayed in **Figures 3.9** (a), **3.9** (b), and **3.9** (c) are similar to those in **Figure 3.7**, and a secondary flow is observed at Section 3 in all cases.

Figure 3.10 reveals that due to the zero height of the side weir, a substantial volume of water flow out through the side weir, resulting in more pronounced changes in flow velocity. Correspondingly, the water surface variations near the side weir are more intense compared to Cases 1 and 2. Nevertheless, downstream of the side weir, near Section 3, a spiral flow similar to that observed in Cases 1 and 2 still observed. The velocity distributions for Case 3 displayed in Sections 1, 2, and 3 show little difference from Cases 1 and 2.

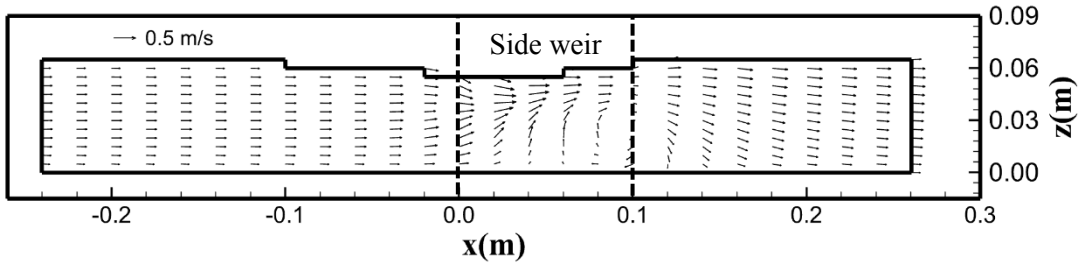

(a) Case 2, 1 (cm) from the side weir

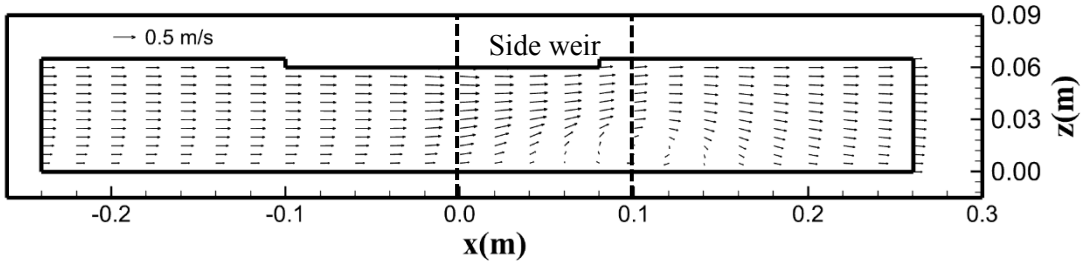

(b) Case 2, 5 (cm) from the side weir

Figure 3.8 Streamwise vector distribution for Case 2

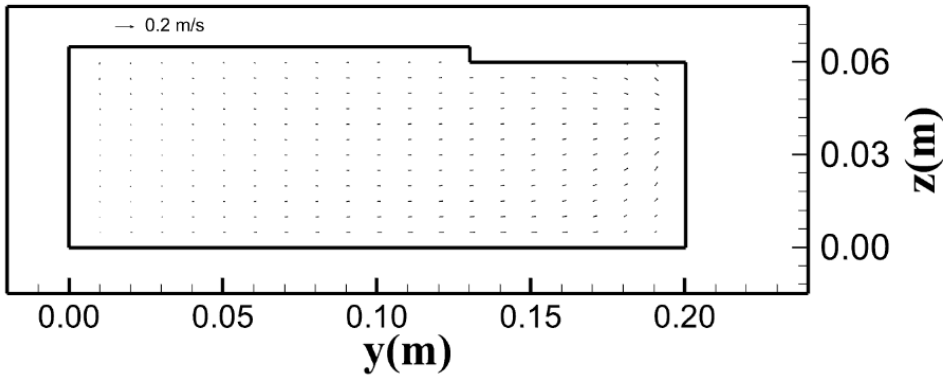

(a) Case 2, Section 1

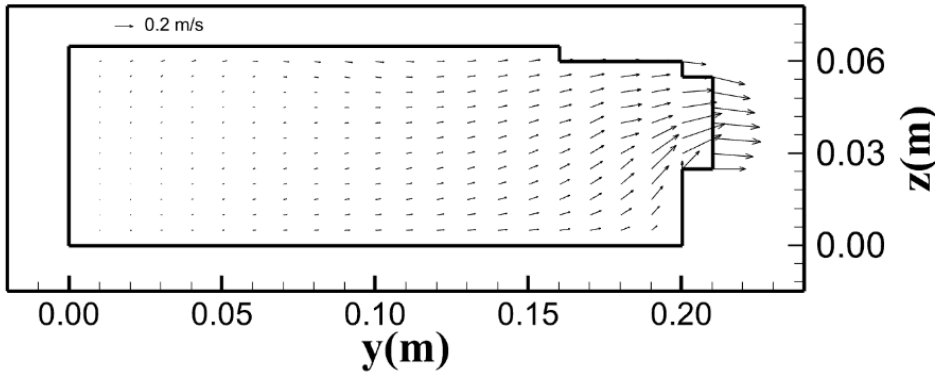

(b) Case 2, Section 2

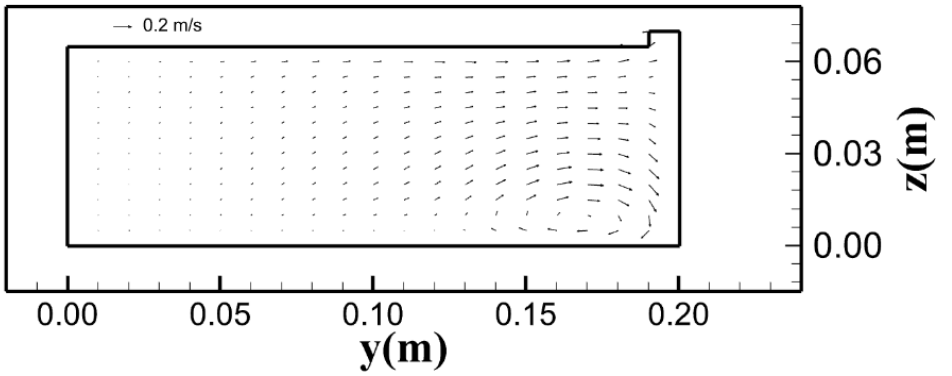

(c) Case 2, Section 3

Figure 3.9 Transverse vector distribution for Case 2

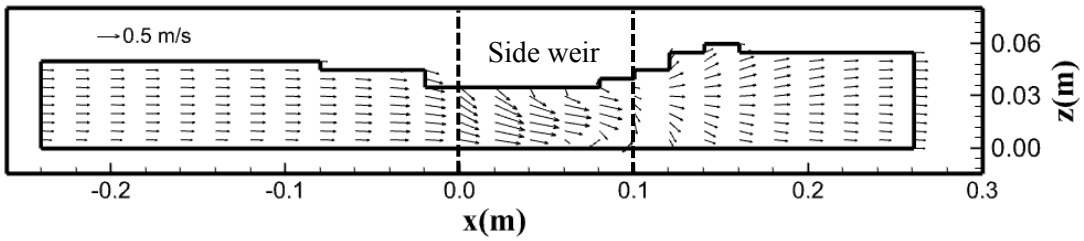

(a) Case 3, 1 (cm) from the side weir

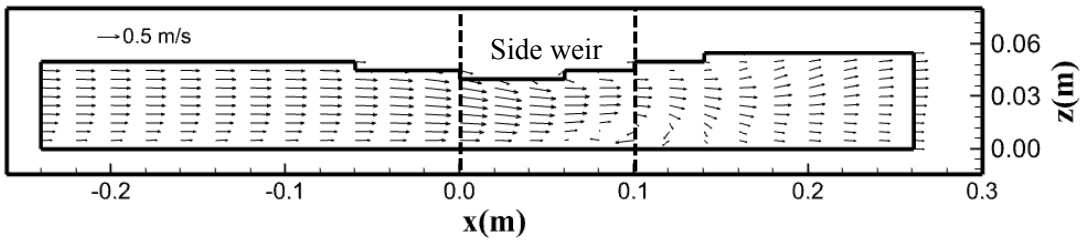

(b) Case 3, 5 (cm) from the side weir

Figure 3.10 Streamwise vector distribution for Case 3

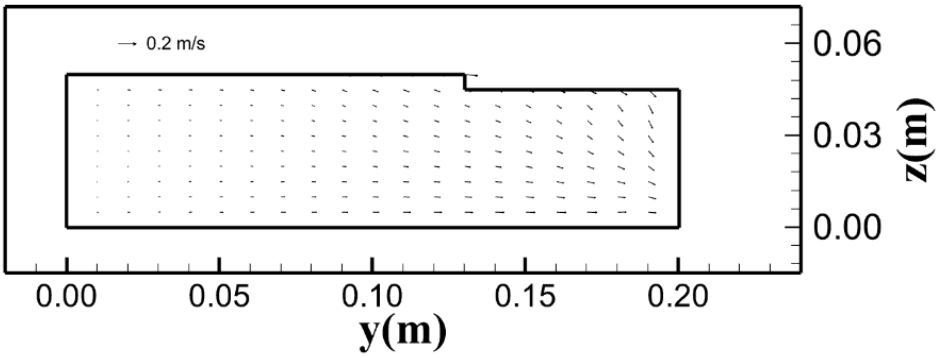

(a) Case 3, Section 1

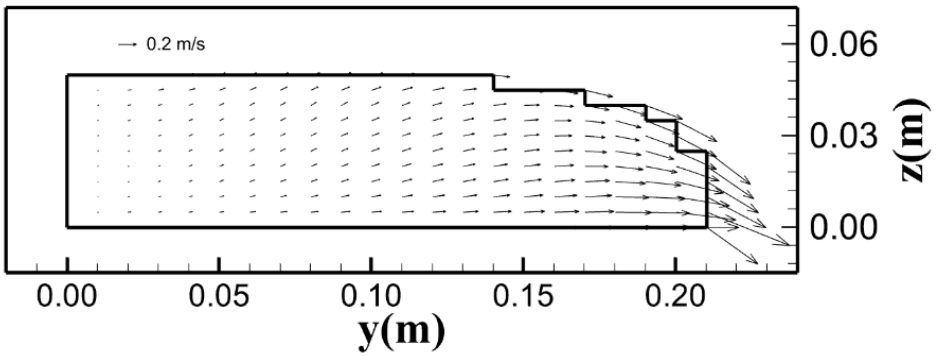

(b) Case 3, Section 2

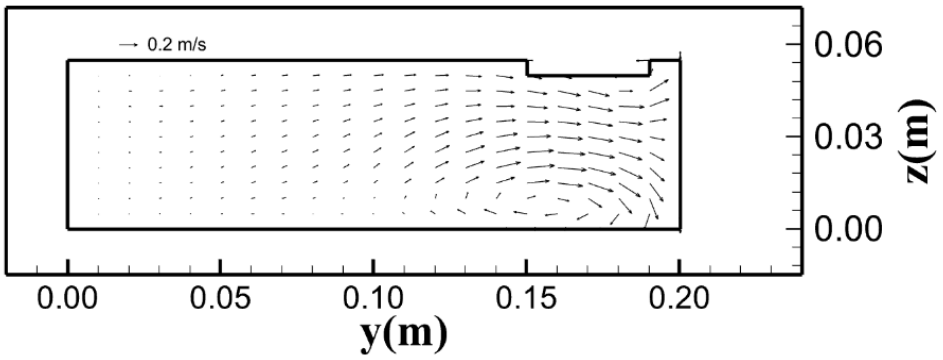

(c) Case 3, Section 3

Figure 3.11 Transverse vector distribution for Case 3

(4) Pressure distributions around side weir

Figure 3.12 indicates that near the end of the side weir in all three cases, the pressure at the bottom is higher than in the region just upstream of the side weir's end. This elevated pressure possibly comes from the rise in water surface near Section 3. The unit of pressure in this figure is pascal. Under the influence of this pressure gradient, the spiral flows in **Figures 3.6**, **3.8**, and **3.10** were observed. Furthermore, **Figure 3.12(c)** suggests that due to the zero height of the side weir in Case 3, which results in a complete overflow, the pressure within the side weir region is markedly low, nearly approaching zero. This leads to a more significant pressure gradient near Section 3, thereby intensifying the spiral flow in Case 3 compared to Cases 1 and 2.

(5) Comparison of the ratio of overflow to inflow rate

A comparison of the measured and predicted ratio of overflow to inflow rate of the side weir is shown in **Table 3.2**. The data presented in the table indicates a good agreement between the calculated and experimentally observed overflow ratio. Comparative analysis reveals that wider overflow weirs correspond to increased overflow discharge, and lower weir heights result in greater overflow volumes.

Table 3.2 Ratio of overflow to inflow rate in straight channel

Case	Height of side weir w (cm)	Length of side-weir L (m)	Q_{MEA}/Q_{IN} Exp.	Q_{MEA}/Q_{IN} Cal.
1	2.5	0.2	0.386	0.351
2	2.5	0.1	0.179	0.167
3	0	0.1	0.423	0.401

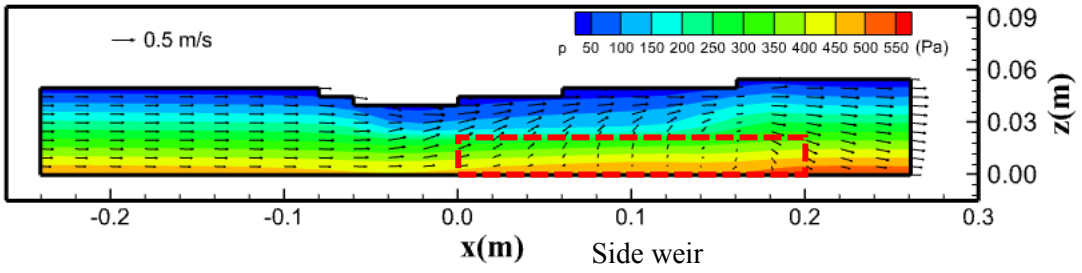

(a) Case 1, 1 (cm) from the side weir

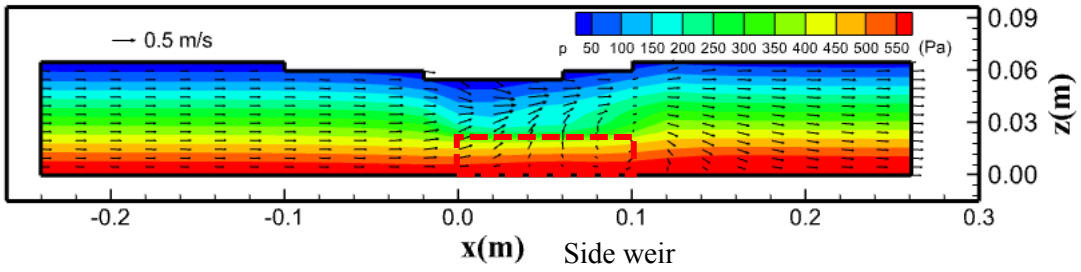

(b) Case 2, 1 (cm) from the side weir

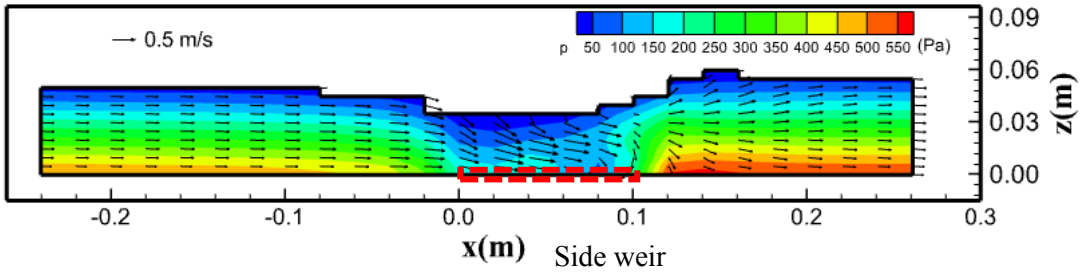

(c) Case 3, 1 (cm) from the side weir

Figure 3.12 Streamwise vector distribution and pressure contour for Case 1, 2 and 3

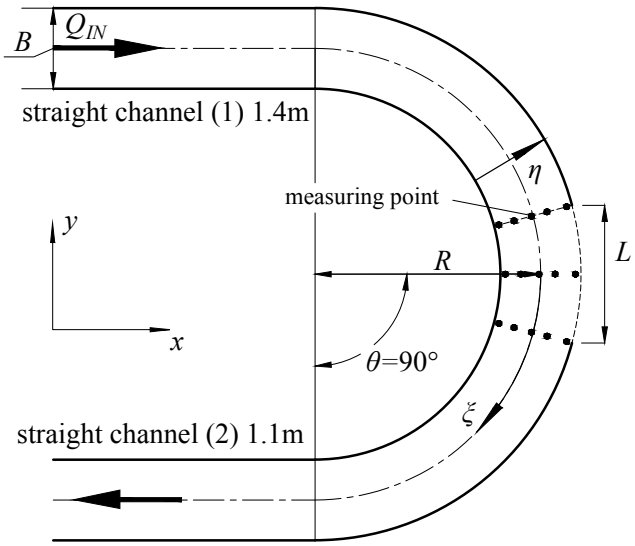

Figure 3.13 Schematic view of experimental set-up[11)]

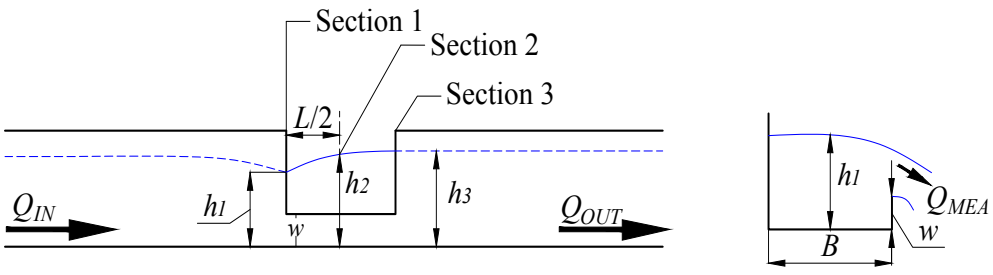

Figure 3.14 Schematic view of side weir[11)]

3.2.2 Application to side weir flow in curved channel

(1) Experimental and computational conditions

The flow parameters and hydraulic conditions were the same as in experiments[11]. **Figure 3.13** and **Figure 3.14** show the schematic views of the experimental set-up and the side weir in detail. The experimental conditions are shown in **Table 3.3**.

B is the width of the channel, w is the height of the weir, L is the length of the weir, the straight channel upstream is 1.4 (m), the straight channel downstream is 1.1 (m), the gradient of the channel is 0, and radius R is 0.7 (m) in this experiment. h_1, h_2, h_3 are the water depths at center of each section respectively, and Section1, Section 2 and Section 3 are set as ξ/L = -0.5, 0 and 0.5 respectively. The entrance and end of the channel bend are set as ξ/L = -5.5 and ξ/L = 5.5 respectively. Here, ξ is the distance from the center position of the weir as shown in **Figure 3.13.**

Q_{IN} is the inflow rate, Q_{OUT} is the outflow rate, and Q_{MEA} is the overflow rate form the side weir. For boundary conditions, a constant flow rate Q_{IN} was given at the inlet upstream, and the gradient of the physical quantities was set to zero at the end of both the side weir channel and the main channel. Calculation time is up to 200 (s), when the flow is steady, in each case, and time step Δt is 0.0005 (s).

The computational meshes consist of 110, 60, and 40 in streamwise, transversal, and vertical directions, respectively, with mesh sizes in each direction of 3 (cm), 0.5 (cm), and 0.5 (cm). In the curved part of the channel, the semicircular channel was equally spaced at 3° intervals, shown in **Figure 3.15**. The red mesh is the flow zone, and green mesh shows the location of the side weir.

Table 3.3 Experimental flow conditions[11]

Case	Length of side weir L (m)	Height of side weir w (cm)	Q_{IN} (m^3/s)
1	0.2	3.5	0.0042
2	0.2	3.5	0.0030
3	0.2	3.5	0.0020
4	0.2	0	0.0042
5	0.2	0	0.0030
6	0.2	0	0.0020

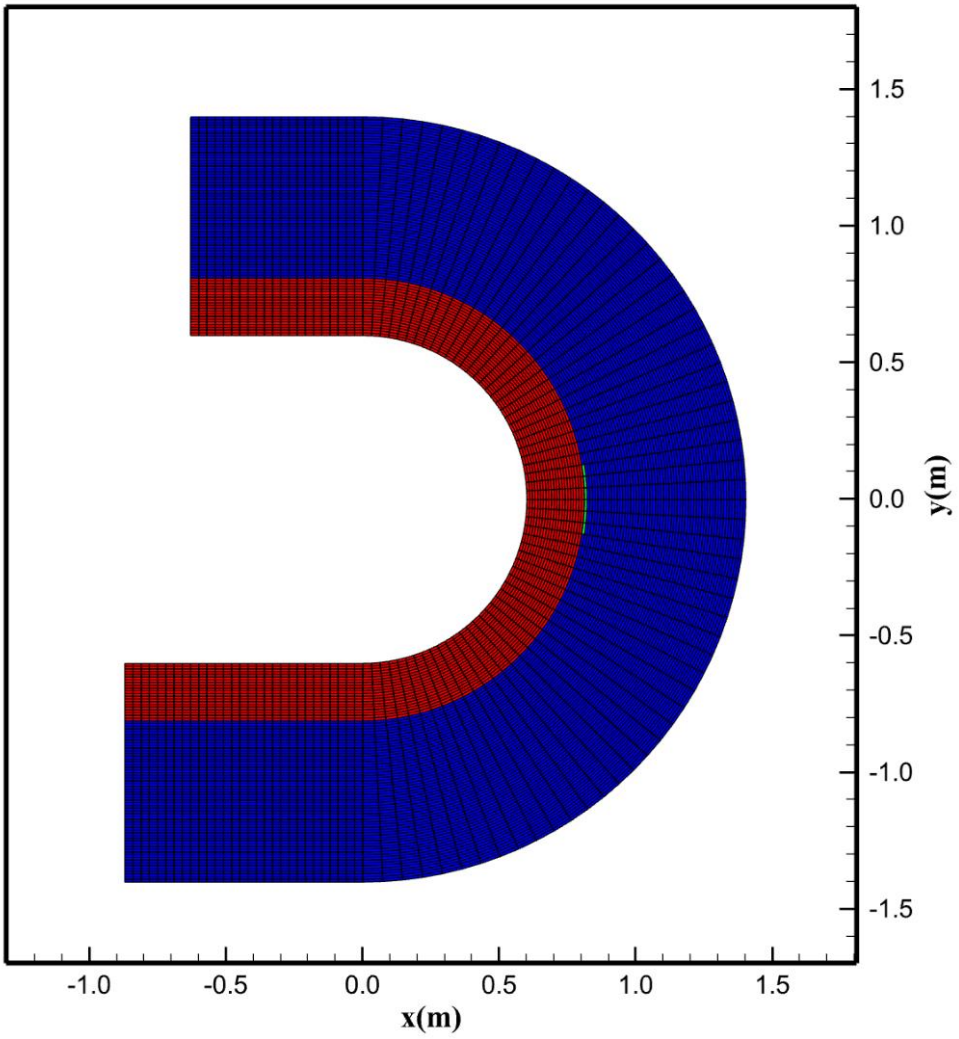

Figure 3.15 Comeputaional mesh in the horizontal plant

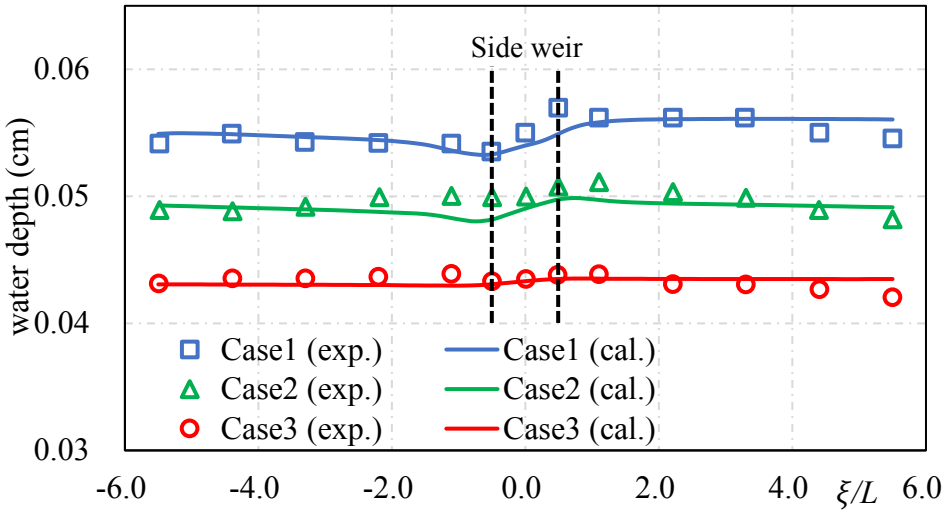

(a) Case 1, 2 and 3 (w/B=0.175)

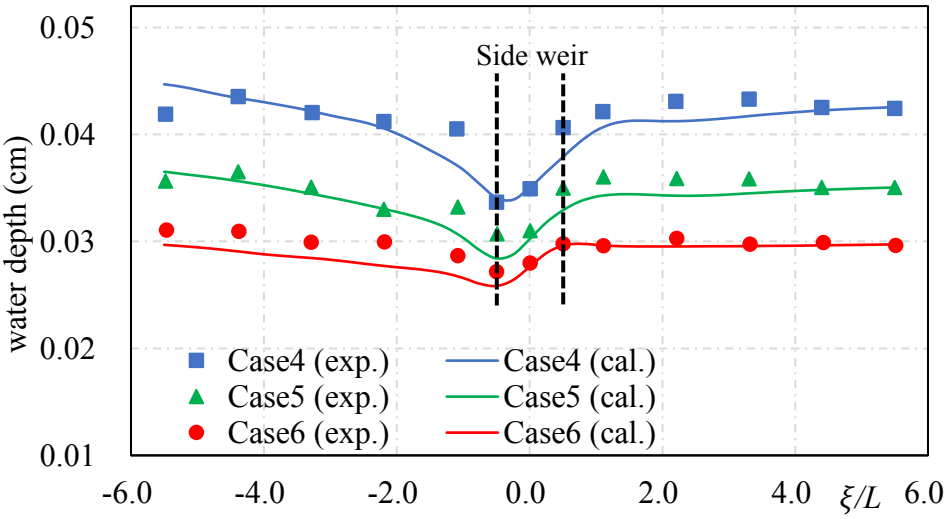

(b) Case 4, 5 and 6 (w/B=0)

Figure 3.16 Calculated and experimental water surface profiles

(2) Comparison of water surface profile in the streamwise direction

A non-dimensional parameter called relative weir height w/B is used to explain the effects of side weir height w by Kawamoto et al.[11]. **Figure 3.16** shows the comparisons of the streamwise water surface profiles along the center line of the channel when the w/B = 0.175 (Case 1, 2, and 3) and w/B = 0 (Case 4, 5, and 6), respectively. The horizontal coordinates are normalized by dividing the length of the side weir. Section 2 shown in **Figure 3.14**, is set as ξ/L = 0.

According to the experiments in cases of w/B = 0.175 shown in **Figure 3.16** (a), the water surfaces stay almost constant until reaching where ξ/L = -1.5 and then start to drop slightly. The water depths rise slightly after crossing the side weir, and the degree of growth in water depth increases with a more significant inflow rate. In the cases of w/B = 0 shown in **Figure 3.16** (b), the water depths from ξ/L = -5.5 continue to drop regardless of the inflow rate until Section 1, where the water depth reaches its lowest section. After passing Section 1, the water levels rise rapidly and start to remain stable at ξ/L = 3.5 downstream. Comparing the cases of w/B = 0 with w/B = 0.175, it should be noted that smaller relative height causes a significant change in water surface fluctuation. According to **Figure 3.16**, it is clear that the numerical model can predict well the fluctuation pattern of the water surface profile at the channel center in the streamwise direction. Nevertheless, the simulation results differ slightly from the experiments in the region of the side weir. For example, the predicted water depth at Section 3 in Case 1 and that at Section 1 in Case 4 is somewhat lower than the experimental results. Since the water surfaces, velocities and flow rates vary so drastically, when w/B = 0, around the side weir, simulated results and experimental results may be prone to differ from each other in this region. In this study, the computational mesh interval in channel bend is 3°, and only 5 meshes in the streamwise direction were used to form the side weir, which may be slightly rigid to capture the dramatic water surface variation. In addition, the volume correction used to prevent numerical diffusion may make water surface distribution smooth. Therefore, a numerical simulation with finer mesh will be conducted and the method to capture the dramatic water surface variation will be studied in a future study.

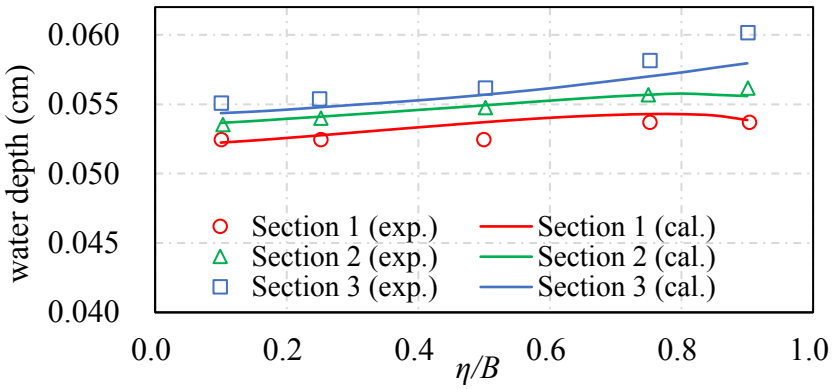

(a) Case 1 (Q_{IN} = 0.0042m^3/s, w/B = 0.175)

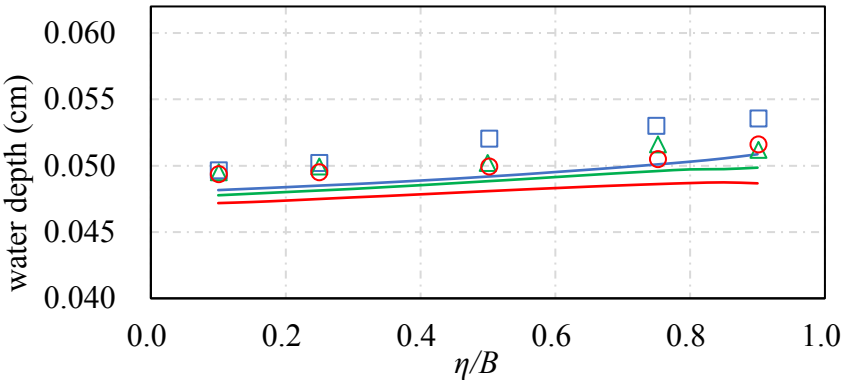

(b) Case 2 (Q_{IN} = 0.003m^3/s, w/B = 0.175)

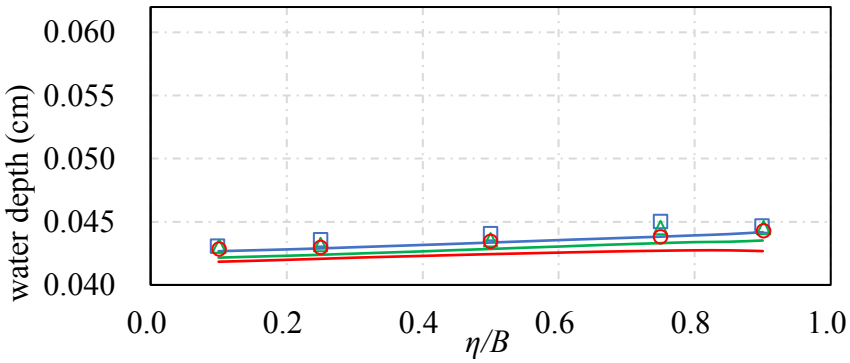

(c) Case 3 (Q_{IN} = 0.002m^3/s, w/B = 0.175)

Figure 3.17 Water surface profile in transversal direction

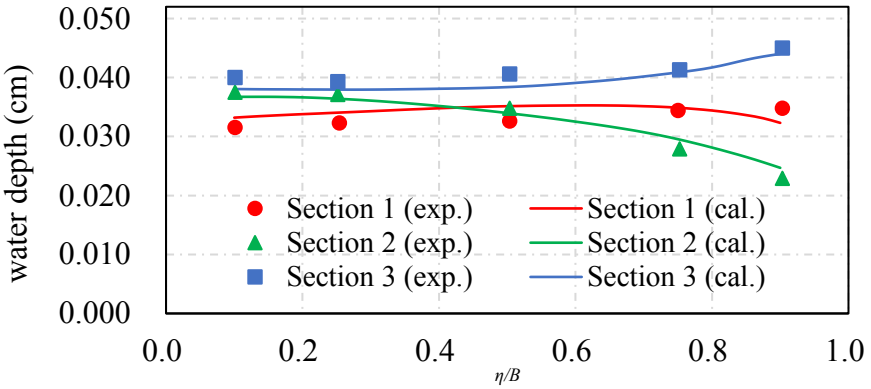

(d) Case 4 (Q_{IN} = 0.0042m^3/s, w/B = 0)

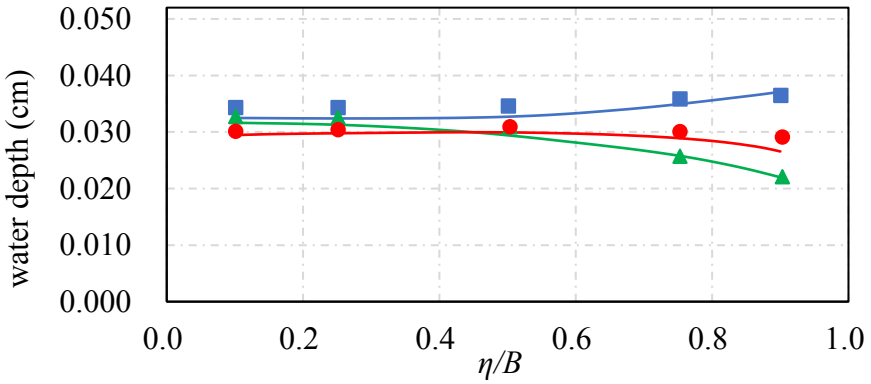

(e) Case 5 (Q_{IN} = 0.003m^3/s, w/B = 0)

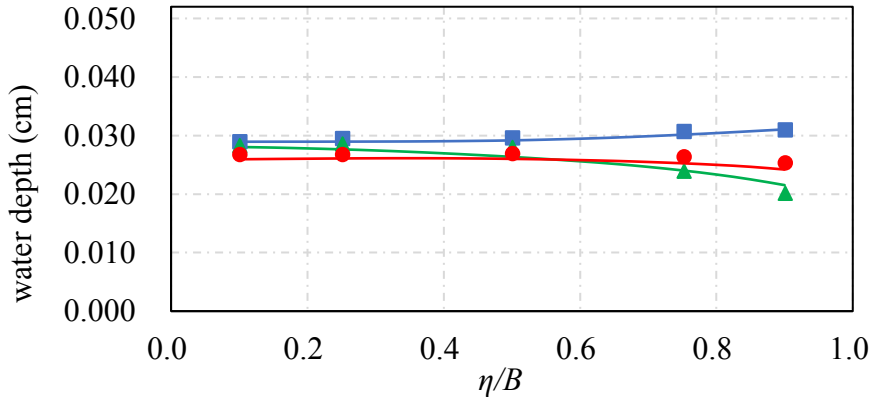

(f) Case 6 (Q_{IN} = 0.002m^3/s, w/B = 0)

Figure 3.17 Water surface profile in transversal direction

(3) Comparison of water surface profile in the transversal direction

Figure 3.17 shows each transversal water depth profile in the cases of w/B = 0.175 and w/B = 0. The distance from inner bank η is normalized by dividing with the width of channel B. Where, $\eta/B = 0$ represents the inner bank wall and $\eta/B = 1$ represents the outer bank wall.

According to experimental results in **Figure 3.17** (a), **Figure 3.17** (b), and **Figure 3.17** (c), water depths at the inner bank are lower than the outer bank in each section. As the upstream inflow Q_{IN} rate increases, the effect of centrifugal force gradually becomes larger, and the difference in water depth between Section 1 and Section 3 of the side weir also increases.

In cases of w/B = 0 shown in **Figure 3.17** (d), **Figure 3.17** (e), and **Figure 3.17** (f), the water surface profile varies a lot compared to cases of w/B = 0.175. In Section 1, the water surface profiles rise from the inner bank to the center of the channel and then start to drop slightly to the outer bank. In Section 2, water depths at the inner bank are much larger than those in the outer bank because of the significantly increased overflow rate and lower weir height. In Section 3, water surface profiles at the outer bank are obviously higher than the inner bank, which is similar to the results in the cases of w/B = 0.175.

Although predicted water depths in Case 2 are lower than the experimental results, other predictions agree well with the pattern of water surface variations observed in experiments. The problem in Case 2 is still unclear and will be discussed in a future study.

(4) Comparison of velocity distribution in the streamwise direction

Figure 3.18 shows the velocity distribution along the center line of the channel in the streamwise direction. On the vertical axis, the flow velocities U are normalized by dividing with $U_{\xi/B}$ = -5.5 located at the entrance of the curved channel.

According to the experiments in cases of w/B = 0.175 shown in **Figure 3.18** (a), flow velocities in the streamwise direction are reduced due to the overflow toward the side weir and keep constant after ξ/L = 3, and it also shows that the lower the inflow rate conditions, the less the decrease in velocities. In addition, the reduction rate of the flow velocity downstream is about 15~25%. On the other hand, in the case of w/B = 0 shown in **Figure 3.18** (b), it can be confirmed that the flow velocity increases by about 15~30% before the entrance of the side weir, and the velocities decrease rapidly as well as those in the case of w/B = 0.175, and the velocities start to stabilize at about ξ/L = 3-4. Numerical results shown in **Figure 3.18** indicate a good agreement with experiment data, except around Section 3 in Case 6 shown in **Figure 3.18** (b). In Case 6, the flow separation zone is larger compared to the other cases (See **Figure 3.19**). The scale of flow separation may affect the reproductivity of streamwise velocity distribution of about ξ/L = 1-3.

(5) Comparison of the ratio of overflow to inflow rate

Table 3.4 compares the measured and predicted ratio of overflow to inflow rate of the side weir. According to **Table 3.4**, when Q_{IN} = 0.003 (m^3/s) and w/B = 0, the predicted overflow ratio is about 10% less than the experiment, however, the predicted overflow depth and velocity distribution are very close to the experiment data, the reason for this problem is not yet well understood. In addition, other cases have a very good agreement with the experiment results within the difference of 2%.

Table 3.4 Ratio of overflow to inflow rate in curved channel

Case	Height of side weir w (mm)	Q_{IN} (m^3/s)	Q_{MEA}/Q_{IN} Exp.	Q_{MEA}/Q_{IN} Cal.
1	35	0.0042	0.249	0.248
2	35	0.0030	0.201	0.205
3	35	0.0020	0.113	0.121
4	0	0.0042	0.535	0.529
5	0	0.0030	0.627	0.553
6	0	0.0020	0.716	0.720

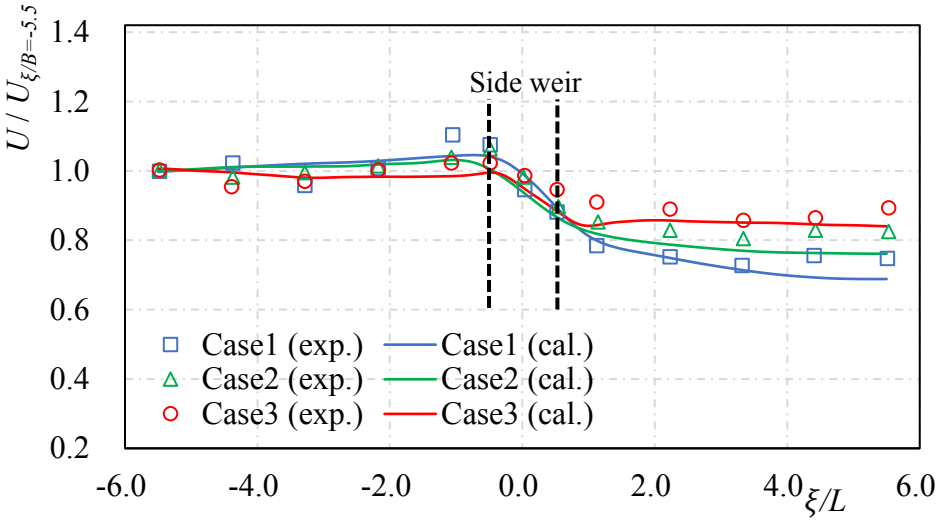

(a) Case 1, 2 and 3 (w/B=0.175)

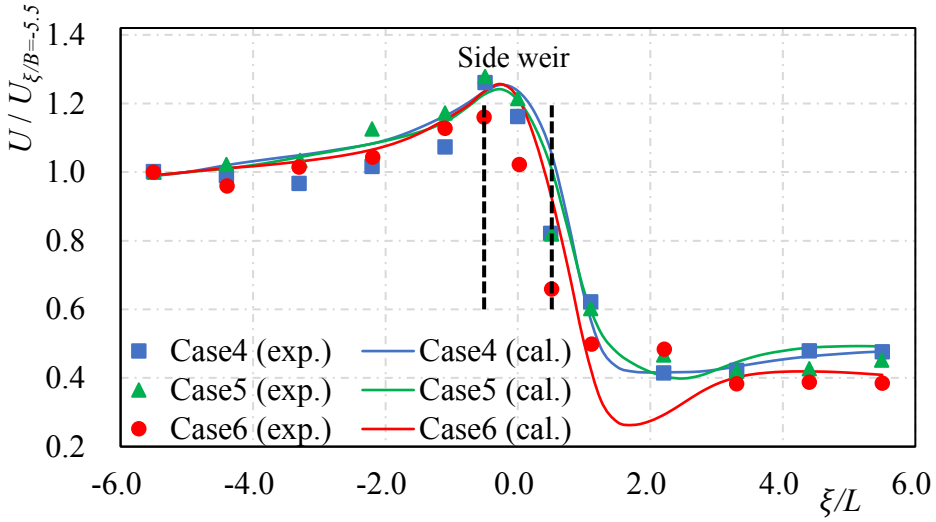

(b) Case 4, 5 and 6 (w/B=0)

Figure 3.18 Calculated and experimental velocity distribution in streamwise direction

(6) Velocity contours and streamlines

In the experiments[11], water surface profiles and velocity distributions are discussed in a streamwise direction, but they did not investigate the flow structure fully.

Figure 3.19 (a) and **Figure 3.19** (b) show the contours of depth-averaged velocity and streamlines in Case 1 and 3 respectively, and **Figure 3.19** (c) and **Figure 3.19** (d) show the contours of depth-averaged velocity and streamlines in Case 4 and 6 respectively. The side weir is between **y** = -0.1 (m) and **y** = 0.1 (m). According to the contours, in the side weir upstream, the velocity magnitude around the inner bank is larger than the outer bank in all 4 cases, which is a common feature in a normal curved open channel[8]. **Figure 3.19** shows that the flow velocities around the inner bank downstream of the side weir are significantly smaller than those around the outer bank. In addition, the effect of lateral overflow is significant, especially in Case 4 and Case 6 ($w/B = 0$). The velocity magnitude at the inner bank tends to be zero downstream of the side weir, and the separation zones can be observed along the inner bank downstream of Section 3. These separation zones were also observed by Faras et al.[8].

(7) Velocity Vectors and secondary flow

Figure 3.20 and **Figure 3.21** show the velocity vectors at Section 1, 2, and 3 in Case 1, 3, 4, and 6. According to the figure at Section 1 (**Figure 3.20** (a), **Figure 3.20** (d), **Figure 3.21** (a) and **Figure 3.21** (d)) the typical secondary flows can be observed in both weir height w/B=0.175 and w/B=0.

In Case 3, the flow rate is relatively small (Q_{IN}=0.002 (m^3/s)) and the overflow rate is only 11% of the inflow rate. Comparing the results at Section 1 and 3 shown in **Figure 3.20** (d) and **Figure 3.20** (f), the flow velocity downstream does not vary drastically, so the secondary flows downstream (at Section 3) of side weir does not differ much from that upstream (at Section 1) and can keep stable during crossing the side weir. Even in Section 2, in the center of the side weir, the secondary flow at the inner bank can be observed. In Case 1 (Q_{IN}=0.0042(m^3/s)), on the other hand, the overflow rate increases to more than twice as much as 25% of the total inflow rate, thus the downstream flow velocity variation is greater than that in Case 3. It should be noted that the downstream secondary flow to be split into two helical flows shown at Section 3 shown in **Figure 3.20** (c).

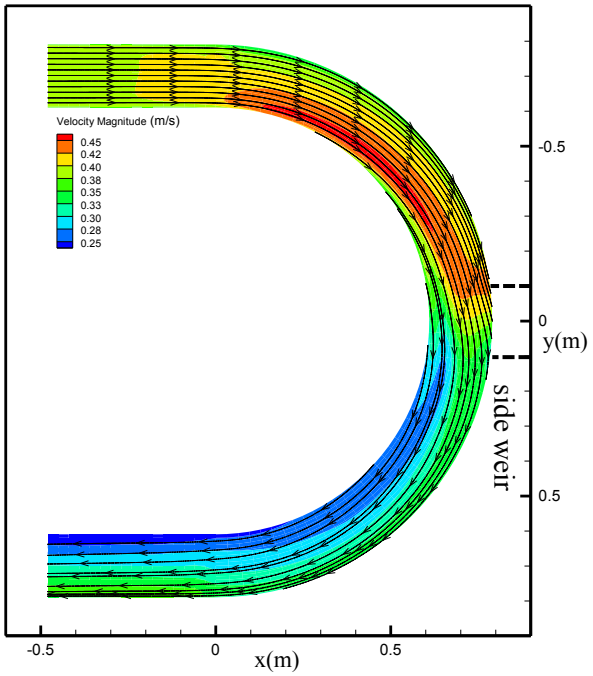

(a) Case 1 (Q_{IN}=0.0042m^3/s, w/B=0.175)

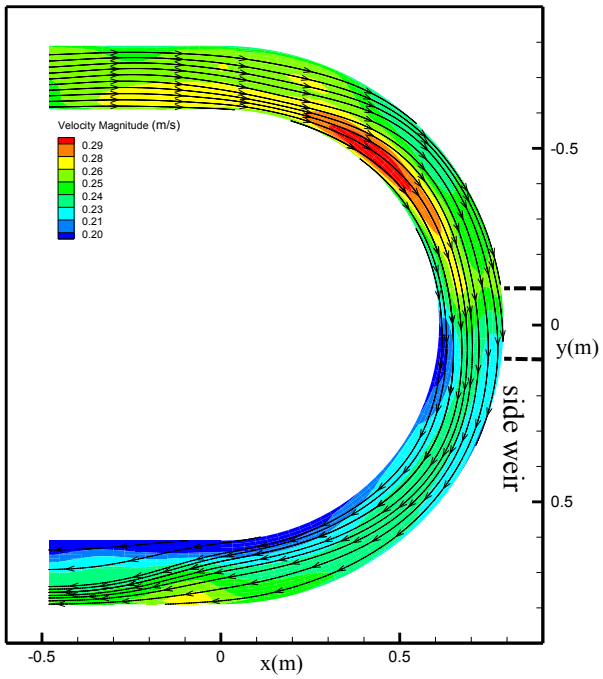

(b) Case 3 (Q_{IN}=0.002m^3/s, w/B=0.175)

Figure 3.19 Contours of depth averaged velocity and streamlines

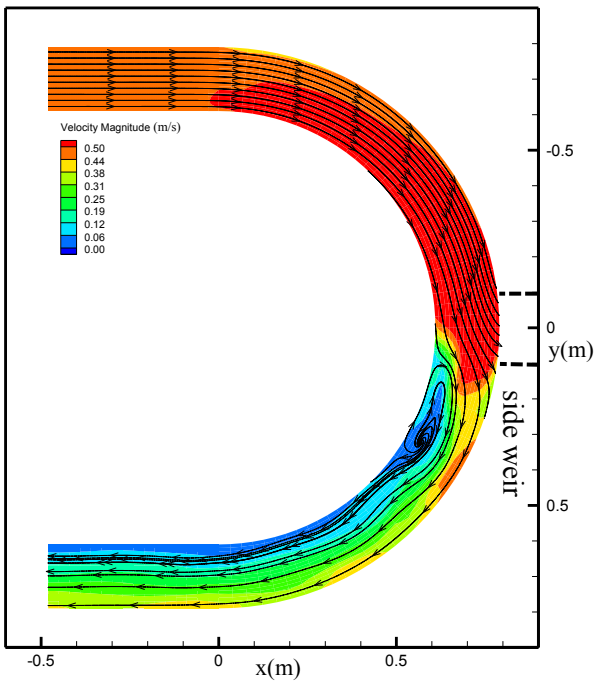

(c) Case 4 (Q_{IN}=0.0042m^3/s, w/B=0)

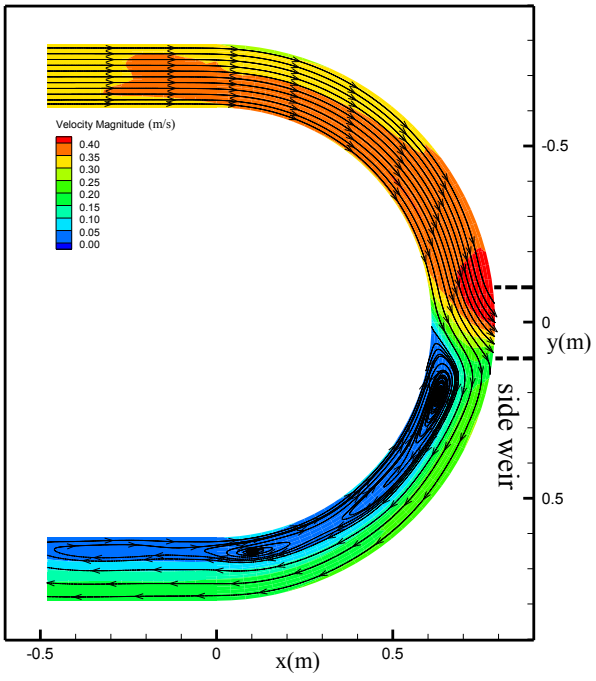

(d) Case 6 (Q_{IN}=0.002m^3/s, w/B=0)

Figure 3.19 Contours of depth averaged velocity and streamlines

According to **Figure 3.21**, because of the low relative height w/B = 0, water depth in both two cases decreased, and therefore, secondary flows upstream of the side weir become more intense compared to Case 1 and Case 3 (w/B = 0.175). In addition, due to the high ratio of overflow (52.9% in Case 4, 72.0% in Case 6), the flow velocity downstream decreases rapidly, causing the structure of the secondary flow downstream to change significantly. As **Figure 3.21** (e) illustrates, the flow in Section 2 is basically all directed to the outer bank. In **Figure 3.21** (f), the secondary flow is concentrated in the outer bank, due to a large amount of overflow to the side weir. In addition, at Section 3, the counteracting and reverse of the clockwise secondary flow can be observed in the inner bank.

When the flow rate increases to Q_{IN} = 0.0042 (m^3/s), the pattern of secondary flows at Section 1 shown in **Figure 3.21** (a) is similar to Case 1 and Case 3 shown in **Figure 3.20** (a) and **Figure 3.20** (d) respectively. At Section 2 indicated by **Figure 3.21** (b), dramatic changes in flow patterns are observed, due to the rapid overflow to the side weir and, the secondary flow in Section 3 is split into two helical flows observed in **Figure 3.21** (c), with the clockwise secondary flow concentrated at the bottom of the outer bank and the counterclockwise secondary flow appearing below the central water surface. The reason for this phenomenon could be that as the weir height decreases to zero, a large amount of water flows out of the side weir, causing the secondary flows that generally flow from the outer bank to the inner bank near the bottom of the channel, such as secondary flows in Section 1, to be forcibly redirected within the side weir area. This effect continues until the downstream end of the side weir. However, because of the impact of the downstream channel bend, the water surface at the outer bank rises, producing a clockwise secondary flow under the pressure gradient. The interaction of these two flow structures causes the secondary flow structure seen in **Figure 3.21** (c).

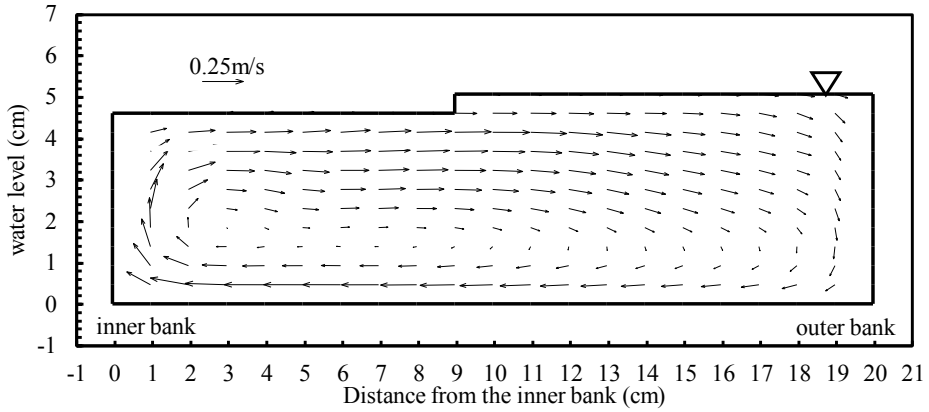

(a) Section 1 in Case 1
(Q_{IN}=0.0042m^3/s, w/B=0.175)

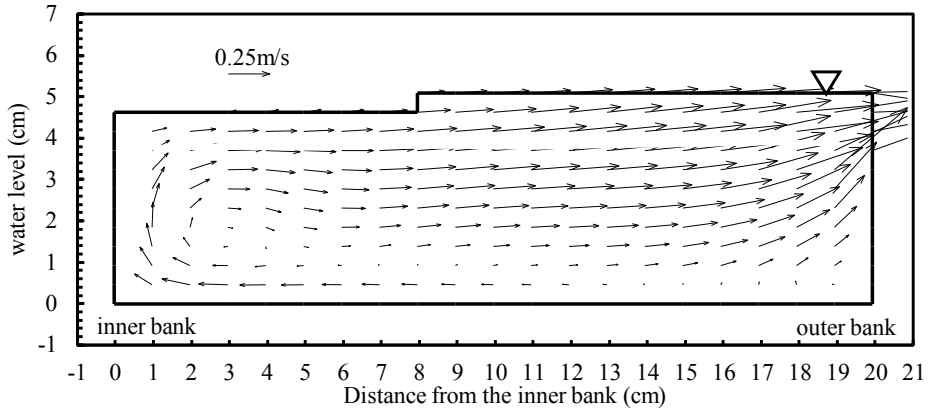

(b) Section 2 in Case 1
(Q_{IN}=0.0042m^3/s, w/B=0.175)

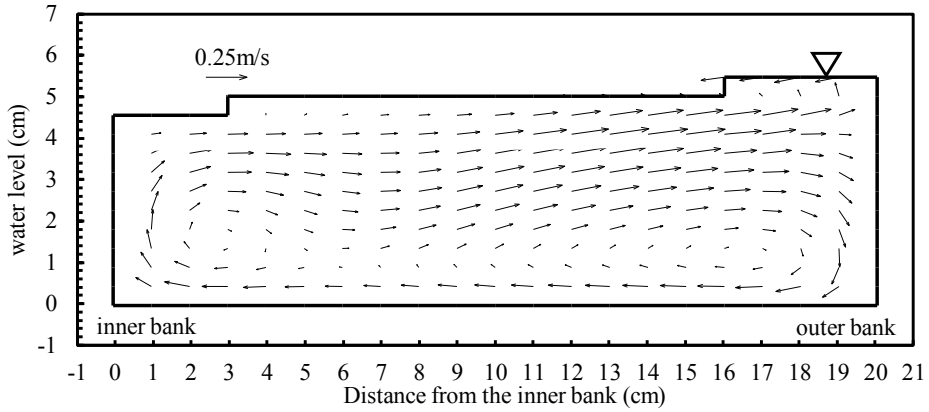

(c) Section 3 in Case 1
(Q_{IN}=0.0042m^3/s, w/B=0.175)

Figure 3.20 Velocity vectors in the transversal cross section (w/B = 0.175)

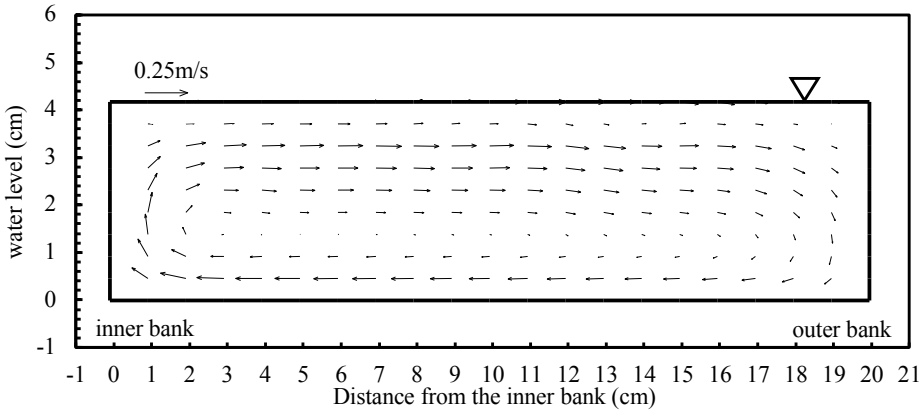

(d) Section 1 in Case 3
(Q_{IN}=0.002m^3/s, w/B=0.175)

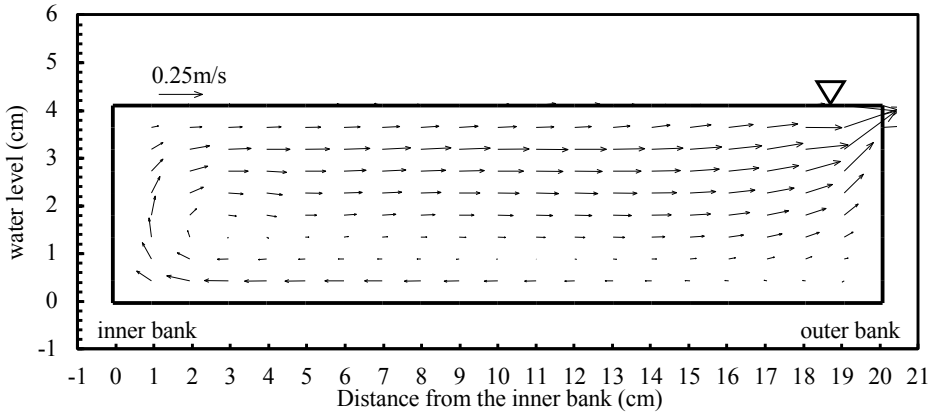

(e) Section 2 in Case 3
(Q_{IN}=0.002m^3/s, w/B=0.175)

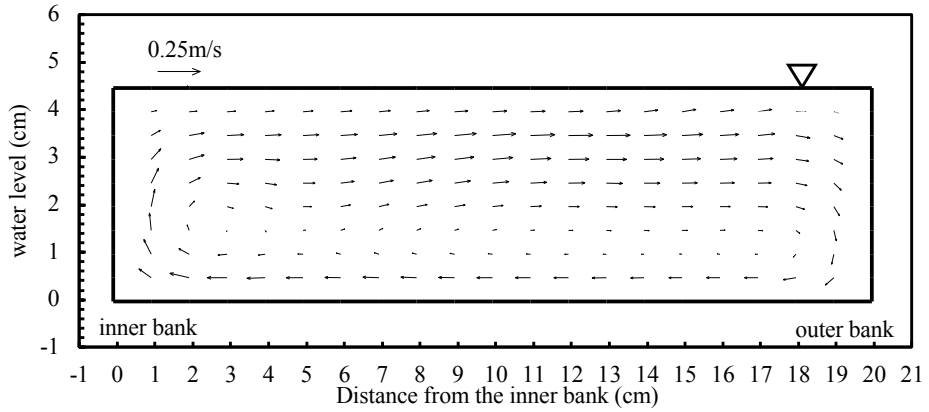

(f) Section 3 in Case 3
(Q_{IN}=0.002m^3/s, w/B=0.175)

Figure 3.20 Velocity vectors in the transversal cross section (w/B = 0.175)

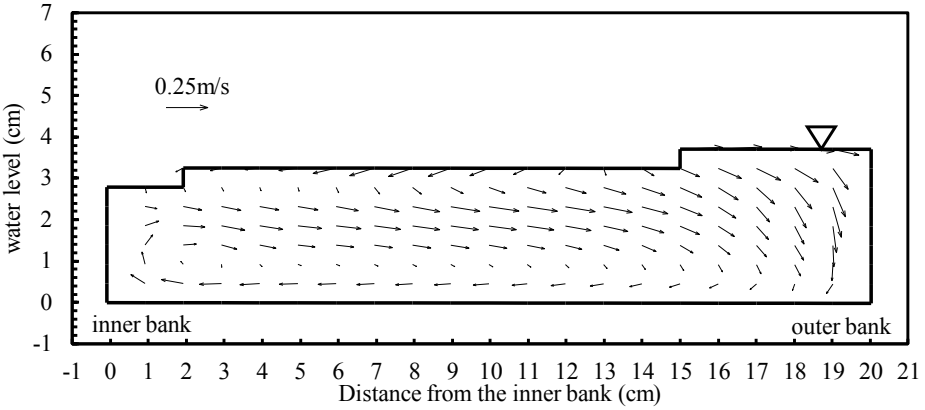

(a) Section 1 in Case 4
(Q_{IN}=0.0042m^3/s, w/B=0)

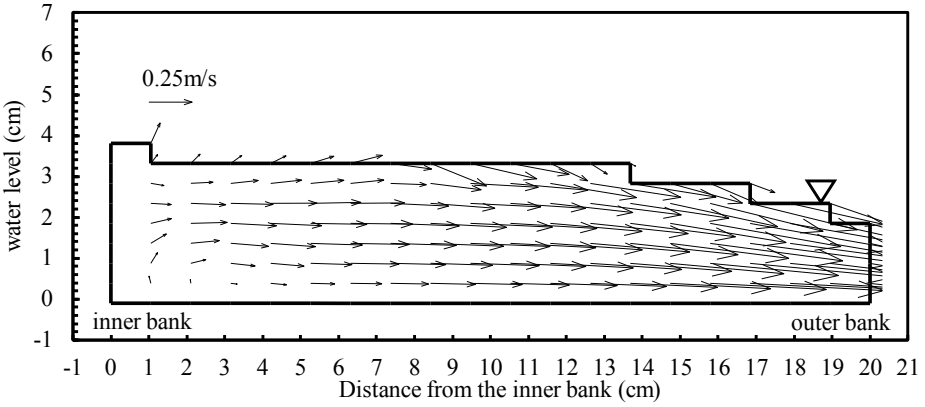

(b) Section 2 in Case 4
(Q_{IN}=0.0042m^3/s, w/B=0)

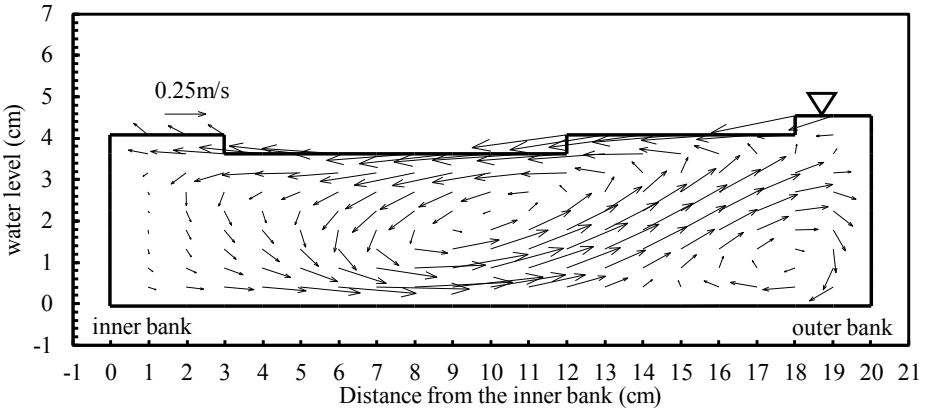

(c) Section 3 in Case 4
(Q_{IN}=0.0042m^3/s, w/B=0)

Figure 3.21 Velocity Vectors in the transversal cross section (w/B = 0)

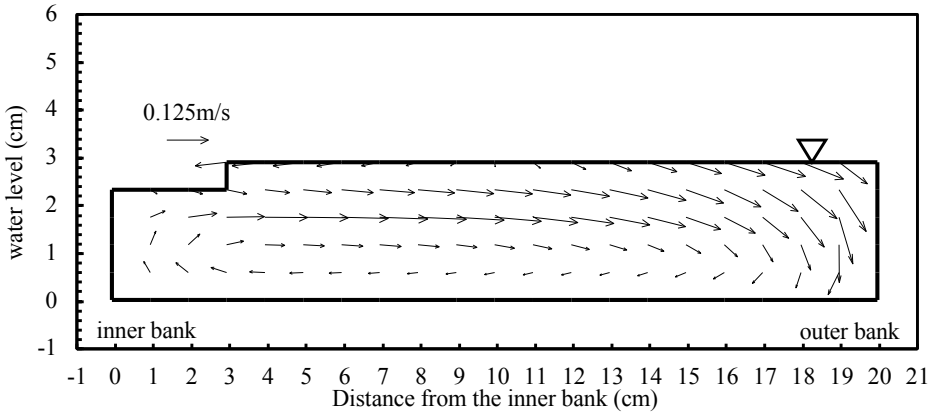

(d) Section 1 in Case 6
(Q_{IN}=0.002m^3/s, w/B=0)

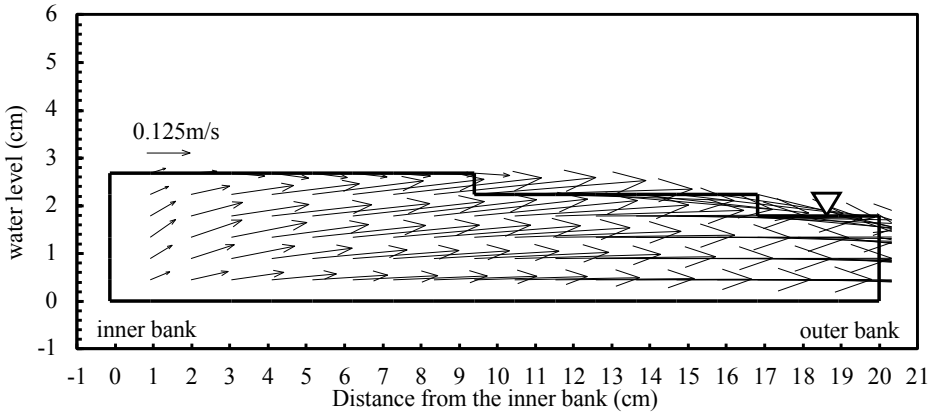

(e) Section 2 in Case 6
(Q_{IN}=0.002m^3/s, w/B=0)

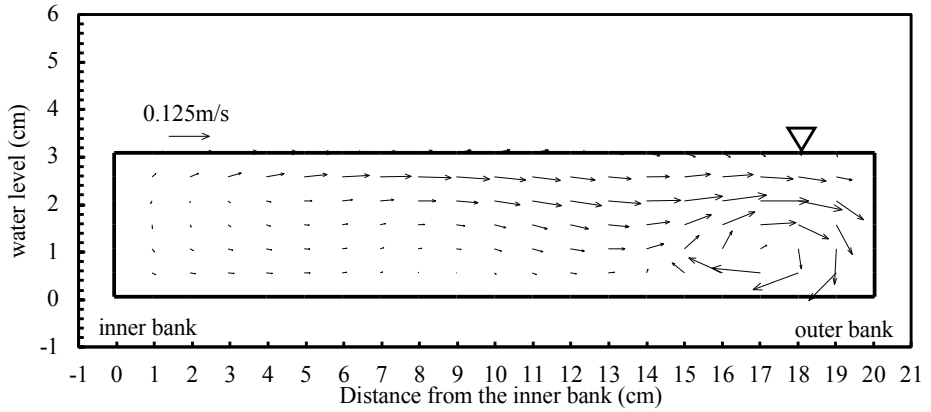

(f) Section 3 in Case 6
(Q_{IN}=0.002m^3/s, w/B=0)

Figure 3.21 Velocity Vectors in the transversal cross section (w/B = 0)

3.3 Summary

In this study, a 3D numerical flow model, coupling the density function method to calculate the water surface variations, on the boundary-fitted coordinate system is applied to simulate the experiments of side weir flows in straight and curved channels. Although there are some differences in the water surface profile and velocity distribution across the side weir interval, the whole trends in the experimental results are predicted well by the model. The conclusions obtained in this study are summarized as follows:

(1) In comparison with the experimental outcomes observed in straight channels[10], this numerical model replicates the distributions of water surface elevation and flow velocity. As depicted in **Figure 3.4**, there is a notable and abrupt elevation in the water surface near Section 3 subsequent to the occurrence of overflow. Upon comparing the vector distributions in **Figure 3.6, Figure 3.8** and **Figure 3.10** of the three cases in the straight channel with side weir, a spiral flow in the latter half of the side weir can be observed in each case. This spiral flow is likely induced by the elevation of the water surface, leading to increased pressure, as seen in **Figure 3.12**, and consequently, the generation of flow under the action of a pressure gradient.

(2) According to **Figure 3.7**, **Figure 3.9** and **Figure 3.11,** even in a straight channel, the presence of a side weir can give rise to secondary flows downstream of the side weir near Section 3, normally observed in curved channels. This secondary flow, distinct from the typical secondary flow observed in meandering channels, is not induced by the centrifugal forces at bends, but rather results from the overflow that create a tendency for the downstream flow towards the side weir. The flow's impact against the lateral walls elevates the water surface downstream edge of the side weir. Under the influence of these factors, a secondary flow in straight channels is generated.

(3) By comparing with the experiment[11], it can be seen that this numerical model can well predict the trend of water surface variation around the side weir in the curved channel. Although the flow velocity distribution near Section 3 in Case 6 is relatively different from the experimental results, the overall variation trend, and the flow velocity distributions upstream and downstream are in good agreement with the experiment shown in **Figure 3.16**, **Figure 3.17**, and **Figure 3.18**. Moreover, according to **Table 3.4**, the model can accurately calculate the overflow rate, and the trend of the overflow rate with the different relative weir height *w/B*. In the case of

w/B = 0.175, the overflow rate Q_{MEA} increases as the inflow rate Q_{IN} increases. The high inflow rate results in higher overflow depth and the overflow rate are maximum in the case of a higher inflow rate. However, in the case of w/B = 0, the overflow rate is inversely proportional to the inflow rate Q_{IN}, a larger inflow rate causes a smaller overflow rate. The direction of streamlines between the high and low discharge cases are different, corresponding to the flow fields along the channel and it was found that the overflow rate is maximum in the case of low inflow rate. The calculated values of all cases are almost consistent with the experimental values except for Case 5, which differs from the experiment by about 10%. Therefore, it can be concluded that the numerical model can simulate the flows around the side weir with two outlets relatively reliably.

(4) Relative weir height can largely influence the formation of separation zones and flow characteristics both upstream and downstream. The separation zones that occurred around downstream of the side weir can be observed in low relative weir height w/B = 0 and become more obvious with a larger inflow rate. Even if the flow rate is increased, the flow separation region remains unobservable for the high relative weir height w/B = 0.175. Moreover, in the case of w/B = 0.175, the maximum flow rate occupies the inner bank of the upstream channel bend, which is similar to the single bend flows. However, when the relative weir height is w/B = 0, the maximum depth-averaged velocity occurs at the outlet of the overflow weir, which is considered to be the factor of gravity.

(5) For secondary flows within the side weir region, the difference in relative weir heights can bring considerable variation to the structure of the secondary flows. In the case of higher relative weir heights w/B = 0.175, the secondary flows upstream and downstream of the lateral overflow and the water surface profile are similar to the secondary flow structures in single channel bend flows, such as superelevation at the outer bank of the water surface, etc. The change in flow rate only affects the flow velocity and the degree of water surface superelevation. However, the secondary flows at the outer bank change significantly in the side weir interval due to the overflow from the wier, and the flows from the outer to the inner bank along the bed weaken. Therefore, for lateral overflow, more consideration can be given to the damage of the overflow to the weir rather than the change in flows near the bed. For

the case of lower relative weir height w/B = 0, the secondary flows upstream are almost the same as when the relative weir height is higher, but the secondary flows downstream are very different. Because the overflow effect is so strong, the secondary flows at the bottom downstream no longer extend to the inner bank and the scale of secondary flows is restricted to just a corner of the outer bank.

Reference

1) DeMarchi, G. : Essay on the performance of lateral weirs, *L'Energia electrica Milan*, Vol. 11, No. 11, pp. 849-860, 1934.
2) Hager, W. H. : Lateral outflow over side weirs, *Journal of Hydraulic Engineering*, ASCE, Vol. 113, No. 4, pp. 491-504, 1987.
3) Chong, H. : Discharge coefficient of lateral diversion from trapezoidal channel, *Journal of Irrigation and Drainage Engineering*, ASCE, Vol. 117, No. 4, pp. 461-475, 1991.
4) Swamee, P. K., Pathak, S. K. and Ali, M. S. : Side-weir analysis using elementary discharge coefficient, *Journal of Irrigation and Drainage Engineering*, ASCE, Vol. 120, No. 4, pp. 742-755, 1994.
5) Borghei, S. M., Jalili, M. R. and Ghodsian, M. : Discharge coefficient for sharp crested side weirs in subcritical flow, *Journal of Hydraulic Engineering*, ASCE, Vol. 125, No. 10, pp. 1051-1056, 1999.
6) Ranga Raju, K.G., Gupta, S.K. and Prasad, B.: Side weir in rectangular channel, *Journal of the Hydraulics Division*, ASCE, Vol.105, No. 5, pp.547-554, 1979.
7) Bagheri, S. and Heidarpour, M. : Characteristics of g flow over rectangular sharp-crested side weirs, *Journal of Irrigation and Drainage Engineering*, ASCE, Vol. 138, No. 6, pp. 541-547, 2012.
8) Fares, Y. R. and Herberton, J. G. : Behaviour of flow in a channel bend with a side overflow channel, *Journal of Hydraulic Research*, IAHR, Vol. 31, No. 3, pp. 383-402, 1993.
9) Asai, K., Kawamoto, N., Shiromizu, K. and Shiromizu, H. : Study on Lateral over flow from outer side breach and inner side breach in curved channel, *Journal of Japan Society of Civil Engineers*, *Ser.B1 (Hydraulic Engineering)*, Vol. 74, No. 4, pp. 637-642, 2018. (in Japanese)

10) Kawamoto, N., Asai, K. and Shirozu, H. : Experiment study of flow pattern around lateral overflow weir in curved and straight channels, *Journal of Japan Society of Civil Engineers*, *Ser. B1 (Hydraulic Engineering)*, Vol. 75, No. 5, pp. 463-468, 2019. (in Japanese)

11) Kawamoto, N., Asai, K. and Shiromizu, H. : Water surface and velocity profiles in curved channel with lateral over flow, *Journal of Japan Society of Civil Engineers*, *Ser.B1 (Hydraulic Engineering)*, Vol. 74, No. 5, pp. 775-780, 2018. (in Japanese)

12) Akiyama, J., Shige-eda, M., Ohba, K., Yamao, M. and Monden, R. : Predictions and characteristics of dyke breach flows in straight and meandering channels, *Journal of Japan Society of Civil Engineers*, *Ser.B1 (Hydraulic Engineering)*, Vol. 68, No. 4, pp. 1021-1026, 2012. (in Japanese)

13) Jia, Y. and Wang, S. S. Y. : Numerical model for channel flow and morphological change studies, *Journal of Hydraulic Engineering*, ASCE, Vol. 125, No. 9, pp. 924-933, 1999.

14) Kimura, I. Uijttewaal, W. S. J., Hosoda, T. and Balen, W. V. : RANS Computations of mild curved open channel flows focusing on an outer-bank cell, *Proceedings of Hydraulic Engineering*, Vol. 52, pp. 1009-1014, 2008. (in Japanese)

15) Bagherifar, M., Emdadi, A., Azimi, H., Sanahmadi, B. and Shabanlou, S. : Numerical evaluation of turbulence flow in a circular conduit, *Applied Water Science*, Vol. 10, No. 35, 2020.

Chapter 4

Model applications of 3D numerical model considering surface and seepage flows in curvilinear coordinate system

4.1 Preliminaries

In natural rivers, the riverbeds and levee slopes are permeable. Several experiments[1),2),3)] systematically investigated the processes of dike breaching due to overtopping flows under various hydraulic conditions. However, the effects of seepage flow during the dike breaching process have not been thoroughly discussed and are often overlooked in these studies. This is because the seepage flow rate is much smaller compared to the flow rate in the main open channel, leading to the assumption that it has little impact on the main open channel flows. Yoden et al.[4)] carried out hydraulic experiments illustrating the impact of dike body saturation on dike breaching caused by overflows. Their findings indicate that a fully saturated dike is more susceptible to erosion. Therefore, it is important to note that the seepage flow can significantly influence the flow characteristics near the permeable riverbed and comprehending the mechanisms of interaction between surface and seepage flows and flow patterns around the riverbed boundary, which is closely linked to the shear stress and velocity distribution near the riverbed, is crucial for the sediment transport process.

Chen & Chiew[5)] and Cheng & Chiew[6)] conducted a series of experiments to investigate the velocity distributions near the permeable riverbed by introducing injection and suction processes. Their findings reveal that the injection of fluid through the permeable riverbed resulted in a decrease in velocity near the riverbed, while suction caused an increase in velocity. These observations highlight the influence of the infiltration process on the velocity distribution and emphasize the importance of considering seepage flow effects when studying flow dynamics near the riverbed. Furthermore, Rao et al.[7)] conducted experiments that demonstrated the influence of both injection and suction on the magnitude of bed shear stress. Additionally, Jewel et al.[8)]

investigated the effects of injection on the critical shear stress and incipient motion of sand particles. These studies show the complex interplay between surface and seepage flows, bed shear stress, and sediment transport processes, providing valuable insights into the mechanisms underlying the interaction between seepage flows and flow patterns near the riverbed.

For numerical studies of the open channel flows, several numerical models have been proposed to simulate the riverbed deformation and the dike breaching process. Most of these models are developed by 2D shallow water equations[9),10),11)]. However, the flow fields within a curved channel and above permeable bed are quite complex and exhibit intricate three-dimensional flow structures, which cannot be fully captured by the shallow water approach. Consequently, the limitations of the shallow water model in accurately simulating these processes necessitate the utilization of a 2D model.

This chapter incorporates the 3D flow model in a generalized curvilinear coordinate system shown in Chapter 2 with a porous media approach. By considering the interactions between surface and seepage flows, and accounting for complex geometries, the model enables more accurate predictions in practical engineering applications. The model has been validated through its application to various experimental scenarios, including lateral seepage in permeable porous material, dam break flows over permeable porous bed, open channel flows with bed suction, and curved channel flows over a deformed riverbed.

4.2 Governing equation with porous media approach

In this chapter, to enhance capability of the numerical model shown in Chapter 2 in simulating both surface and seepage flows, the porous media approach is integrated into this numerical model. The governing equations are presented below.

[continuity equation]

$$\frac{\partial(1-c)\rho\Phi}{\partial t}+\frac{1}{\sqrt{g}}\frac{\partial(1-c)\rho\Phi\sqrt{g}V^i}{\partial\xi^i}=0 \tag{4.1}$$

[momentum equation]

$$\frac{\partial(1-c)\rho V^i}{\partial t}+\nabla_j\left[(1-c)\rho V^iV^j\right]=(1-c)\rho G^i \tag{4.2}$$

$$-(1-c)g^{ij}\nabla_j p + 2\nabla_j(1-c)\mu S^{ij} + \nabla_j[-(1-c)\rho\overline{v^i v^j}] + R^i$$

where t: time, ξ^i: spatial coordinates of the computational space, Φ: density function, c: volume fraction in the solid phase, V^i: contravariant component of velocity vector, v^i: contravariant component of the turbulent velocity vector, p: pressure, ρ: the density of fluid, g: determinate of metric tensor, μ: viscosity coefficient of fluid, g^{ij}: contravariant components of metric tensor, S^{ij}: rate of strain tensor, G^i: contravariant component of gravity.

The drag force R^i exclusively exists within the porous region and is modeled in accordance with the Darcy's law:

$$R^i = \frac{\rho G(1-c)^2}{K} V^i \tag{4.3}$$

where K is hydraulic conductivity, and G is the magnitude of gravity.

Note that the solid volume fraction c in governing equations varies in liquid-solid interface, therefore c in the interface cell is calculated by following equation.

$$c = \lambda(z_{bc}/\Delta z) \tag{4.4}$$

where λ is the porosity of bed material, z_{bc} is the solid height in one interface cell, Δz is cell size in z direction.

The friction velocity u_* is evaluated by wall function for rough wall (4.5).

$$\frac{V_p}{u_*} = \frac{1}{\kappa} ln \frac{z_p}{k_s} + A_r \tag{4.5}$$

where, k_s is representative distance normal to the bed (roughness height), κ is Kármán constant (= 0.41) and A_r is a constant of 8.5, V_p is the velocity magnitude at center of the first layer of mesh above the bed. The turbulence kinematic energy k and turbulence energy dissipation rate ε are assessed utilizing a wall function for rough wall (4.5) based on the log-law.

Note that the turbulence calculation in this model is only confined to the surface flow, while the seepage flow within the porous media does not incorporate turbulence model.

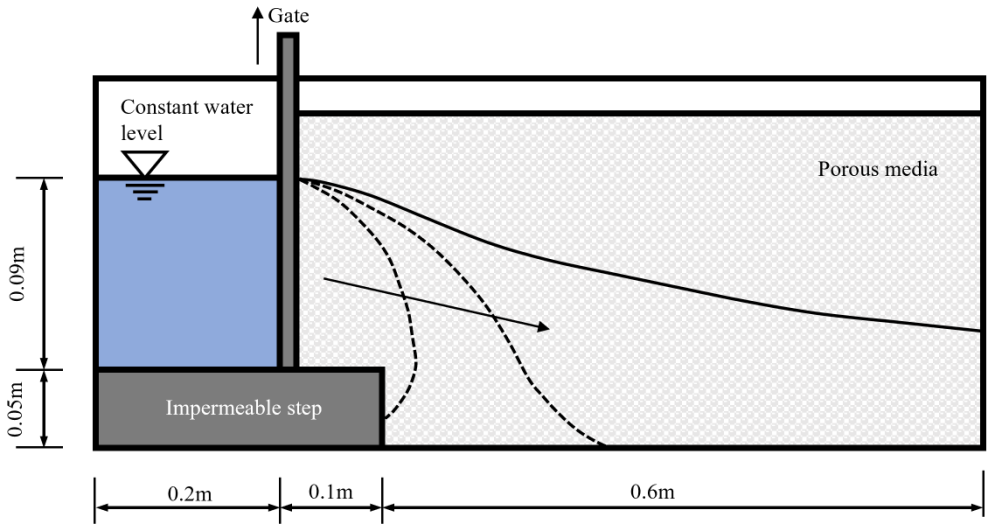

Figure 4.1 Schematic diagram of lateral seepage flows in porous media[12)]

4.3 Model applications

4.3.1 Application to lateral seepage in permeable porous material

(1) Computational conditions

The numerical model is applied to simulate experiment of the lateral seepage flow in straight channel carried out by Ghimire et al.[12)]. The schematic diagram of the experimental flume is presented in **Figure 4.1.** The hydraulic conditions of experiment are provided in **Table 4.1**. The rectangular computational mesh in streamwise ξ, transverse η, and vertical ζ directions consist of 180, 5, and 40 elements, and the mesh sizes in each direction are set to 0.5 (cm), 1 (cm), and 0.5 (cm), respectively.

(2) Simulation results and discussion

Figure 4.2 presents the water surface profile and velocity vectors within the porous media at various time steps during the simulation, and **Figure 4.3** provides a comparison of surfaces between the experimental data and the simulation results. **Figure 4.2** and **Figure 4.3** indicate that the numerical model can accurately predict the seepage flow through porous media, encompassing both the propagation speed of the seepage front and its water surface. For instance, as depicted in **Figure 4.3** (b), the water surface exhibits a slight depression around **x** = 0.12 (m) due to the step's influence. This pattern has been successfully captured by the numerical model, which substantiates its reliability

Table 4.1 Experimental conditions[12)]

Diameter of glass bead (mm)	5
Concentration of solid particles	0.6
Initial water level (m)	0.09
Flume dimensions L, B and H (m)	0.9, 0.1, 0.15

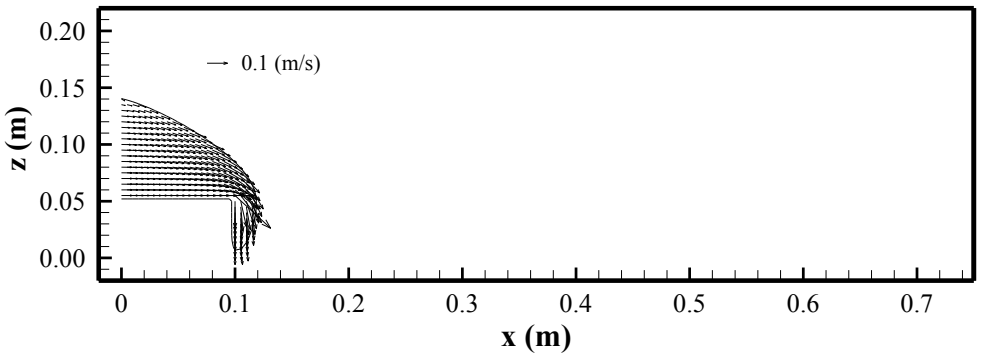

(a) t = 1 (s)

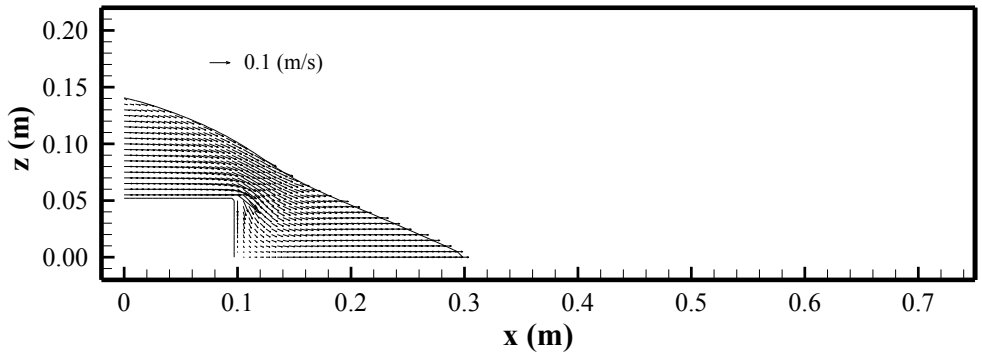

(b) t = 3.75 (s)

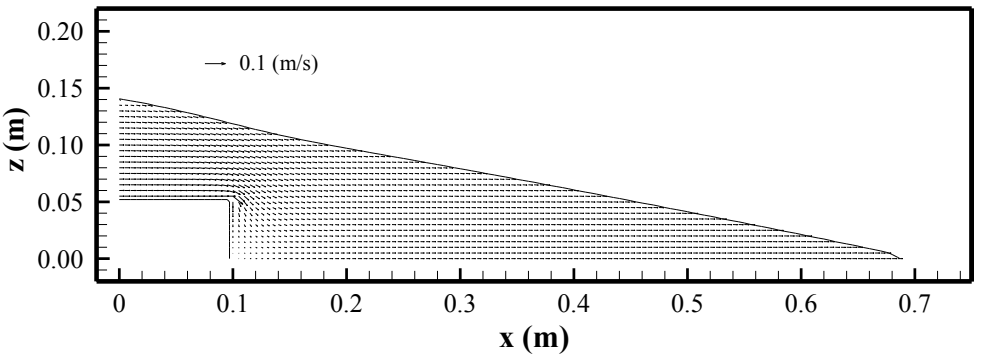

(c) t = 13 (s)

Figure 4.2 Water surface profiles and velocity vectors

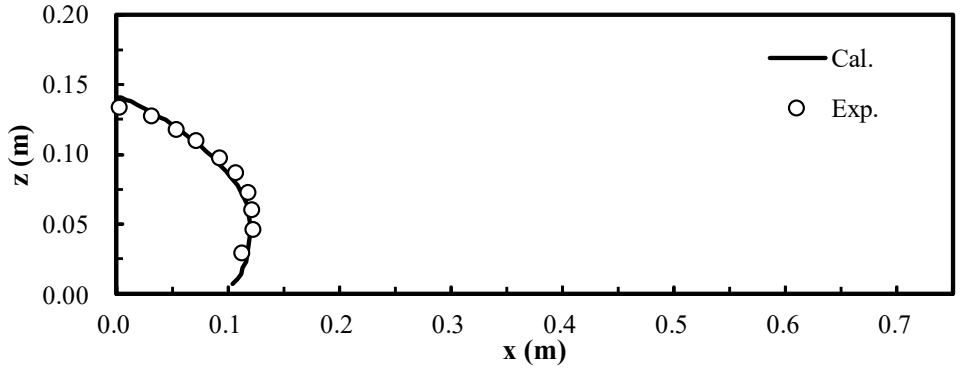

(a) t = 1 (s)

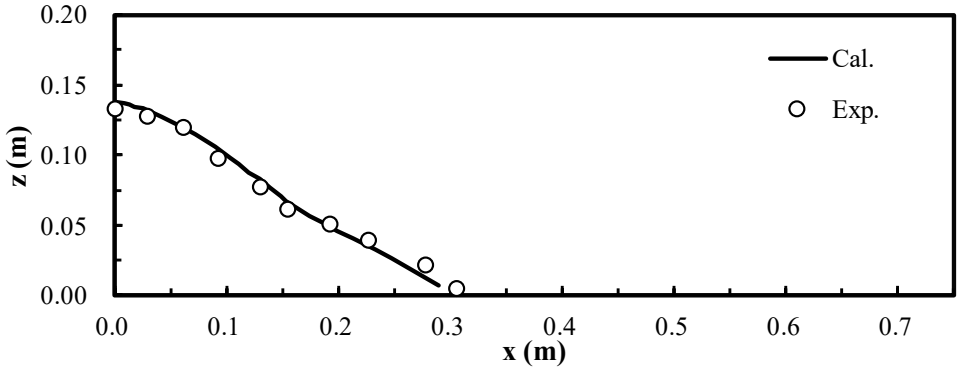

(b) t = 3.75 (s)

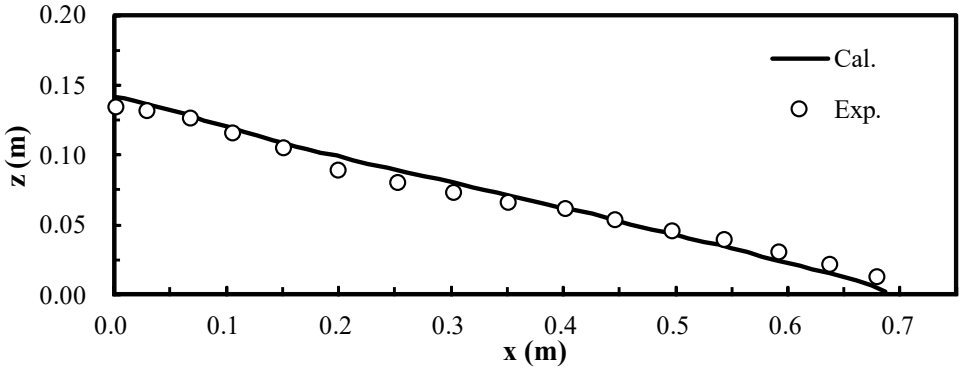

(c) t = 13 (s)

Figure 4.3 Comparisons of water surface profiles

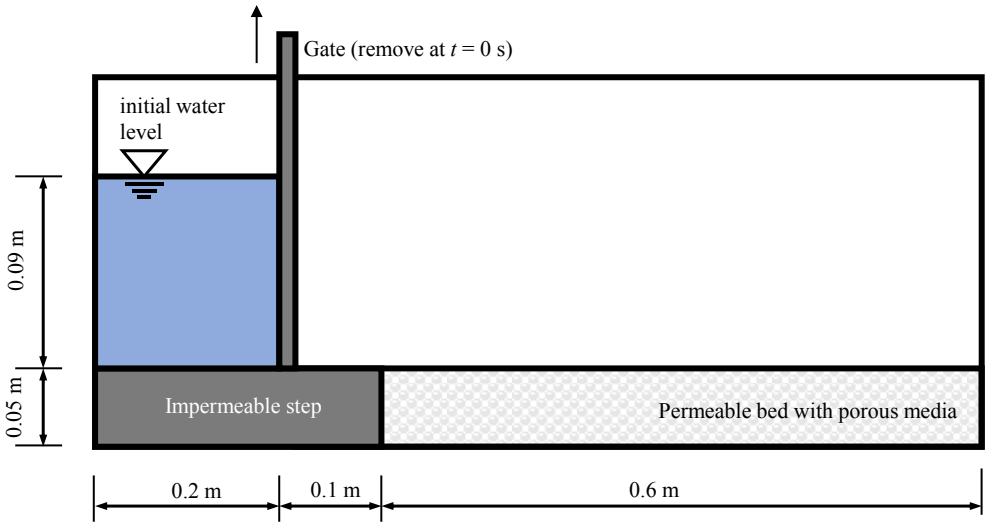

Figure 4.4 Schematic diagram of dam break flows over permeable bed[12)]

4.3.2 Application to dam break process over a permeable porous bed

The dam break problem is a classic benchmark test in computational fluid dynamics, frequently employed to assess the accuracy of numerical models. This simulation tries to replicate the dam break phenomenon over a bed composed of porous media, thereby evaluating the model's precision in predicting water surface profiles and the seepage flow.

(1) Computational conditions

The numerical model is applied to simulate the experiment of the dam break flows over permeable porous bed in a straight channel carried out by Ghimire[12)]. The schematic diagram of the experimental flume is presented in **Figure 4.4**. The flow domain comprises a section with an impervious step and a subsequent section with a dry permeable porous bed. The porous bed consists of glass beads extending up to a height of 0.05 (m) and a length of 0.6 (m) above the impervious bottom of the flume. The conditions of experiment are provided in **Table 4.2**. The rectangular computational mesh is the same as the mesh in Chapter 4.3.1. In the experiment[12)], a water reservoir is initially filled with water at an initial water level of 0.09 (m). At one end of the reservoir, a gate is installed to create a temporary obstruction. Subsequently, the gate is rapidly removed, allowing the water to flow freely and propagate downstream under the influence of gravity.

Table 4.2 Experimental conditions[12)]

Diameter of glass bead (mm)	12
Concentration of solid particles	0.6
Initial water level (m)	0.09
Flume dimensions L, B and H (m)	0.9, 0.1, 0.15

(2) Simulation results and discussion

Figure 4.5 presents the water surface profiles and velocity vectors at various time steps during the simulation, while **Figure 4.6** provides a comparison of water surfaces between the experimental data[12)] and the simulation results.

As depicted in **Figure 4.5**, the flow in this scenario is composite, contained both surface and seepage flows. The flow occurs above and within the porous medium, as can be distinctly observed in the figures. In **Figure 4.5** (a), most of the water is situated above the bed with a minor portion within the porous medium, while the leading edge continues to advance, forming a surface flow. In addition, it is observed that the fastest seepage rates are located at a central position (**x** = 0.32 (m)). As the leading edge moves forward, the mass of liquid above the riverbed gradually diminishes with an accompanying decrease in velocity. By **Figure 4.5** (c), most of the water resides within the porous layer, and a slight upward bulge near **x** = 0.3 (m) on the water surface replicates the water surface profile observed in the experiments well.

Compared to the simulation results by Ghimire [12)], this simulation has better reproduction in both water surface profiles and seepage flows. In their simulations, the leading edge of the water surface is rather rounded, whereas the actual water surface profile is quite sharp, as illustrated in **Figure 4.5** (a), **x** = 0.4 (m). Additionally, the seepage flow within the porous medium in the experiments does not descend in a stepped manner and then move to the right. Instead, it is fastest in the middle, subsequently spreading to both sides. Furthermore, at t = 0.4 (s), the seepage front has already surpassed the water surface above the riverbed, as shown in **Figure 4.5** (b)**.** At t = 1.0 (s), the upward bulge near **x** = 0.3 (m) on the water surface does not appear in their simulations.

Figure 4.6 demonstrates a favorable agreement with the experimental observations when simultaneously simulating surface and seepage flows. This straightforward and simple application serves to illustrate the efficiency of the flow model

in accurately simulating surface and seepage flows in porous media, which holds significant importance for subsequent applications.

Figure 4.7 shows the evolution of the pressure in the simulation. The figures clearly illustrate the distribution of hydrostatic pressure in open channel flow and porous media during a dam break event. It is evident that this is a gravity-driven flow where, within the porous medium, the percolation progresses to the right under the influence of a pressure gradient. Furthermore, when compared to the simulation result[12)], the pressure distribution is more reasonable and accurate. For instance, in the simulation result[12)], the pressure contours at the front of the flow at $t = 0.2$ (s) present a rounded shape, which is inconsistent with the sharp water surface observed in the experiment, indicating that the pressure distribution should not be as depicted. Therefore, the simulations from this model are more precise.

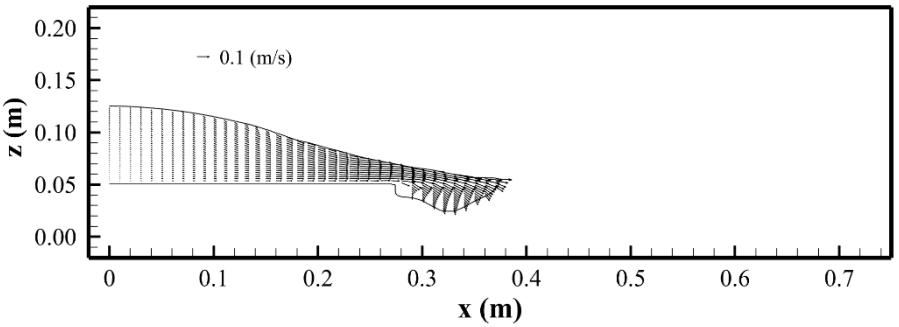

(a) t = 0.2 (s)

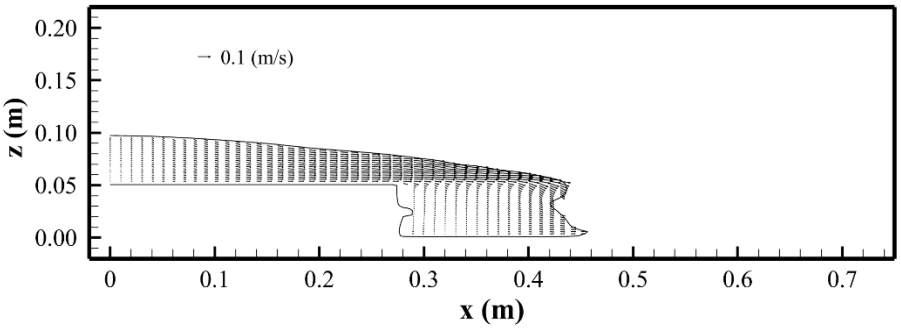

(b) t = 0.4 (s)

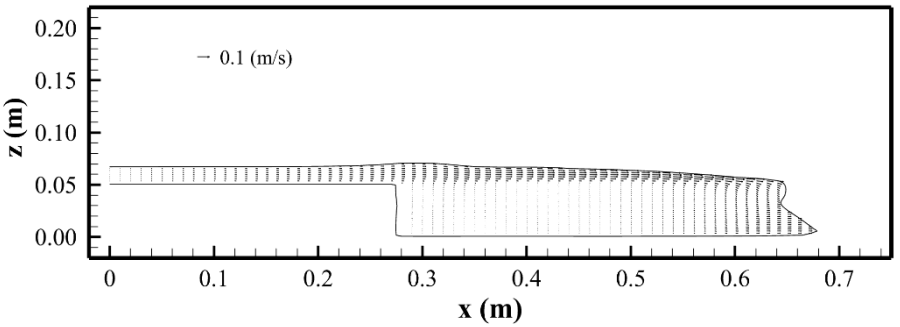

(c) t = 1 (s)

Figure 4.5 Water surface profiles and velocity vectors

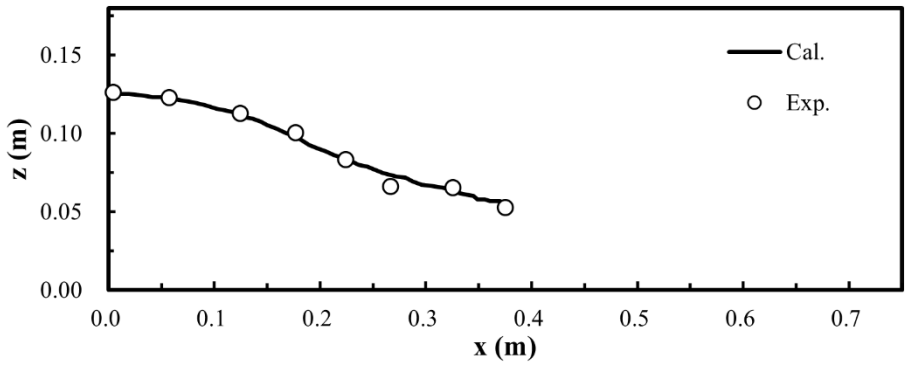

(a) t = 0.2 (s)

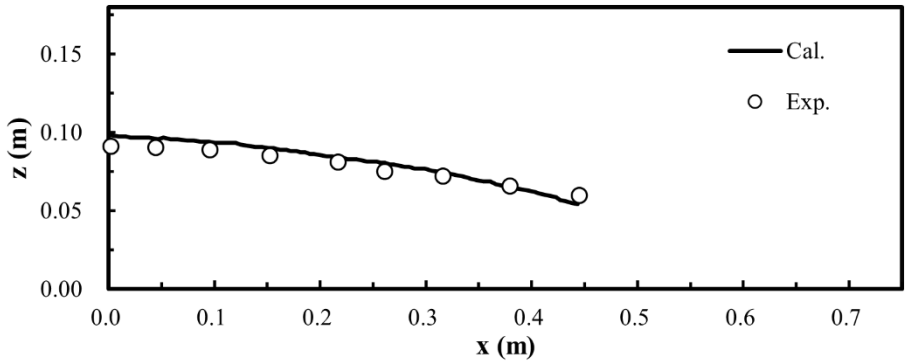

(b) t = 0.4 (s)

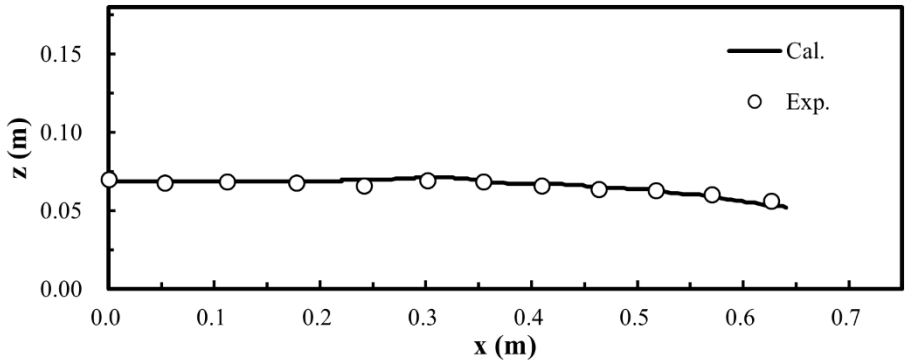

(c) t = 1 (s)

Figure 4.6 Comparisons of water surface profiles

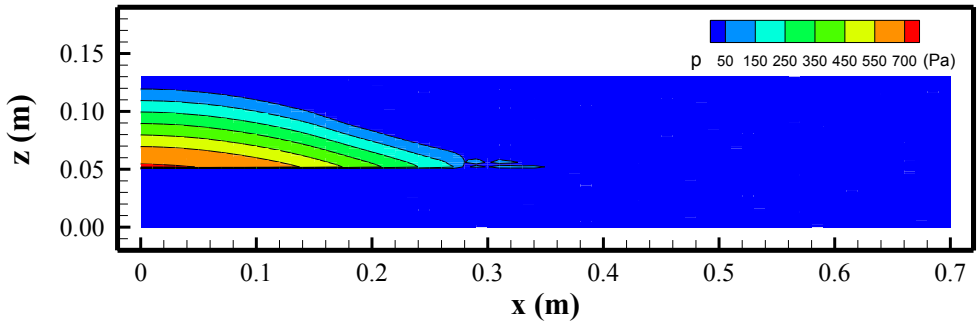

(a) t = 0.2 (s)

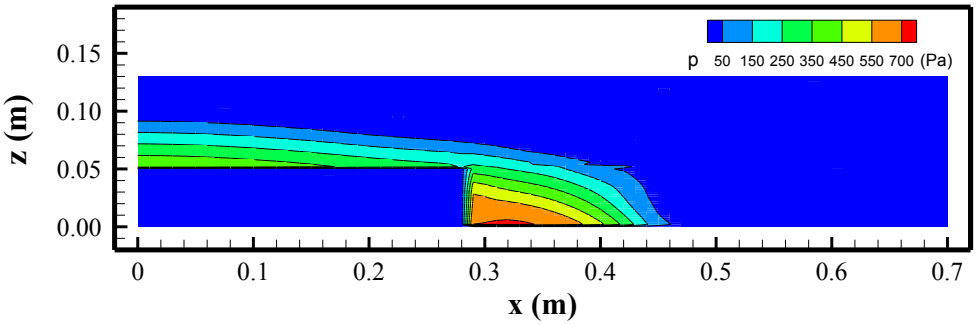

(b) t = 0.4 (s)

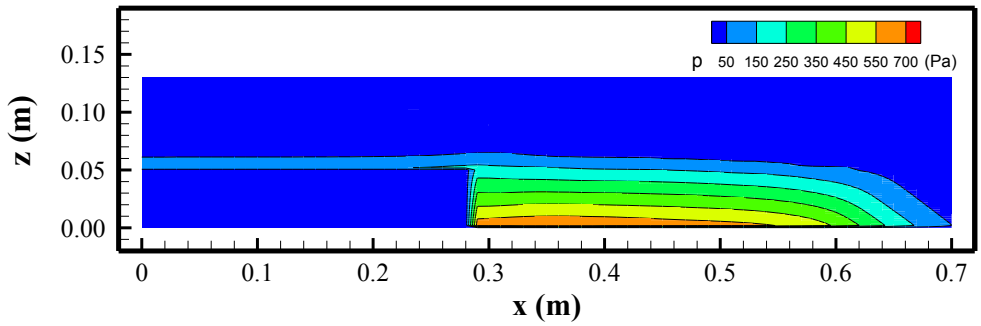

(c) t = 1 (s)

Figure 4.7 Evolution of pressure profiles during simulation

Table 4.3 Experimental conditions[5)]

h (cm)	8.7	Diameter d_{50} (cm)	0.247
U (cm/s)	21.2	B (cm)	70
Fr	0.23	w_s(cm/s)	-0.324

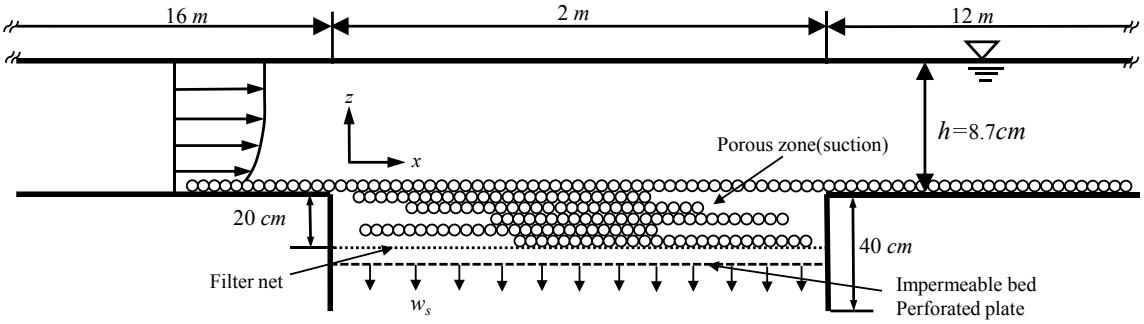

Figure 4.8 Schematic diagram of test section in experiment[5)]

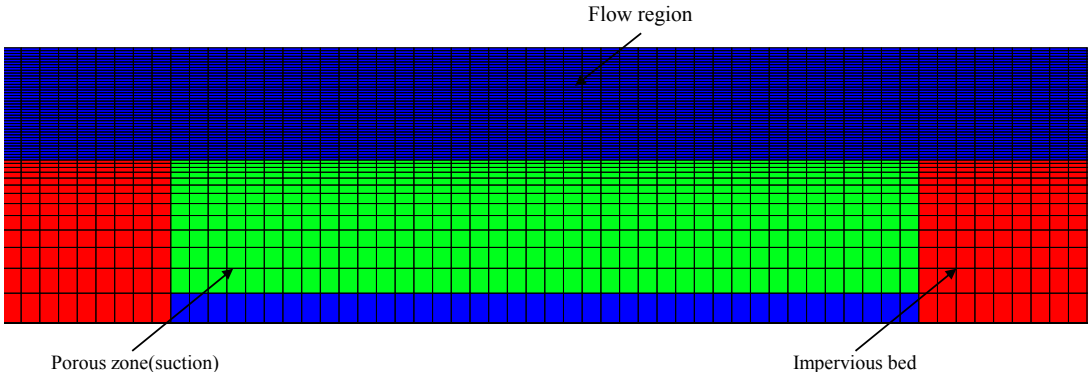

Figure 4.9 Computational mesh in the vertical plant

4.3.3 Application to open channel flows with bed suction

The numerical model is applied to simulate the experiment carried out by Chen & Chiew[5)]. The experiment investigated the velocity distribution of the open channel flows with bed suction. In this experiment and simulation, the flow patters are investgated considering the influence of seepage flow and river bed suction.

(1) Computational conditions

The schematic diagram of the experiment[5)] is shown in **Figure 4.8**. The total

length of the experimental flume is 30 (m) long. The suction zone, which is set at a distance of 16 (m) from the flow entrance of the flume, spans a length of 2 (m), a width of 70 (cm)and a depth of 40 (cm). It is filled with sand, characterized by median particle size (d_{50}) of 0.00247 (m), reaching a depth of 20 (m). The seepage flow velocity w_s in the experiment is regulated by adjusting the valves installed on the drainage pipes to ensure uniformity. Both the upstream and downstream channels were roughened using the same sand particles to achieve consistent roughness with the suction zone.

Figure 4.9 depicts the part of the computational mesh configuration around the porous zone. The rectangular computational mesh in streamwise ξ, transverse η, and vertical ζ directions consists of 150, 14, and 40 elements, and the mesh sizes in each direction are set to 5 (cm), 5 (cm), and 0.5 (cm)-2 (cm) (0.5 (cm)for surface flow region, 0.5 (m)-2 (cm)for porous zone) respectively. The porous zone with suction is represented by the green meshes and initially saturated, while the blue meshes depict the flow region. The impermeable riverbed and walls are represented by the red meshes.

The experimental conditions (Case 2) are presented in **Table 4.3**. h is water depth, d_{50} is median particle size, U is depth-averaged velocity, B is the width of the experimental flume, Fr is Froude number.

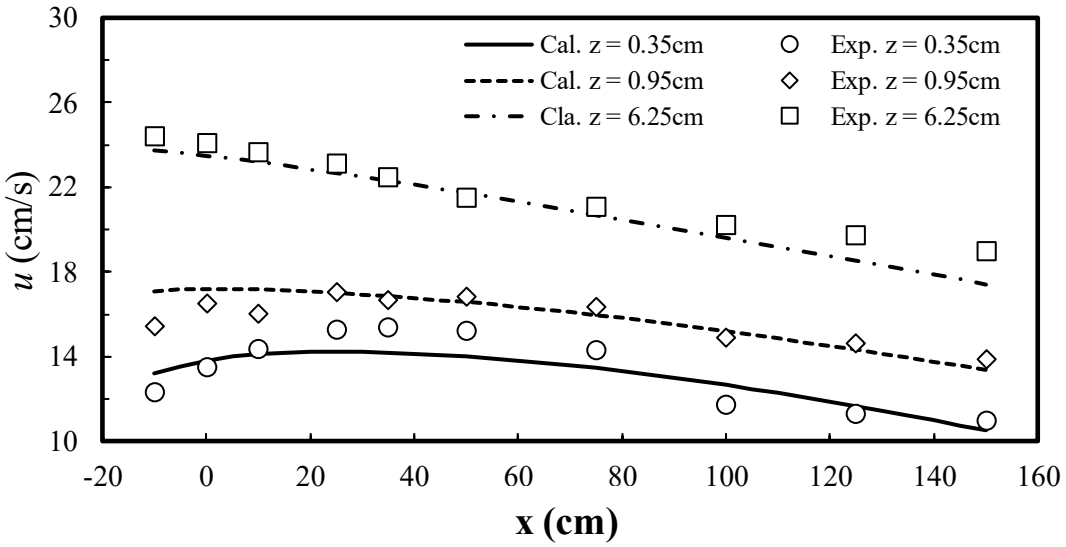

Figure 4.10 Streamwise velocity distribution at various vertical positions

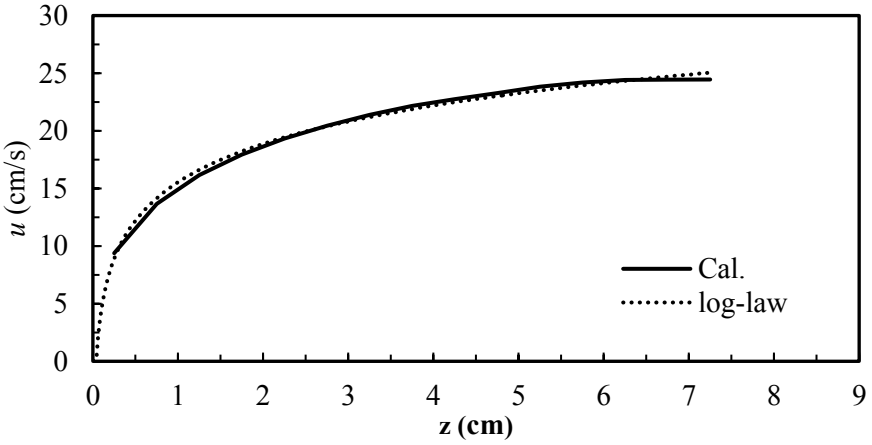

(a) **x** = -25 (cm)

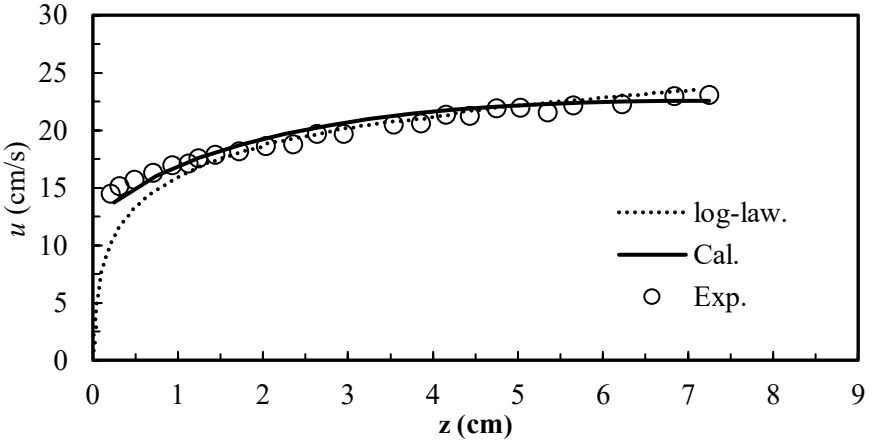

(b) **x** = 25 (cm)

Figure 4.11 Vertical velocity distributions

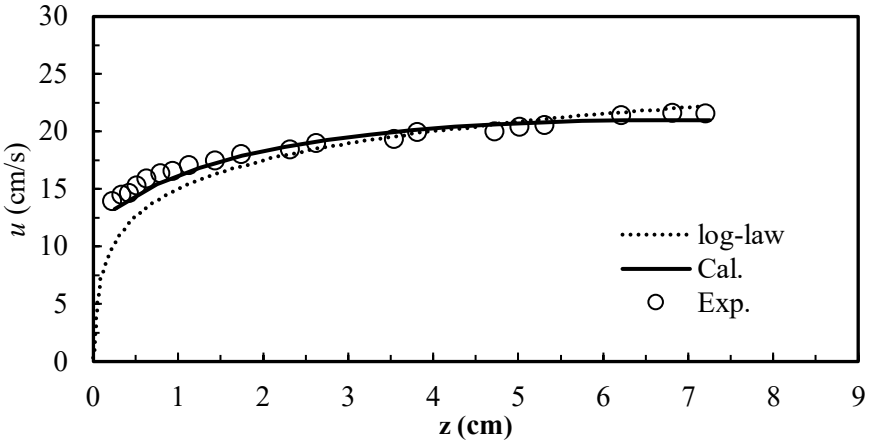

(c) **x** = 75 (cm)

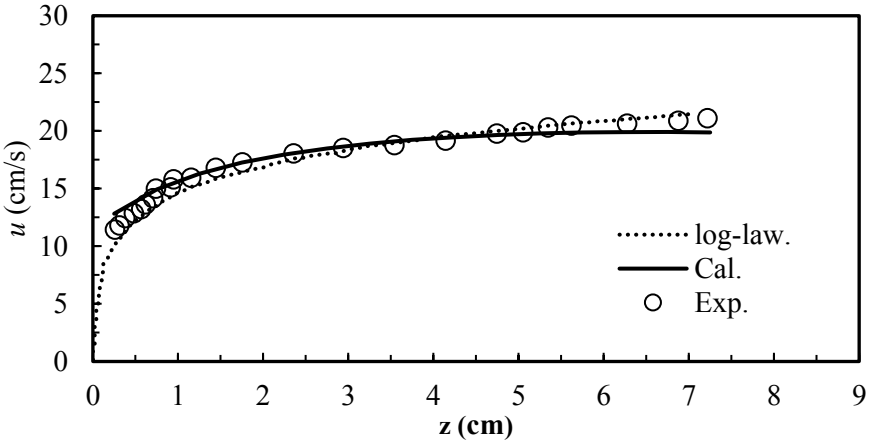

(d) **x** = 100 (cm)

Figure 4.11 Vertical velocity distributions

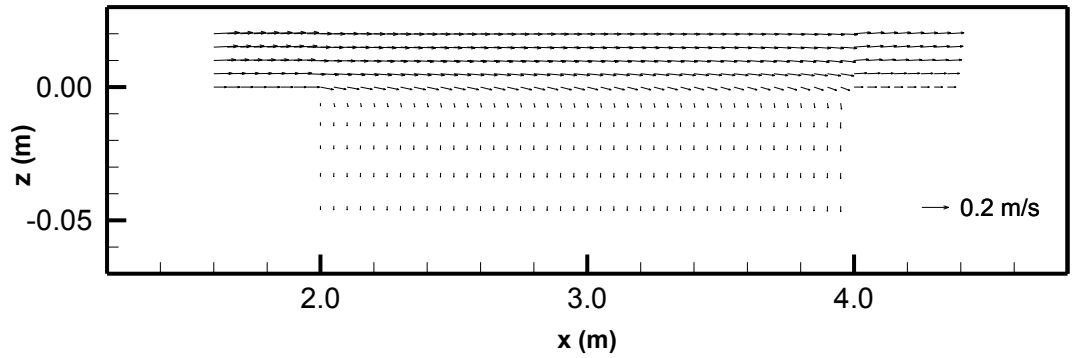

Figure 4.12 Streamwise velocity vectors near the edge of porous zone

(2) Simulation results and discussion

Figure 4.10 presents the velocity distributions at various vertical positions, providing valuable insights into the flow characteristics. The leading edge of the suction zone is set as **x** = 0 (cm) and **z** is the vertical distance from the bottom of the flume bed. The findings from **Figure 4.10** show a distinctive difference in the velocity distributions above the suction zone compared to a normal open channel flow. Near the permeable riverbed, specifically at **z** = 0.35 (cm), the flow velocity demonstrates a distinctive behavior characterized by an initial increase, followed by a subsequent decrease, and attains a peak velocity value within the **x** range of 30-45 (cm). Within the **x** range of 0-40 (cm), the presence of suction brings the downward flow to the porous zone, increasing the velocity value near the riverbed. However, since the flow rate in the main flow direction decreases due to the outflow from the bottom of the porous zone, the velocities in the *x* range exceeding 40 (cm) are deceased in terms of flow continuity. The velocity distributions at **z** = 0.95 (cm) exhibit a similar pattern to those at **z** = 0.35 (cm), which is a slightly smaller trend. On the other hand, as observed in the experiment[5)], the simulation demonstrates a decrease in velocity throughout the entire suction zone at **z** = 6.25 (cm), indicating that the influence of suction is primarily confined to the riverbed.

Figure 4.11 illustrates the vertical velocity distributions at three specific positions (**x** = -25 (cm), **x** = 25 (cm), **x** = 75 (cm), and **x** = 100 (cm)) obtained from the experiments[5)], simulations, and log-law predictions. Upon the solid bed, the velocity distribution shown in **Figure 4.11** (a) follows the log-law, while both the experimental observations and simulation results shown in **Figure 4.11** (b), (c) and (d) show that the

velocities near the riverbed under suction conditions are larger than those predicted by the log-law, and vertical velocity distribution near the riverbed are more uniformed.

Figure 4.12 presents the distribution of streamwise velocity vectors in the vicinity of the bed bottom. It can be observed from the figure that near the edge of the porous zone, the flow velocity is slightly accelerated in a downward and oblique direction due to the effect of suction. This observation is consistent with the conclusions drawn from **Figures 4.10** and **4.11**.

Hence, the presence of seepage flow exerts substantial influence on the velocity distributions near the permeable riverbed and the patterns of velocity distributions can be reproduced in this study. Therefore, incorporating the seepage process into numerical models is of great importance to enhance the model's accuracy.

Table 4.4 Experimental conditions[13)]

Bend angle (°)	90	Averaged d (mm)	0.6
Width B (m)	0.2	Flow rate Q (m^3/s)	0.004
Radius of curvature r (m)	0.2	Averaged depth h (m)	0.04
Bed slope	1/300	B/h	5.0

4.3.4 Application to the flows in a curved open channel

Subsequently, the model is employed to simulate the flows in a curved open channel over a deformed riverbed, aiming to assess the accuracy of reproducing the flow fields, including the complicated velocity of streamwise and secondary flows and water surface profile. Hinokidani et al.[13)] conducted experiments to investigate bed variations in a curved channel.

(1) Computational conditions

The experimental channel used in their study has a length of 6.84 (m) and a width of 0.2 (m), featuring a rectangular cross section. The channel bend between two straight channels in the study has a 90° curvature with a length of 0.94 (m) and a radius of 0.6 (m). The upstream straight section of the channel extends for 4.5 (m), while the downstream straight section spans 1.4 (m). Once the riverbed deformation reaches a

steady state, the riverbed is stabilized by the varnish, and subsequent measurements are performed to assess the velocity distributions and water surface profiles over a fixed bed. The experimental conditions are presented in **Table 4.4**.

Figure 4.13 illustrates the contour of the riverbed profile around the channel bend, which is used for the numerical simulation. In order to optimize computational efficiency, the upstream straight section of the channel in the simulation is set to 1.5 (m) (4.5 (m) in the experiment), while the downstream straight section spans 1.0 (m) (1.4 (m)in the experiment). As a result, the computational mesh employed in this study consists of 185, 10, and 50 grids in the streamwise, transverse, and vertical directions, respectively, with grid sizes of 2 (cm), 2 (cm), and 0.5 (cm) in the corresponding directions (ξ, η, and ζ). For the curved section of the channel, the channel bend is uniformly spaced at intervals of 1.5°.

In this study, the utilization of curvilinear coordinates allows for the generation of grids along the curved channel in the horizontal plane. However, to evaluate the model's ability of accurately simulating surface and seepage flows over the deformed riverbed, the experimental riverbed profile is replicated in the vertical direction using equation (4.4). In order to mimic the fixed riverbed condition, the infiltration process is minimized by setting a sufficiently low hydraulic conductivity ($K = 7.14\times10^{-6}$ (m/s)), and the permeable riverbed is set to be saturated initially.

Regarding the boundary conditions, a constant discharge rate of 0.004 (m^3/s) is imposed at the upstream inlet. The velocity gradients are assumed to be zero at the outlet. Additionally, the water level is maintained with a fixed height of 0.04 (m) at the downstream end.

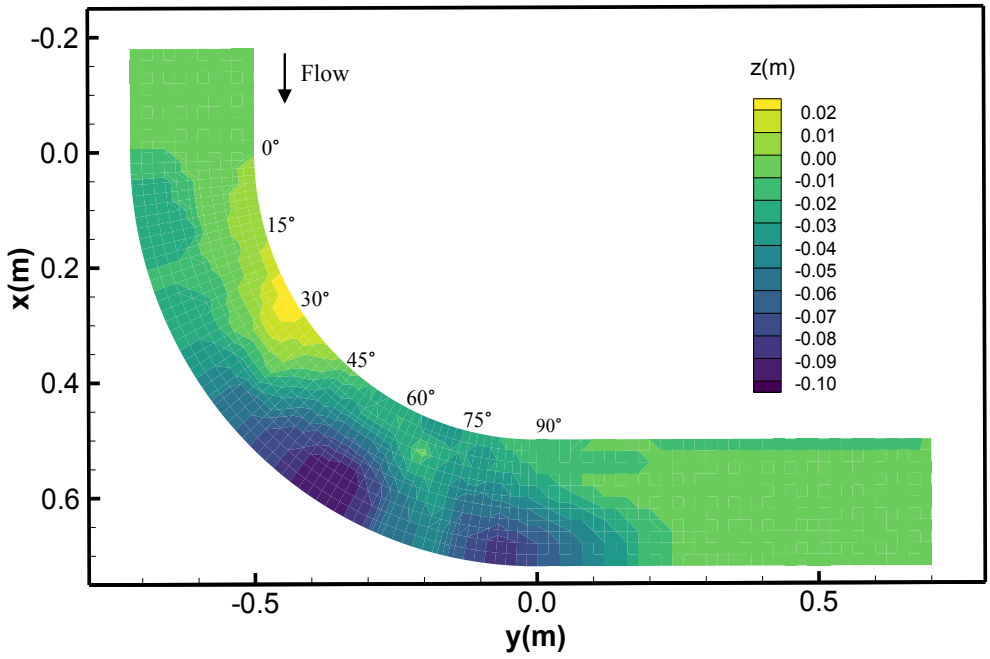

Figure 4.13 Experimental riverbed fomation[15)]

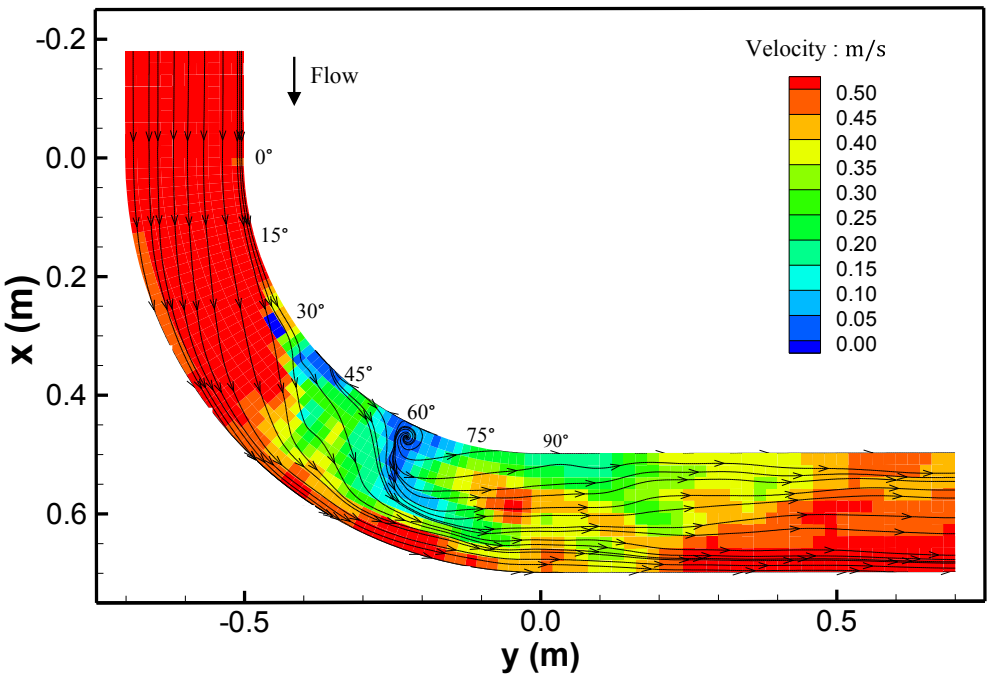

Figure 4.14 Depth averaged velocity contour and streamlines

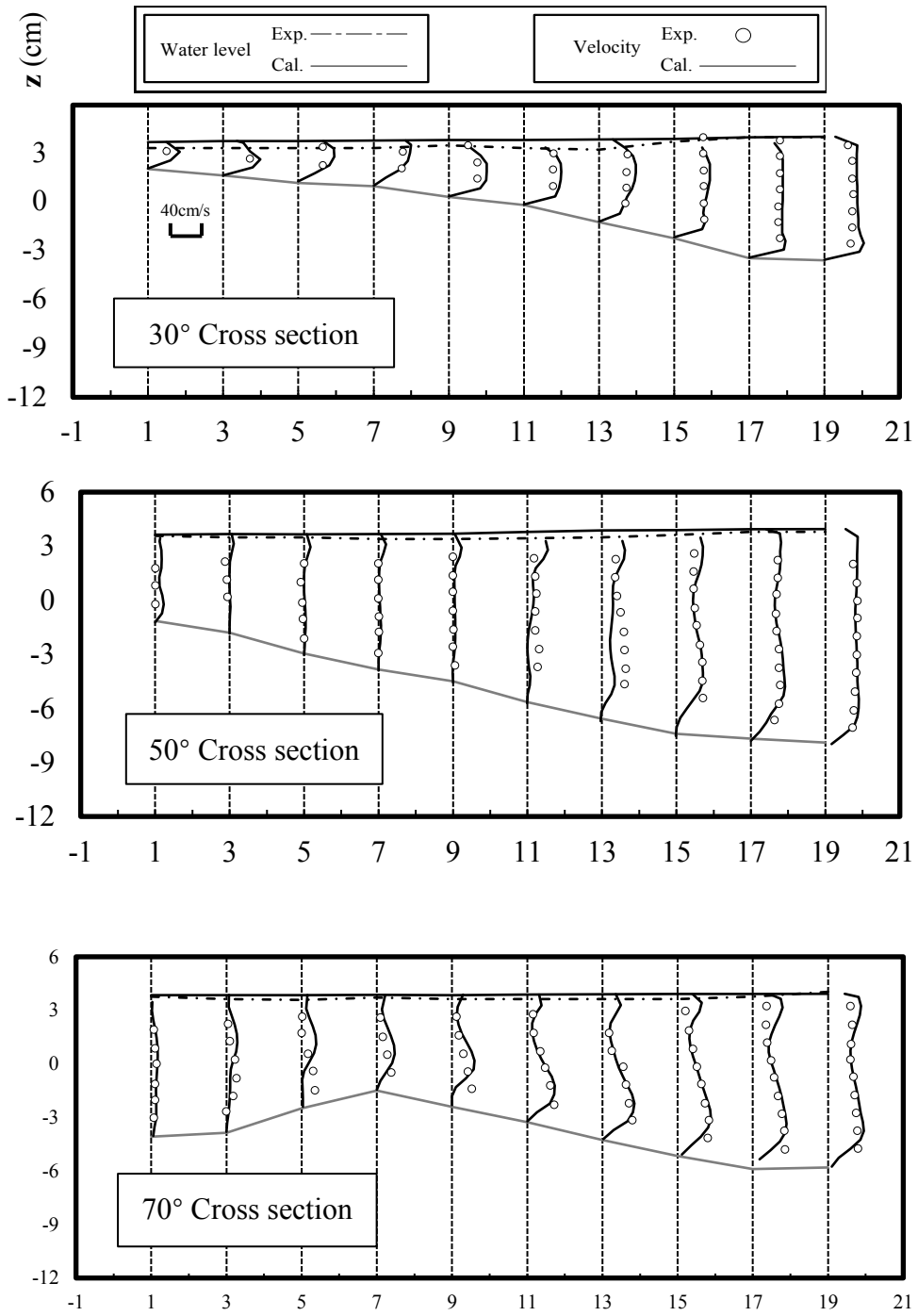

Figure 4.15 Velocity distributions in streamwise direction

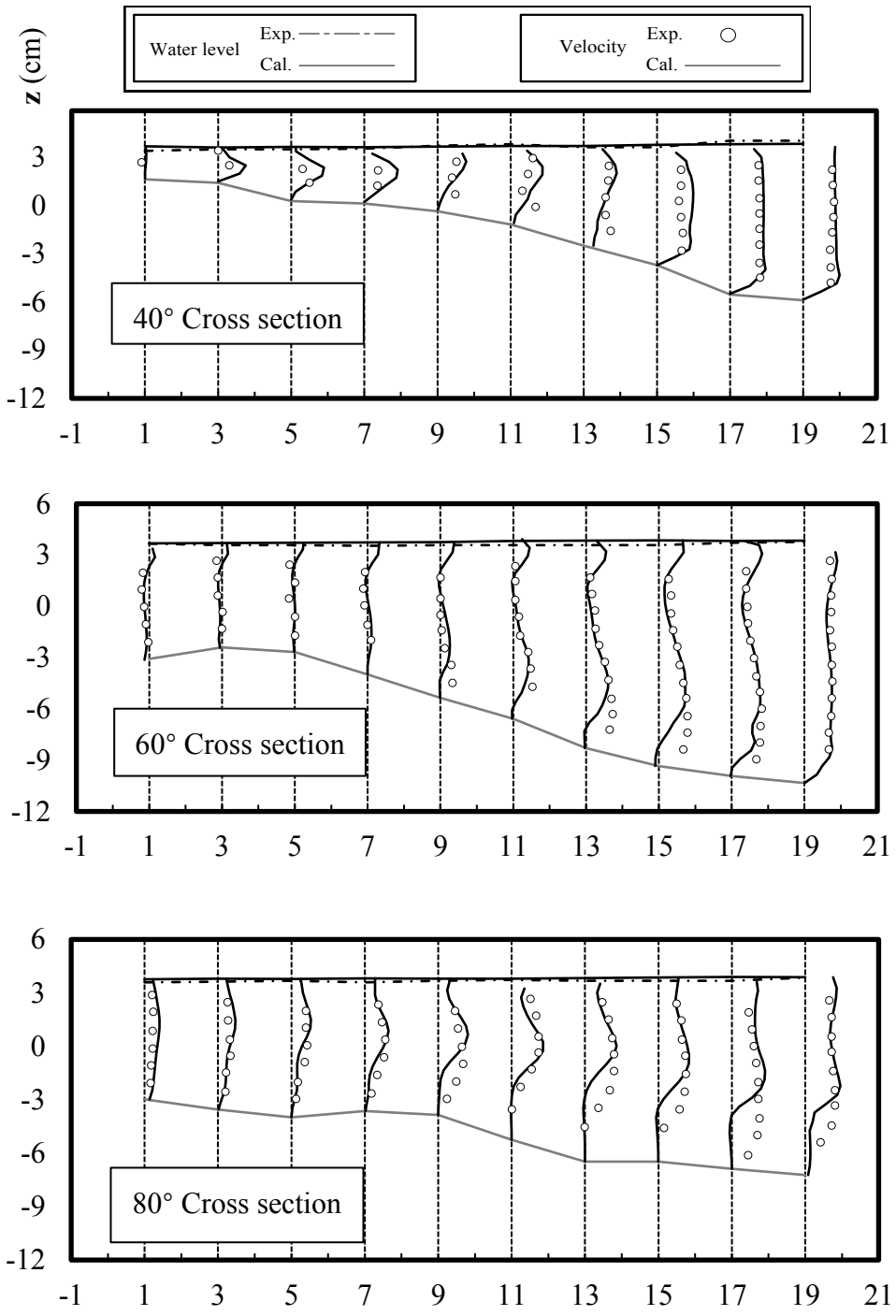

Figure 4.15 Velocity distributions in streamwise direction

(2) Simulation results and discussion

Figure 4.14 presents the contour plot of depth-averaged velocity and streamlines around the channel bend. In the experimental study[13], a separation zone is observed around the 40° section at the inner bank, with the mainstream converging towards the outer bank around the 50° to 55° section, where maximum scouring takes place. The flow diverges gradually towards the inner bank downstream of the 55° section. These flow patterns are effectively captured by the numerical model, as presented in **Figure 4.14**.

Figure 4.15 shows the comparisons of water surface profiles and vertical velocity distributions in the streamwise direction. Based on the simulation results, the overall reproduction of streamwise velocity distributions exhibits favorable agreements with the experimental observations[13]. Notably, the nearly stagnant flow patterns observed at the inner bank of the 50°, 60°, and 70° sections, where the flow separation takes place, are reproduced in the numerical simulation. However, in the 60° and 80° cross sections, the velocities at the bottom regions of 15 cm, 17 cm, and 19 cm exhibit lower magnitudes compared to the experimental measurements. One possible explanation for this discrepancy could be attributed to the relatively small scouring area observed around this section, while the computational mesh might be considered too coarse to accurately capture the velocity distribution in this scouring region.

Figure 4.16 depicts the comparisons of water surface profiles and vertical velocity distributions in the transverse direction. The same results of water surface profiles in **Figure 4.15** are shown in **Figure 4.16** to represent the water levels. According to the simulation results, analogous to the experimental observations[13] at the 30°, 40°, and 50° cross sections, fully developed secondary currents near the outer bank are confirmed in the upstream region of the scouring area around the 55° cross section. On the other hand, the agreement of velocity distributions at the 60° cross section is not deemed satisfactory. Particularly, the opposite direction of the secondary flow is observed at the bottom region of the inner bank in the 60° cross section, in contrast to the experimental findings. Moreover, the velocity magnitude at the bottom region of the outer bank surpasses that of the experimental measurements. Furthermore, in the 70° cross section, a reversed vortex is observed in the simulation at the upper region of the outer bank. One possible explanation for this difference could be the slight overestimation of secondary flows upstream, but the reason for this discrepancy is still unclear.

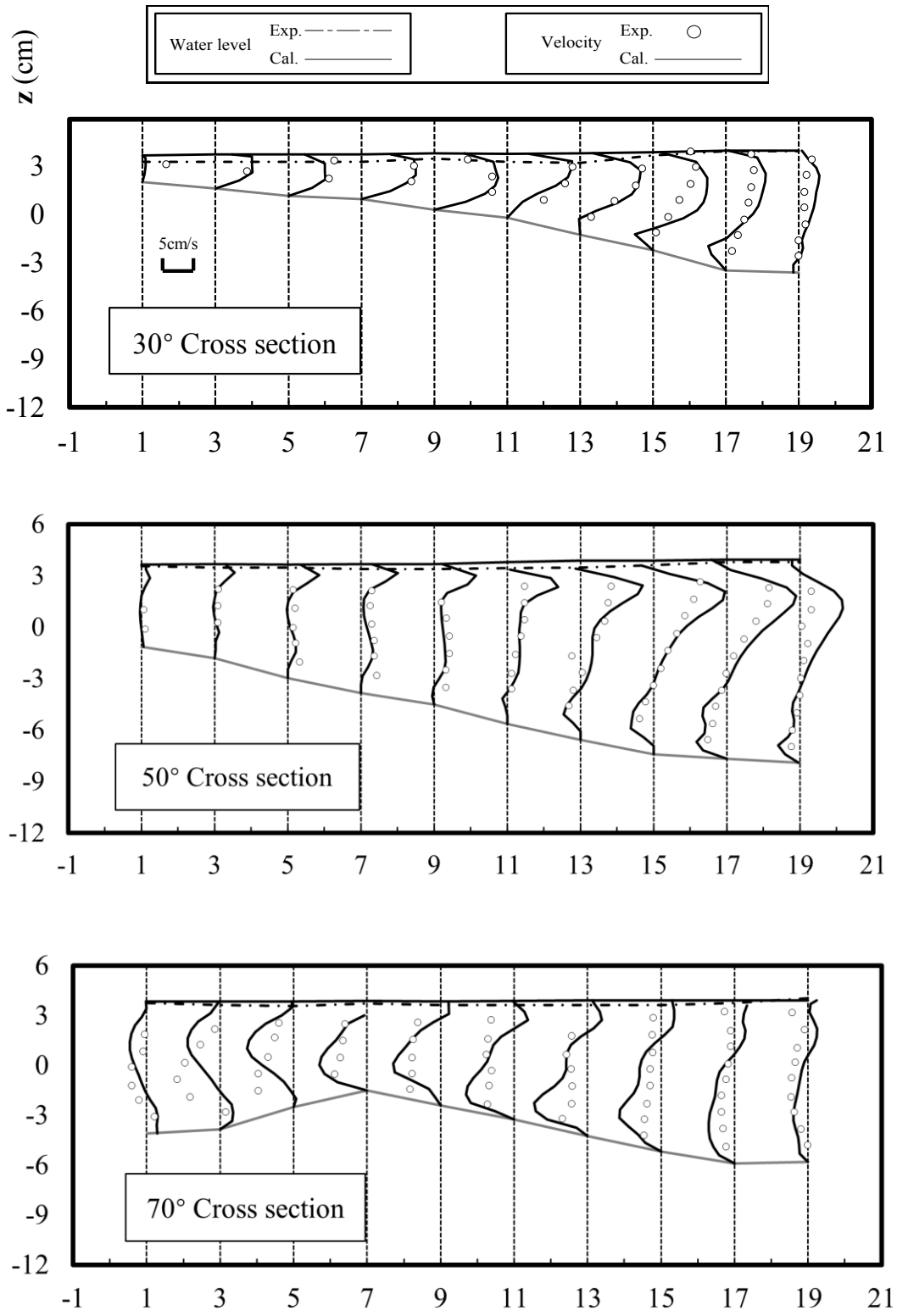

Figure 4.16 Velocity distributions in transverse direction

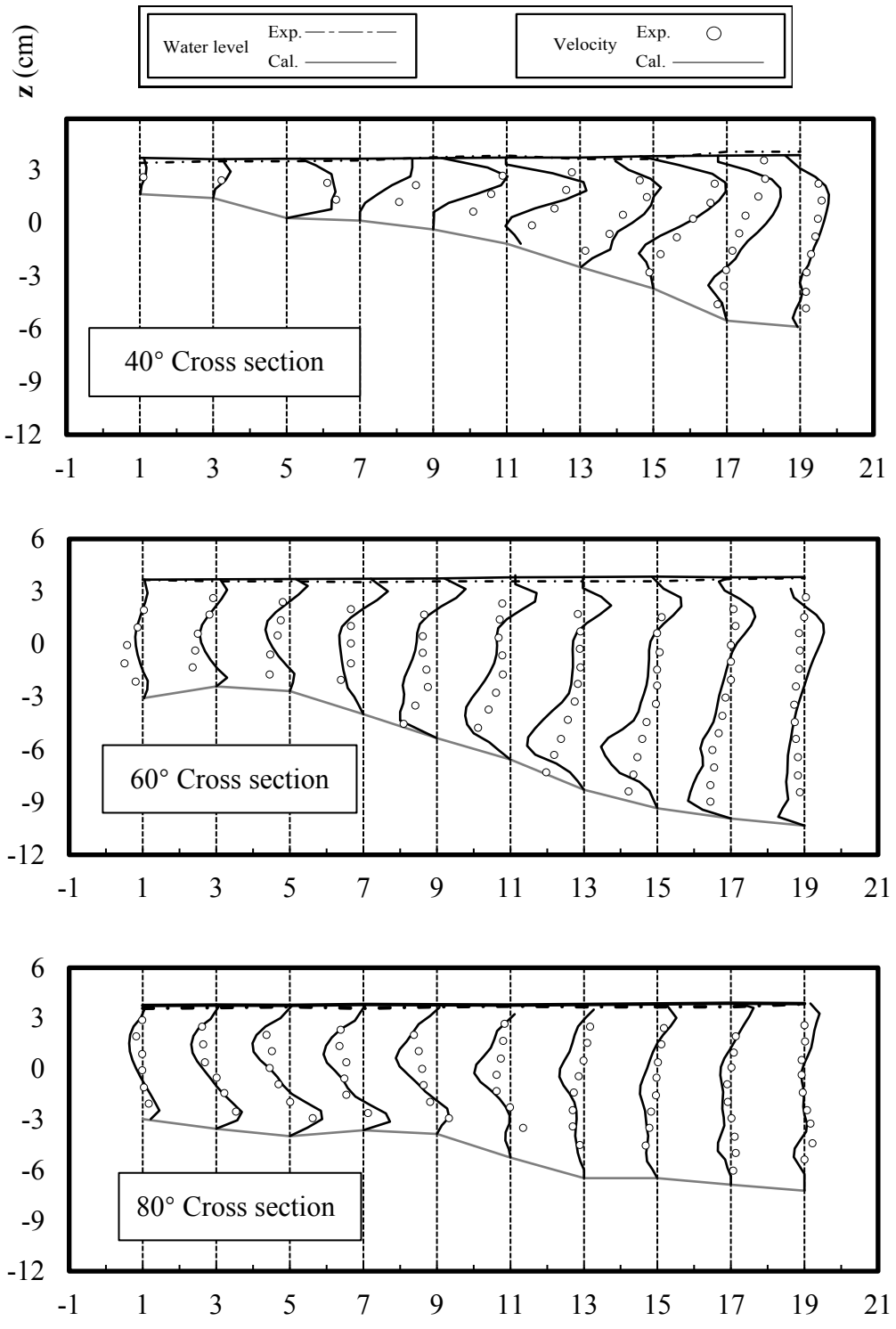

Figure 4.16 Velocity distributions in transverse direction

For the experimental study[13] of curved open channel flows, two simulations were conducted by Kajikawa et al.[14] and Shimada et al.[15]. Kajikawa et al.[14] employed the FAVOR method in their study and mentioned that the velocity distribution upstream of the 40° section exhibited significantly higher values, and the separation zone behind 40° is elongated compared to the experimental data. Due to the abrupt variations near the separation zone, the agreement between the simulated and observed water surface profiles around the 40° section is unsatisfactory. Furthermore, the reproduction of vertical velocity distributions at the inner bank of the 50° and 60° sections, as well as the vertical velocity distributions at the center of the 80° section, does not align well with the experiments.

Shimada et al.[15] conducted simulations of the experiment using a generalized curvilinear moving coordinate system and compared the vertical velocity distributions and averaged velocity vectors. Based on their findings[15], inverse vortices are observed at the outer bank near the water surface in the 50°, 60°, and 70° cross sections, therefore the reproduction of the water surface in these sections is not satisfactory. Moreover, the secondary flow even exhibits complete reversal in the 80° cross section in the simulation.

As the three numerical results illustrate, all the models can simulate reasonable flow patterns observed in the experiment. However, upon a detailed comparison, it can be observed that the simulated flow patterns in this numerical model are better than the previous models, as shown in **Figure 4.15** and **Figure 4.16**. Specifically, the water surface profile at the 40° section and the vertical distribution at the 80° section demonstrated a better agreement with the experimental observations. Additionally, the absence of inverse vortices in this simulation contributed to a satisfactory reproduction of the water surface profile, compared with the other two models.

4.4 Summary

Through comparison of the experimental observations and simulation results, the following conclusions are obtained:

(1) Seepage flow in the porous media and, surface and seepage flows over a permeable porous bed can be accurately predicted using this numerical model, as evidenced by the good agreement of the water surface profile with experimental observations.

(2) By incorporating a porous media approach and enabling simultaneous simulation of surface and seepage flows, the flow model employed in this study successfully

captures the variations in flow patterns, showing a substantial influence of seepage flows on the velocity distributions near the permeable riverbed.

(3) In a curved open channel with negligible seepage flows, the proposed flow model demonstrates the capability to provide reliable predictions of the complex flow dynamics, water surface profiles, and velocity distributions.

(4) Suction can have a significant impact on the infiltration process. Given that natural riverbeds are typically composed of fine sand grains, future studies will incorporate the influence of suction in unsaturated porous media to enhance the model's performance.

Reference

1) Schmocker, L. and Hager, W. H. : Modelling dike breaching due to overtopping, *Journal of Hydraulic Research*, IAHR, Vol. 47, No. 5, pp. 585-597, 2009.
2) Schmocker, L. and Hager, W. H. : Plane dike-breach due to overtopping: effects of sediment, dike height and discharge, *Journal of Hydraulic Research*, IAHR, Vol. 50, No. 6, pp. 576-586, 2012.
3) LaRocque, L, A., Elkholy, M., Chaudhry, M, H. and Imran, J. : Experiments on urban flooding caused by a levee breach, *Journal of Hydraulic Engineering*, ASCE, Vol. 139, No. 9, pp. 960-973, 2013.
4) Yoden T., Nakagawa H., Mizutani H., Kawaike K. and Zhang H. : Research on the mechanisms of river embankment by erosion due to overtopping flow in consideration of soil saturation, *Journal of Japan Society for Natural Disaster Science*, Vol. 33, No. 1, pp. 29-41, 2014. (in Japanese)
5) Chen, X. and Chiew, Y. : Velocity distribution of turbulent open-channel flow with bed suction, *Journal of Hydraulic Engineering*, ASCE Vol. 130, No. 2, pp. 140-148, 2004.
6) Cheng, N. and Chiew, Y. : Modified logarithmic law for velocity distribution subjected to upward seepage, *Journal of Hydraulic Engineering*, ASCE, Vol. 124, No. 12, pp. 1235-1241, 1998.
7) Rao, A. R., Subrahmanyam, V., Thayumanavan, S. and Namboodiripad, D. : Seepage effects on sand-bed channels, *Journal of Irrigation and Drainage Engineering*, ASCE, Vol. 120, No. 1, pp. 60-79, 1994.

8) Jewel, A., Fujisawa, K. and Murakami, A. : Effect of seepage flow on incident motion of sand particles in bed subjected to surface flow, *Journal of Hydrology*, Vol. 579, 124178, 2019.

9) Mizutani, H., Nakagawa, H., Yoden, T., Kawaike, K., and Zhang, H. : Numerical modelling of river embankment failure due to overtopping flow considering infiltration effects, *Journal of Hydraulic Research*, IAHR, Vol. 51, No. 6, pp. 681-695, 2013.

10) Kakinuma, T. and Shimizu, Y. : Large-scale experiment and numerical modeling of a riverine levee breach, *Journal of Hydraulic Engineering*, ASCE, Vol. 140, 04014039, pp. 1-9, 2014.

11) Nishimoto, N., Shimizu, Y. and Aoki, K. : Numerical simulation of bed variation considering the curvature of stream line in a meandering channel, *Japanese Journal of JSCE*, Vol. 456, pp. 11-20, 1992. (in Japanese)

12) Ghimire, B. : Hydraulic analysis of free-surface flows into highly permeable porous media and its applications, *doctor thesis*, *Kyoto University*, 2009.

13) Hinokidani, O., Michiue, M. and Kawai, S. : Experimental study on bed variation and sand waves in curved channel, *Annual Journal of Hydraulic Engineering,* JSCE., Vol. 42, pp. 979-984, 1998. (in Japanese)

14) Kajikawa, Y. and Hinokidani, Y. : 3-D numerical simulation of flow in curved channel with small width-to-depth ratio when dune developed, *Annual Journal of Hydraulic Engineering,* JSCE., Vol. 53, pp. 883-888, 2009. (in Japanese)

15) Shimada, R., Kimura, I. and Shimizu, Y. : Study on 3D flow structure and bed deformation in curved open channel, *Journal of Japan Society of Civil Engineers, Ser. A2 (Applied Mechanics)*, Vol. 67, No. 2, pp .703-712, 2011. (in Japanese)

Chapter 5

Model applications to bar formation and dike breaching

5.1 Preliminaries

In recent years, frequent heavy rainfalls have led to the occurrence of numerous flood events. During such floods, river discharges increase sharply, resulting in a rapid rise in water levels and flow velocities. Particularly in meandering sections of rivers, the influence of centrifugal forces causes higher water levels on the outer bank compared to the inner bank, significantly increasing the risk of levee breaches. Flows in meandering channels, particularly after overtopping events, often exhibit complex three-dimensional characteristics, including secondary flows and bed deformation. To address the knowledge gap in the process of dike breaching at a channel bend, this study aims to develop a 3D flow model with sediment transport in the curvilinear coordinate system. The model will effectively capture both the curved channel boundary and the dike surface, enabling a precise numerical investigation of the dike failure process at a channel bend. While specific experiments for direct comparisons are lacking, the model's performance is assessed through separate verifications as bed deformation in the meandering channel and levee breaching to ensure its accuracy and reliability. The final goal of this research is to contribute valuable insights into risk management and safety assessment in meandering river systems by using this kind of numerical model.

As a typical bed deformation phenomenon in meandering channels, Hasegawa[1)] and Colombini et al.[2)] conducted a series of experiments investigating the bar formation with different hydraulic conditions.

Moreover, several experimental studies investigated the process of dike breaching. Schmocker et al.[3), 4)] and LaRocque et al.[5)] conducted a comprehensive series of experiments by systematically varying the parameters of hydraulic conditions, dike

materials, and dike geometry.

For numerical study, several numerical models have been proposed to simulate the bar formation[6] as well as the dike breaching process[7), 8), 9), 10)]. Most of these models are developed by 2D shallow water equations[6), 7), 8), 9), 10)]. However, flows in a meandering channel show the three-dimensional flow structure, and the flow fields and sediment transport phenomena around the dike exhibit significant complexity. The shallow water approach has inherent limitations in accurately simulating these processes. Therefore, a 3D model is necessary. Onda et al.[11), 12)] utilized a 3D flow model incorporating both equilibrium and non-equilibrium sediment transport models to simulate the dike failure process within a Cartesian coordinate system. Kajigawa[13)] employed FAVOR method in Cartesian grids to simulate the bar formation in the meandering channel. But the Cartesian coordinate system exhibits disadvantages in fitting smoothly the boundary and simulating the flow characteristics in regions with extremely shallow water depth along the dike surface, resulting in inadequate predictions of velocities and sediment transport along the dike surface.

In this Chapter, a 3D flow model used in Chapter 4 incorporating an equilibrium sediment transport model is developed. The performance of the model is evaluated by analyzing the numerical results, including comparisons with experimental data of the bed deformation in the meandering channel[1)] and the dike breaching process[12)].

5.2 Governing equation and sediment transport model

5.2.1 Flow model

The governing equations of continuity and motion are the same as those in Chapter 4, which is shown below.

[continuity equation]

$$\frac{\partial(1-c)\rho\Phi}{\partial t}+\frac{1}{\sqrt{g}}\frac{\partial(1-c)\rho\Phi\sqrt{g}V^i}{\partial\xi^i}=0 \tag{5.1}$$

[momentum equation]

$$\frac{\partial(1-c)\rho V^i}{\partial t}+\nabla_j\left[(1-c)\rho V^iV^j\right]=(1-c)\rho G^i \tag{5.2}$$

$$-(1-c)g^{ij}\nabla_j p + 2\nabla_j(1-c)\mu S^{ij} + \nabla_j[-(1-c)\rho\overline{v^i v^j}] + R^i$$

where t: time, ξ^i: spatial coordinates of the computational space, Φ: density function, c: volume fraction in the solid phase, V^i: contravariant component of velocity vector, v^i: contravariant component of the turbulent velocity vector, p: pressure, ρ: the density of fluid, g: determinate of metric tensor, μ: viscosity coefficient of fluid, g^{ij}: contravariant components of metric tensor, S^{ij}: rate of strain tensor, G^i: contravariant component of gravity.

The drag force R^i exclusively exists within the porous region and is modeled in accordance with the Darcy's law:

$$R^i = \frac{\rho G(1-c)^2}{K} V^i \tag{5.3}$$

where K is hydraulic conductivity, and G is the magnitude of gravity.

5.2.2 Bed deformation model

The bed load transport is considered as the sediment transport in this flow model. First, the revised Mayer-Peter and Müller equation (5.4), which incorporates the influence of bed gradient shown in equation (5.5) as proposed by Colombini[14], is utilized to calculate the bed load rate q_{bs} in the streamwise direction. Additionally, equation (5.6) by Hasegawa[1] is employed to determine the bed load rate q_{bn} in the transverse direction.

$$q_{bs} = a(\tau_* - \tau_{*c})^{\frac{3}{2}} \sqrt{(\frac{\sigma}{\rho_w} - 1)Gd^3} \tag{5.4}$$

$$\tau_{*c} = \tau_{*c0} - \frac{\tau_{*c0}}{\tan\varphi}(S - \frac{\partial z_b}{\partial s}) \tag{5.5}$$

$$q_{bn} = q_{bs}\left(-\sqrt{\frac{\tau_{*c}}{\mu_s\mu_k\tau_*}}\frac{\partial z_b}{\partial n}\right) \tag{5.6}$$

where q_{bs} and q_{bn} are the bed load rate in the streamwise and the transverse directions, τ_* is the dimensionless tractive stress, τ_{*c} is the dimensionless critical tractive stress, σ is the density of bed material, ρ_w is the density of water, d is the diameter of sediment particle, τ_{*c0} is dimensionless critical tractive stress calculated by Iwagaki equation (5.7) and (5.8), φ is the friction angle, S is the bed slope, z_b is bed elevation, μ_s is

the static friction factor (=0.7), μ_k is the dynamic friction factor (=0.35).

$$\tau_{*c0} = \frac{{u_{*c}}^2}{(\frac{\sigma}{\rho_w} - 1)Gd} \tag{5.7}$$

$${u_{*c}}^2 = \begin{cases} 0.14(\frac{\sigma}{\rho_w} - 1)Gd & R_* < 2.14 \\ (0.1235(\frac{\sigma}{\rho_w} - 1)G)^{\frac{25}{32}} \nu^{\frac{7}{16}} d^{\frac{11}{32}} & 2.14 \leq R_* < 54.2 \\ 0.034(\frac{\sigma}{\rho_w} - 1)Gd & 54.2 \leq R_* < 162.7 \\ \left(0.01505(\frac{\sigma}{\rho_w} - 1)G\right)^{\frac{25}{22}} \nu^{-\frac{3}{11}} d^{\frac{31}{32}} & 162.7 \leq R_* < 671 \\ 0.05(\frac{\sigma}{\rho_w} - 1)Gd & 671 \leq R_* \end{cases} \tag{5.8}$$

where u_{*c} is critical friction velocity, ν is kinematic viscosity, R_* is Reynolds number of sand particles.

The dimensionless tractive stress τ_* is evaluated by wall function for rough surfaces (5.9).

$$\begin{gathered} \frac{V_p}{u_*} = \frac{1}{\kappa} ln \frac{z_p}{k_s} + A_r \\ k_s = 2.5d \\ \tau_* = \frac{{u_*}^2}{(\frac{\sigma}{\rho_w} - 1)Gd} \end{gathered} \tag{5.9}$$

where u_* is friction velocity, V_p is the velocity magnitude at center of the first layer of mesh above the bed and is expressed as

$$V_p = \sqrt{g_{\xi\xi}(V^\xi)^2 + g_{\eta\eta}(V^\eta)^2 + g_{\xi\eta}V^\xi V^\eta} \tag{5.10}$$

z_p is the distance between the bed surface and the center of the first layer of mesh above the bed, k_s is representative distance normal to the bed (roughness height), κ is Kármán constant (= 0.41) and A_r is a constant of 8.5.

Although the value of 8 is often used for a in equation (5.4), a = 16 was used in the dike breaching simulation for the No. 5 silica sand in consideration of the sediment transport characteristics and the erosion process when the grain size is large, which was verified in the previous numerical simulation[12].

The bed load rates, q_{bs} and q_{bn}, are firstly converted into q_b^x and q_b^y in Cartesian coordinate system, and are subsequently converted into q_b^ξ and q_b^η within the curvilinear coordinate system through coordinate transformation, showing as:

$$\begin{gathered} U_p = \sqrt{(U^x)^2 + (U^y)^2} \\ \sin\theta = \frac{U^y}{U_p}, \cos\theta = \frac{U^x}{U_p} \\ \begin{pmatrix} q_b^x \\ q_b^y \end{pmatrix} = \begin{pmatrix} \cos\theta & -\sin\theta \\ \sin\theta & \cos\theta \end{pmatrix} \begin{pmatrix} q_{bs} \\ q_{bn} \end{pmatrix} \\ \begin{pmatrix} q_b^\xi \\ \\ q_b^\eta \end{pmatrix} = \begin{pmatrix} \frac{\partial\xi}{\partial x} & \frac{\partial\xi}{\partial \mathrm{y}} \\ \frac{\partial\eta}{\partial x} & \frac{\partial\eta}{\partial \mathrm{y}} \end{pmatrix} \begin{pmatrix} q_b^x \\ \\ q_b^y \end{pmatrix} \end{gathered} \tag{5.11}$$

where U_p is the velocity magnitude of the first layer of mesh above the bed, U^x and U^y are the velocity components in Cartesian coordinate system.

The riverbed variation is then determined based on the sediment continuous equation. In Cartesian coordinate system, the sediment continuous equation is expressed by equation (5.12).

$$\frac{\partial z_b}{\partial t} + \frac{1}{1-\lambda}\left\{\frac{\partial q_b^x}{\partial x} + \frac{\partial q_b^y}{\partial y}\right\} = 0 \tag{5.12}$$

The sediment continuous equation in curvilinear coordinate system can be derived by the vector form (5.13)

$$\begin{gathered} \frac{\partial z_b}{\partial t} + \frac{1}{1-\lambda}\nabla\cdot\boldsymbol{q_b} = 0 \\ \nabla\cdot\boldsymbol{q_b} = \boldsymbol{e}^i\frac{\partial}{\partial\xi^i}\cdot\left(q_b^j\boldsymbol{e}_j\right) \\ = \boldsymbol{e}^i\frac{\partial}{\partial\xi^i}\cdot\left(q_b^j\boldsymbol{e}_j\right) \\ = \boldsymbol{e}^i\cdot\boldsymbol{e}_j\frac{\partial q_b^j}{\partial\xi^i} + \boldsymbol{e}^i\cdot q_b^j\frac{\partial\boldsymbol{e}_j}{\partial\xi^i} \\ = \delta^{ij}\frac{\partial q_b^j}{\partial\xi^i} + \frac{q_b^i}{2g}\frac{\partial g}{\partial\xi^i} \\ = \frac{1}{\sqrt{g}}\frac{\partial\sqrt{g}q_b^i}{\partial\xi^i} \end{gathered} \tag{5.13}$$

Therefore, the sediment continuous equation in curvilinear coordinate system is

shown in equation (5.14).

$$\frac{\partial \sqrt{g} z_b}{\partial t} + \frac{1}{1-\lambda}\left\{\frac{\partial}{\partial \xi}\left(\sqrt{g} q_b^{\xi}\right) + \frac{\partial}{\partial \eta}\left(\sqrt{g} q_b^{\eta}\right)\right\} = 0 \tag{5.14}$$

where λ is the porosity of bed material, q_b^{ξ} and q_b^{η} are contravariant components of bed load rates in ξ and η directions, respectively.

5.2.3 Slope collapse model

As illustrated in **Figure 5.1**, considering a scenario where the gradient between adjacent grid cells in each cross-section exceeds the angle of repose θ_c. In this case, even if there is no actual sediment transport, a slope collapse can occur, resulting in an apparent sediment flow. Now, if denoting the riverbed elevation at two adjacent points as z_{b1} and z_{b1}, and the distance between these two points as $\Delta\eta$, then

$$\begin{gathered} \frac{\partial z_b}{\partial \eta} = \frac{z_{b1} - z_{b2}}{\Delta \eta} > tan\theta_c \\ \frac{(z_{b1} - \Delta z_d) - (z_{b2} + \Delta z_d)}{\Delta \eta} = tan\theta_c \end{gathered} \tag{5.15}$$

where Δz_d represents the amount of riverbed reduction on the upper slope due to a landslide, and $\Delta\eta$ is the distance between the two points under consideration. As a result of the slope collapse, the gradient between the two points will lessen until it reaches the angle of repose θ_c.

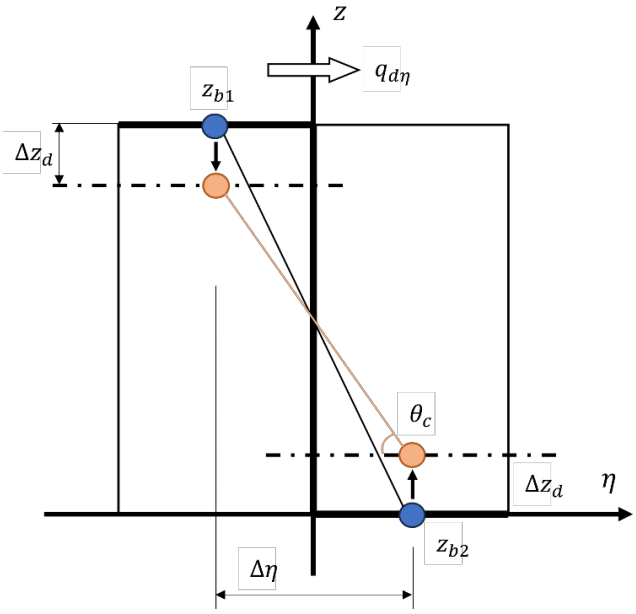

Figure 5.1 Schematic of slope collapse model

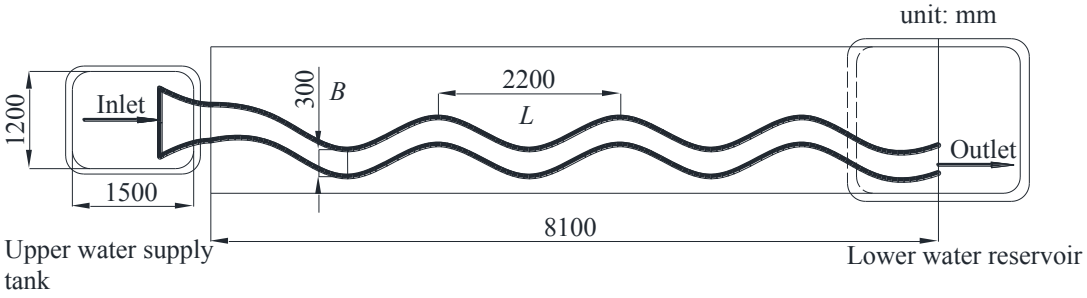

Figure 5.2 Experimental set-up[1)]

5.2.4 Numerical method

The numerical methods employed for the discretization of the continuity and motion equations are detailed in Chapter 2. For equation (5.14), the 2nd order Adams-Bashforth method is used for time integration, while the central difference method is adopted for the spatial difference of q_b^{ξ} and q_b^{η}.

5.3 Model applications

5.3.1 Application to bar formation in a meandering channel

(1) Experimental and computational conditions

The numerical model for the flows and bed deformation is applied to simulate the experiment carried out by Hasegawa[1)]. The objective of this experiment is to clarify the characteristics of the riverbed deformation comprising the bars and scour patterns induced by channel curvature. **Figure 5.2** illustrats the experimental set-up[1)]. The experimental conditions (ME-2) utilized in this study are presented in **Table 5.1**. The planform of the experimental channel exhibits a meandering shape, with its centerline represented by a sine-generated curve.

Table 5.1 Experimental flow conditions[1)]

Bed material	silica sand	Diameter d (mm)	0.425
Width B (m)	0.3	Flow rate Q (m^3/s)	0.00187
Slope i	1/300	Manning roughness n	0.018
Meandering angle (°)	30	Meandering length L (m)	2.2

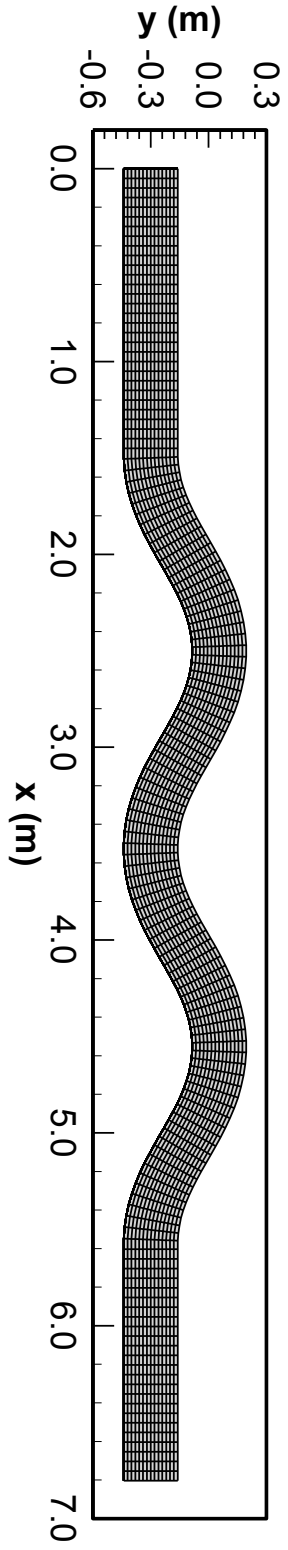

Figure 5.3 Computaional mesh in the horizontal plant

In the experimental setup, water flow was initiated on a flattened bed, and once the bed shape achieved a steady state, the experiment was temporarily stopped to immobilize the riverbed surface using a fixative. Subsequently, the experiment was resumed to measure the flow velocity.

The hydraulic condition set in the model is the same with the experiment. The computational mesh in streamwise ξ, transversal η, and vertical ζ directions consists of 150, 15, and 40 elements, with $\Delta\xi$, $\Delta\eta$ and $\Delta\zeta$ set to 5 (cm), 2 (cm), and 0.5 (cm). Time step Δt is 0.0001 (s). It is considered that the flow velocity at the entrance of the curved section and the boundary conditions at the upstream and downstream ends have a significant impact on the flow and riverbed deformation. As shown in **Figure 5.3**, simulations are therefore conducted on a computational domain that includes an additional half-meandering wavelength in both the upstream and downstream sections, up to two wavelengths. Additionally, to ensure a stable boundary condition, a straight channel of 1.5 (m) length is introduced at the inlet and outlet of the domain.

(2) Simulation results

Figure 5.4 (a) and **Figure 5.4** (b) illustrate the experimental and predicted riverbed deformation at the equilibrium state, respectively. Consistent with the experimental setup, one wavelength, characterized by well-developed riverbed deformation, was chosen for detailed analysis and discussion. The experimental riverbed reached an equilibrium state approximately 240 minutes after the initiation, whereas the computational model achieved equilibrium within approximately 60-70 minutes from the start. This may result from the different initial velocity conditions and a shorter flume compared with the experiment, which was reported by Kajikawa[13]. Since the velocity field is already well-established at the initiation of the riverbed deformation in the simulation, the time required to attain an equilibrium riverbed was likely reduced.

According to **Figure 5.4**(b), erosions are observed within the **x** = 2.6 (m) to **x** = 3.4 (m) range upstream and within the **x** = 3.3 (m) to **x** = 4.5 (m) range downstream. Additionally, the bars are observed within the **x** = 2.6 (m) to **x** = 3.4 (m) range upstream and within the **x** = 3.8 (m) to **x** = 4.4 (m) range downstream. Comparisons with experimental results reveal that the regions where erosion occurs are almost identical, and the depths of erosion are also comparable. Regarding sediment deposition, both the

experimental and simulation results indicate that the accumulation (bar) zones are primarily located on the inner bank downstream within the channel. Although the maximum deposition heights are around 0.02 (m) in both cases, there are differences in the exact locations. In the experiments, the 0.02 (m) deposition (bar) zones occur between **x** = 2.5 (m) to **x** = 2.7 (m), and between **x** = 3.6 (m) to **x** = 4.2 (m).

Figure 5.5 (a) and **Figure 5.5** (b) illustrate the experimental and predicted depth-averaged velocity vectors at the equilibrium state, respectively. Due to the presence of bars, the flow velocity is markedly slow on the inner bank of the channel and significantly faster on the outer bank. This distribution of flow velocity intensifies the concavity of the river's concave banks and the convexity of its convex banks, epitomizing a typical morphological characteristic of meandering river bends.

Figure 5.6 and **Figure 5.7** depict the temporal evolution of topography and flow velocity distribution. It is evident that due to the influence of meandering, the water flow consistently tends to erode the outer banks. Concurrently, under the effect of centrifugal force, secondary flows are generated, leading to the gradual erosion of the outer banks and the deposition of sediment on the inner banks.

Figure 5.8 illustrates the velocity vector distribution and topographical changes at three cross-sectional planes, with the green areas representing the terrain. Section 1 is located at **x** = 3.0 (m), Section 2 at **x** = 3.5 (m), and Section 3 at **x** = 4.0 (m). In Section 1, a strong secondary flow is observed on the outer bank upstream, which, under its influence, transports sediment from the outer to the inner bank, resulting in pronounced erosion on the outer bank and sediment accumulation on the inner bank. The velocity vector distribution in Section 3 is similar to that in Section 1, with both sections exhibiting areas of erosion and accumulation due to the effects of secondary flow. This flow pattern is characteristic of meandering channels.

Kajikawa utilized the FAVOR method[13)] with a Cartesian grid to simulate the same experiment. They simulated smooth, curved wall using the FAVOR method and employed a two-dimensional sediment transport flow model. While their results roughly matched the experimental measurements in terms of the amount of bed change, the locations of bars and erosion differed. Their predictions for bar and erosion locations were generally shifted downstream. For instance, there should be an erosion area of about 1 cm in the central part of the outer bank, which their model failed to replicate. This was largely

due to their numerical model didn't simulate the reduced flow velocities in the eroded outer bank regions well. However, in this model, as can be seen from **Figure 5.7**, the low-velocity regions gradually emerge as the deposition areas develop.

Thanks to the accurate prediction of secondary flows in bends by the three-dimensional flow model, the river morphology and flow characteristics predicted by this model align more closely with experimental observations compared to the FAVOR method-based numerical model.

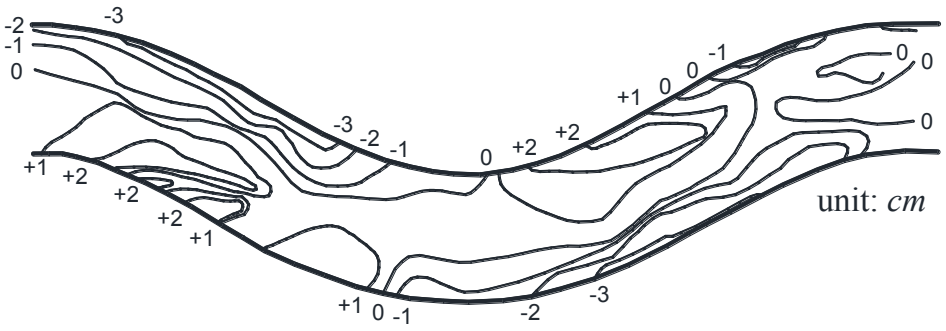

(a)

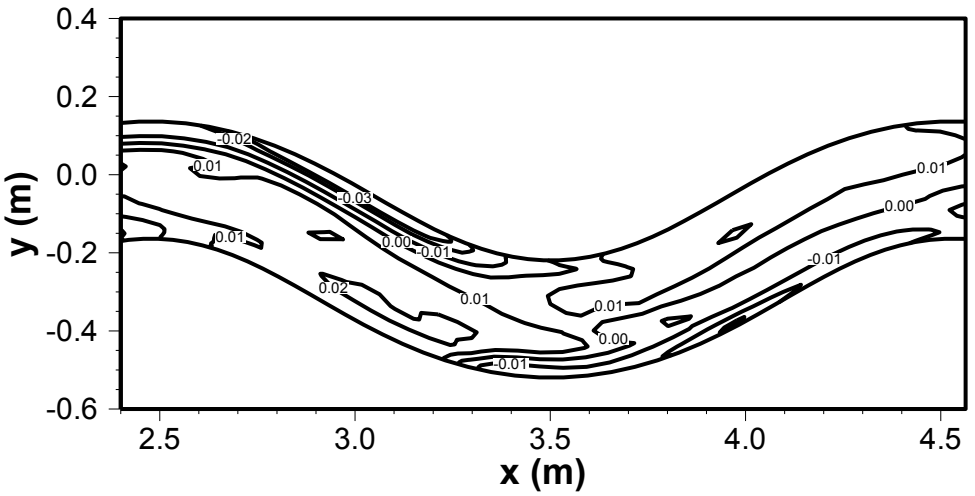

(b)

Figure 5.4 Result of the riverbed deformation
((a) Experiment and (b) Simulation)

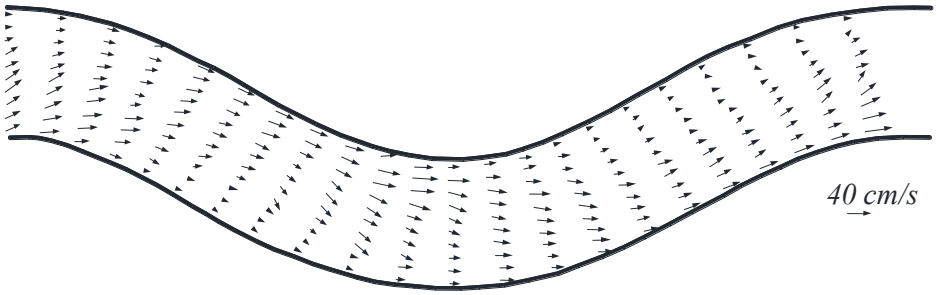

(a)

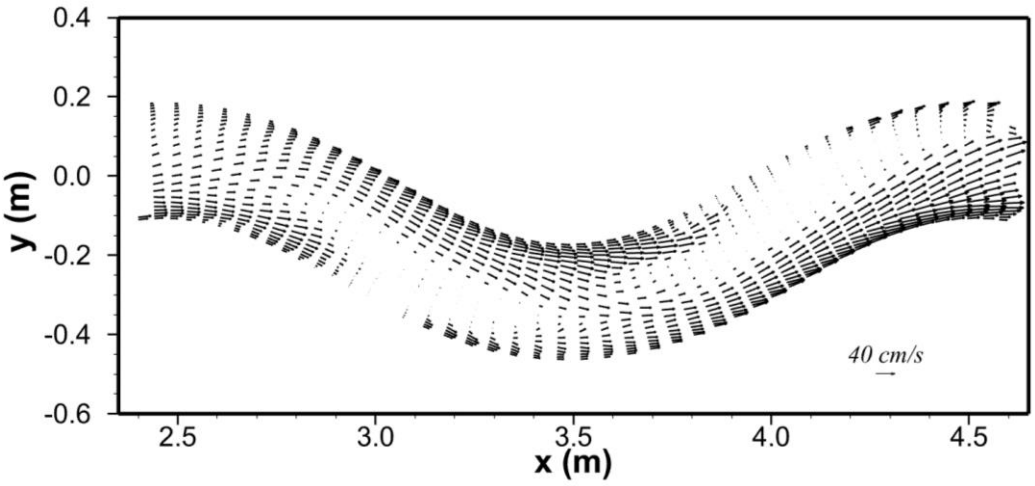

(b)

Figure 5.5 Result of depth-averaged velocity vectors
((a) Experiment and (b) Simulation)

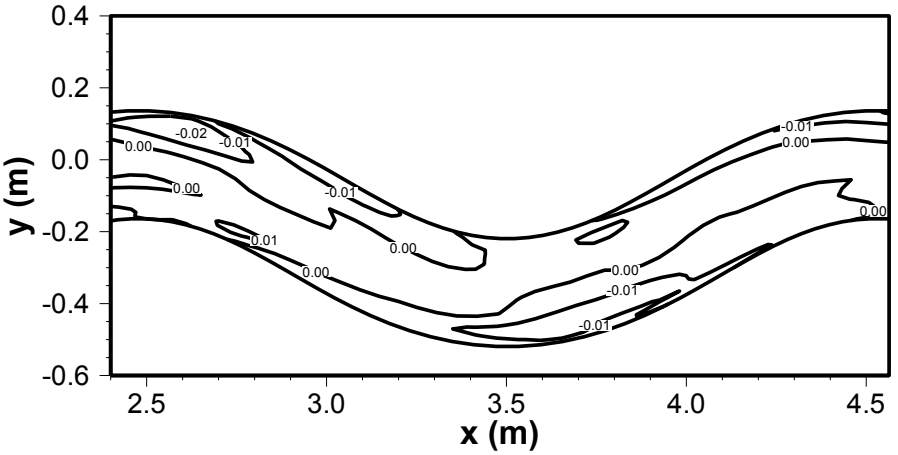

(a)

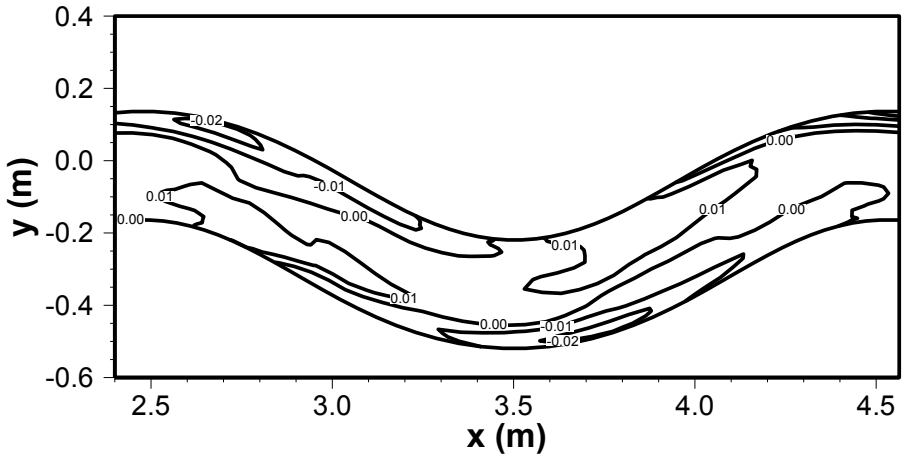

(b)

Figure 5.6 Result of temporal riverbed deformation
((a) 10 min, (b) 20 min (c) 30 min and (d) 50 min)

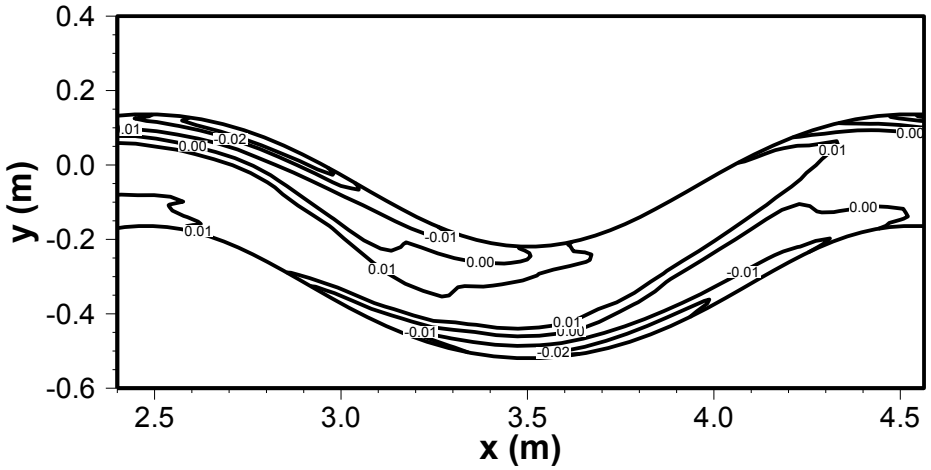

(c)

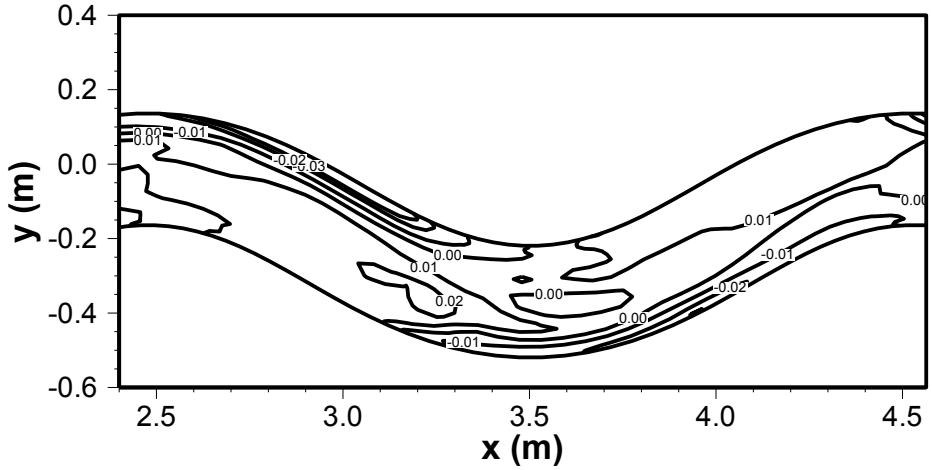

(d)

Figure 5.6 Result of temporal riverbed deformation
((a) 10 min, (b) 20 min (c) 30 min and (d) 50 min)

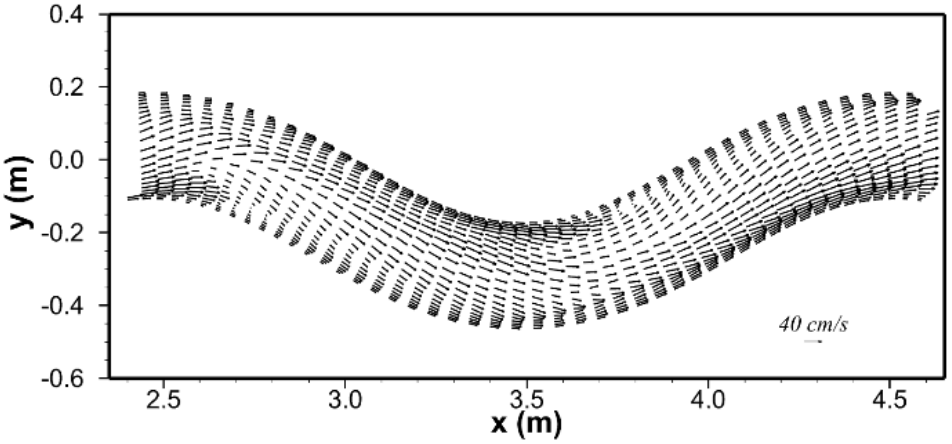

(a)

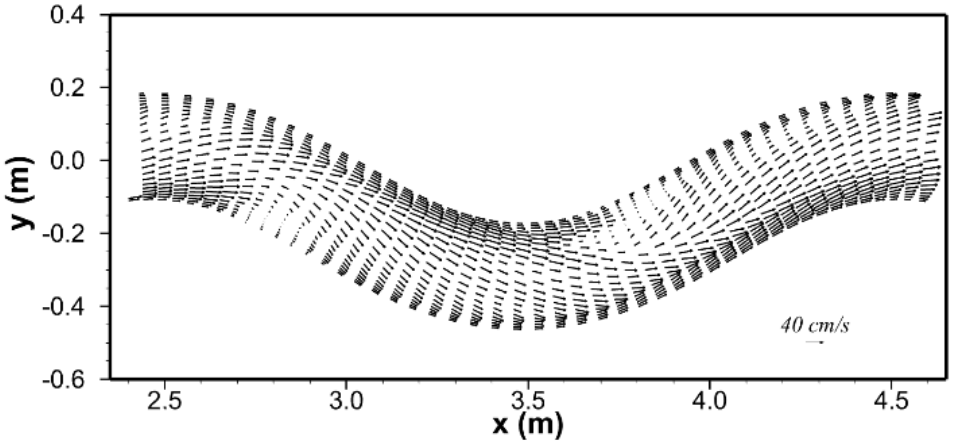

(b)

Figure 5.7 Result of temporal depth-averaged velocity vectors
((a) 10 min, (b) 20 min (c) 30 min and (d) 50 min)

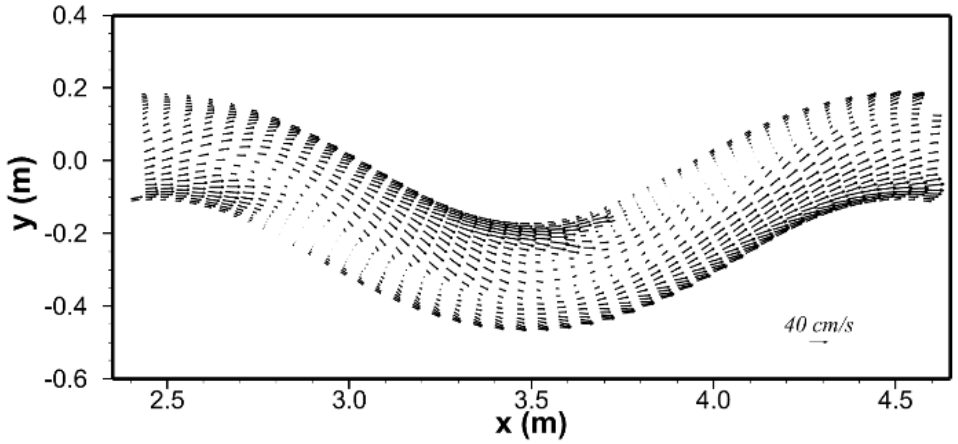

(c)

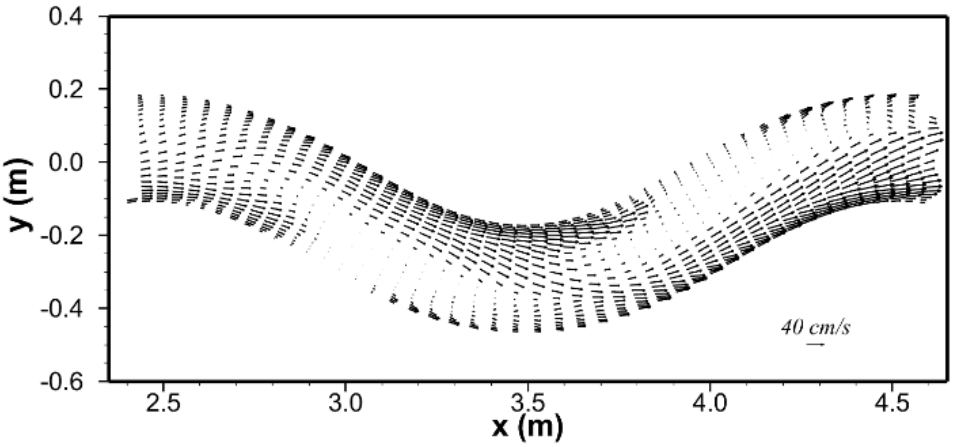

(d)

Figure 5.7 Result of temporal depth-averaged velocity vectors
((a) 10 min, (b) 20 min (c) 30 min and (d) 50min)

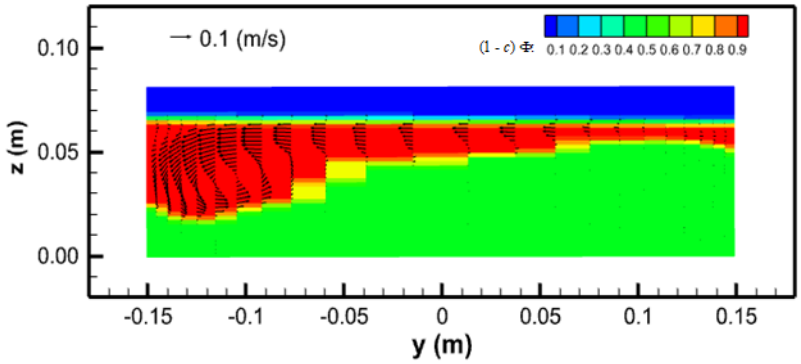

(a) Section 1

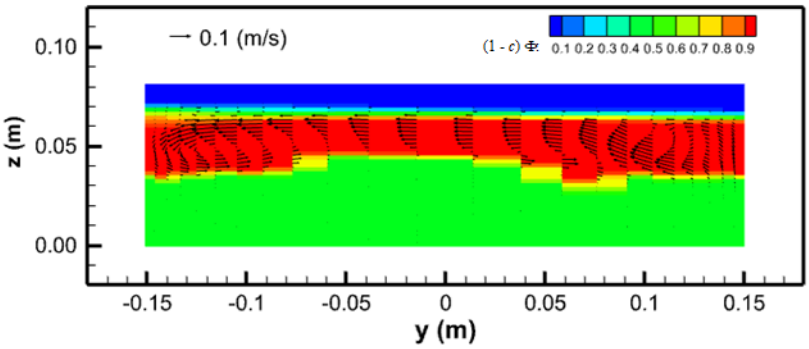

(b) Section 2

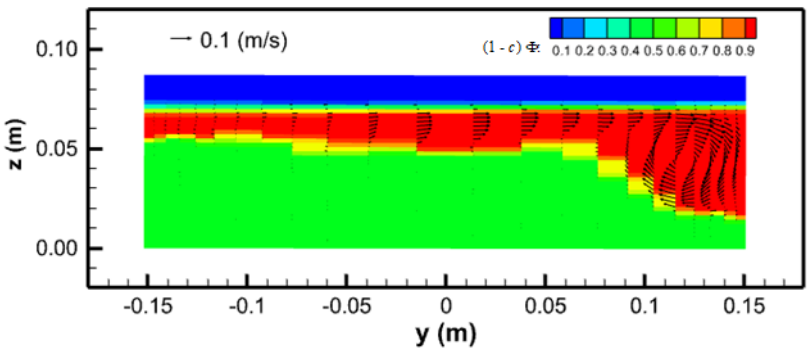

(c) Section 3

Figure 5.8 Vertical vector distributions and riverbed variations

Table 5.2 Experimental flow conditions[12)]

Bed material	No.5 silica sand	Diameter d (mm)	0.55
Width B (m)	0.2	Flow rate Q (m^3/s)	0.0033
Density of the dike body (g/cm^3)	1.52	Water saturation (%)	5.56

5.3.2 Application to dike breaching due to overtopping flows

(1) Experimental and computational conditions

The numerical model for flows and bed deformation is applied to simulate the experiment carried out by Onda et al.[12)]. The detailed schematic diagram of the experimental dike is presented in **Figure 5.9**. The hydraulic conditions of the experiment are provided in **Table 5.2.**

The computational mesh in streamwise ξ, transversal η, and vertical ζ directions consist of 390, 5, and 60 elements, with $\Delta\xi$, $\Delta\eta$ and $\Delta\zeta$ set to 1 (cm), 4 (cm), and 0.25 (cm)-2 (cm). Time step Δt is 0.00025 (s). **Figure 5.10** illustrates the schematic of the mesh around the dike body. Consistent with the experimental setup, the water is excluded in the flume initially, and the flow are simulated under a constant discharge condition from the upstream section. The initiation of overtopping flow is assumed to be at t = 0 (s), which is the same as the experiment condition.

(2) Simulation results

Figure 5.11 shows the temporal change of the flow pattern in the simulation when t = 5 (s), t = 10 (s), t = 15 (s) and t = 20 (s). The contour in **Figure 5.11** illustrates the density function Φ multiplied with the water volume fraction $(1-c)$ to observe the dike surface clearly. According to **Figure 5.11**, the seepage surface gradually propagated towards the back slope of the dike as time progressed, and the infiltration process was found to be aligned with the positions observed in the experimental results[12)], although the corresponding figure[12)] is not included in this study. Furthermore, as the erosion progresses, there is an observed increase in the overflow depth on the crest of the dike.

Figure 5.12 (a) illustrates the temporal variation of bed deformation, and **Figure**

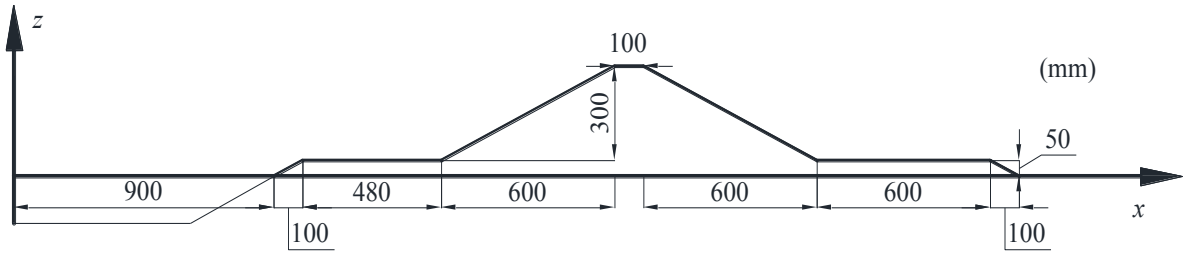

Figure 5.9 Experimental set-up[12)]

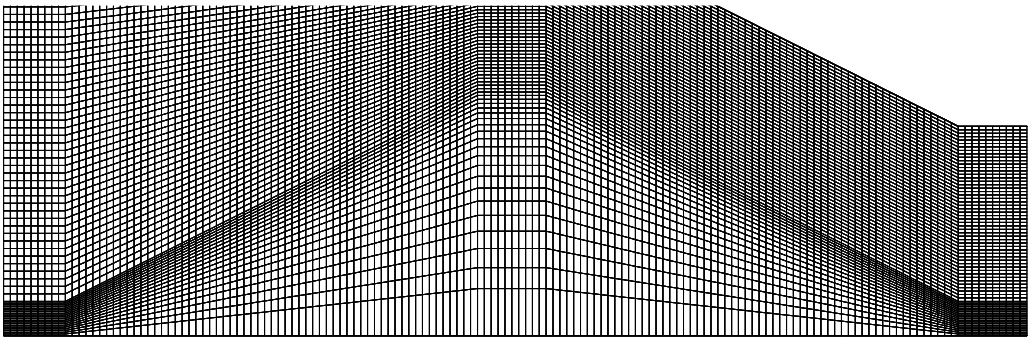

Figure 5.10 Computaional mesh for the dike body in the vertical plant

5.12(b), (c), and (d) show the comparisons between experimental observations[12)] and simulation results[12)] using Cartesian coordinates. In the Cartesian model[12)], both bed load and suspended load were considered. However, it was observed that the simulation results of the model considering solely the bed load closely resembled those of the model incorporating both bed load and suspended load, except for the area near the dike's berm. Consequently, the data from the Cartesian model[12)], which considered both bed load and suspended load, has been utilized in this analysis. The mesh size[12)] in x, y, and z directions in Cartesian coordinate system consists of 390, 5, and 71 elements, with Δx, Δy, and Δz set to 1 (cm), 4 (cm), and 1 (cm), and the number of grids[12)] in streamwise and transversal directions is the same with the curvilinear model, but the curvilinear model has a higher resolution with fewer grids (60 elements) in the vertical direction. According to **Figure 5.12** (a), the erosion process exhibits a gradual acceleration followed by deceleration, indicating a temporal variation in bed load rate. During the initial stage, characterized by a low overflow rate, the erosion process proceeds slowly. However, as the overflow rate increases, there is a pronounced increase in flow velocity. This sudden change in flow velocity triggers a significant acceleration of the erosion process. As the erosion of the dike progresses, leading to a decrease in dike height, an increase in overflow depth and a

decrease in flow velocity, the erosion process shows a gradual deceleration.

According to **Figure 5.12** (b), (c), (d)**,** the sediment transport at the back slope by the curvilinear model is found to be overestimated at t = 10 (s) and t = 15 (s). In contrast, the Cartesian model consistently underestimates the sediment transport throughout the entire duration. Furthermore, the dike heights obtained from the experiment[12)], Cartesian model[12)], and curvilinear model after 20 (s) are 0.280 (m), 0.311 (m), and 0.279 (m), respectively. Notably, the curvilinear model's dike height prediction demonstrates a closer agreement with the experimental results than the Cartesian model. One possible explanation for this result is that the mesh used in the curvilinear model offers an improved resolution of flow velocities near the dike surface, where the water depth is very shallow, particularly during the initial moments of the overtopping flow. While both the Cartesian model and the curvilinear model can simulate the observed trend of the dike erosion, the curvilinear model exhibits better accuracy in predicting the dike height.

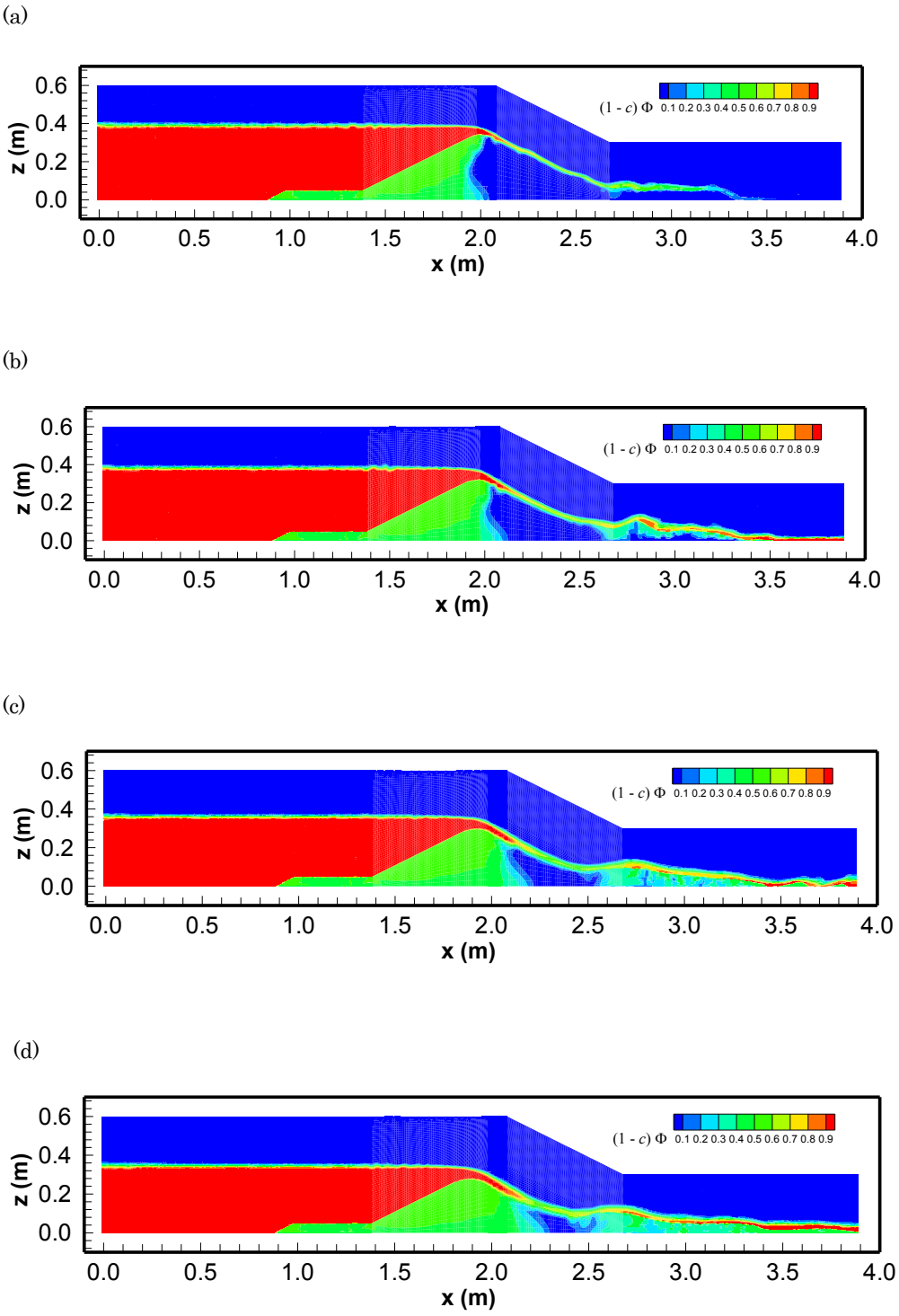

Figure 5.11 Simualtion results ((a)t = 5s, (b) t = 10s, (c)t = 15s and (d) t = 20s)

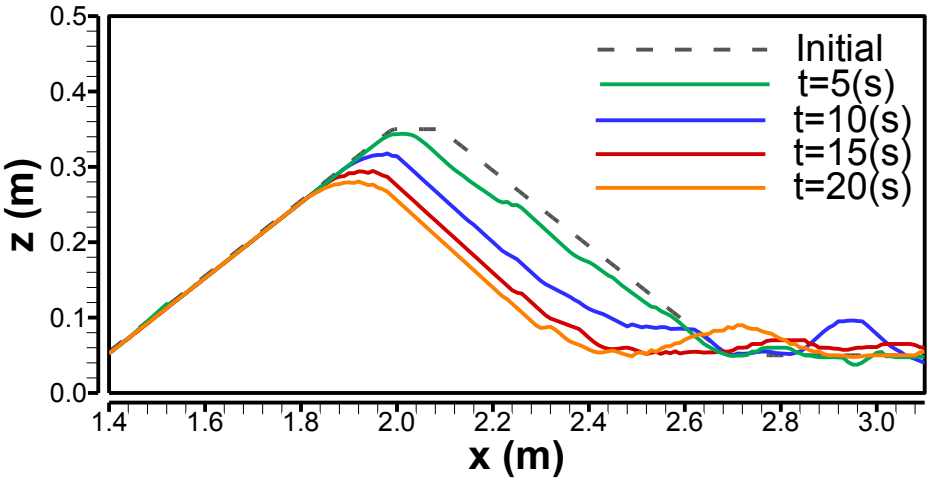

(a)

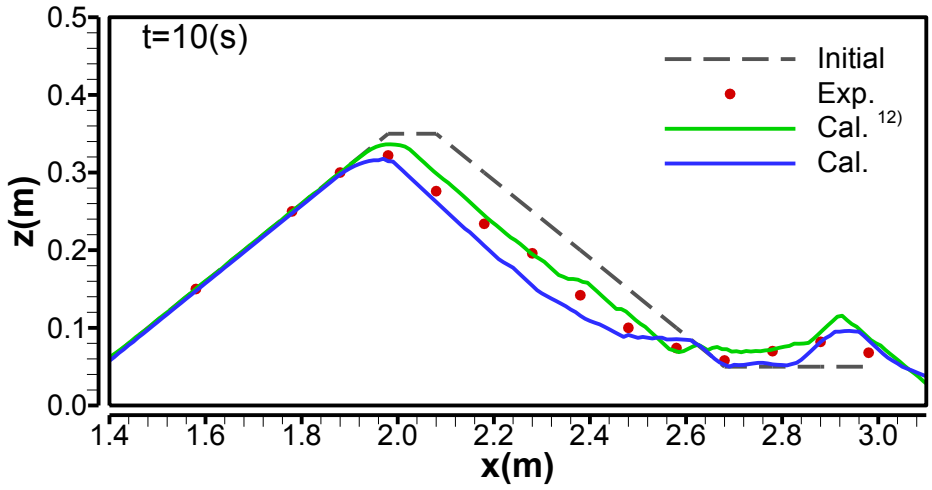

(b)

(Green line: Cartesian model Blue line: Curvilinear model)

Figure 5.12 Simulation results ((a) bed deformation with time progression and (b) t = 10 (s), (c) t = 15 (s) and (d) t = 20 (s) comparion of the dike defomation between the experiment and simulation)

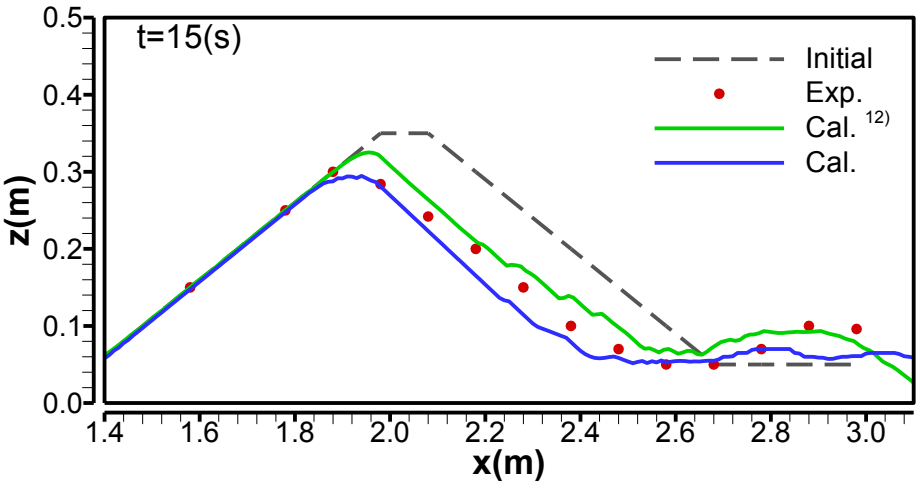

(c)

(Green line: Cartesian model Blue line: Curvilinear model)

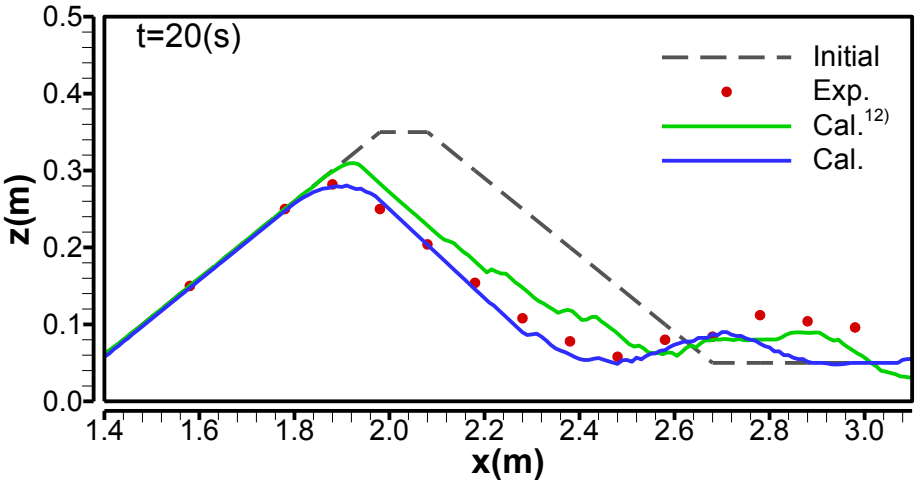

(d)

(Green line: Cartesian model Blue line: Curvilinear model)

Figure 5.12 Simulation results ((a) bed deformation with time progression and (b) t = 10 (s), (c) t = 15 (s) and (d) t = 20 (s) comparion of the dike defomation between the experiment and simulation)

5.4 Summary

This Chapter verifies the numerical model through its application to the bar formation in a meandering channel and dike breaching processes. The following are some conclusions derived from the study:

(1) This model, through precise simulation of surface flow and the secondary currents, successfully replicates the erosion and deposition observed in the experiment. Benefiting from the application of the 3D flow model, the secondary flows in meandering channels are more accurately replicated. It is observed that the erosion on the outer banks correspond well with experimental data, primarily due to the impact of these secondary flows, leading to significant erosion of the outer banks. On the other hand, while there is a slight discrepancy in the height of sediment accumulation compared to experimental results, the locations are consistent. When compared with existing 2D models[13], the 3D model exhibits improvements in accuracy.

(2) A fixed grid was employed to compute the dike failure, providing a better simulation of the flows on the dike surface during the initial period. Through accurately simulating the initial flow conditions, it has been observed that the erosion process at the top of the dike aligns closely with experimental results. Furthermore, the model successfully replicates the characteristic erosion pattern at the top, which progresses from slow to fast, with the erosion rate gradually decelerating after reaching its peak erosion rate. On the other hand, as the dike starts deformation, the mesh no longer completely fits the changing surface. Therefore, future studies should be conducted on the dike deformation process.

Reference

1) Hasegawa, K. : Hydraulic Study on the planform and bed configuration of meandering rivers and flow, *doctor thesis*, *Hokkaido University*, 1983. (in Japanese)
2) Colombini, M., Tubino, M. and Whiting, P. : Topographic expression of bars in meandering channels, *Third International Workshop on Gravel-Bed Rivers*, 1990.
3) Schmocker, L. and Hager, W. H. : Modelling dike breaching due to overtopping, *Journal of Hydraulic Research*, IAHR, Vol. 47, No. 5, pp. 585-597, 2009.
4) Schmocker, L. and Hager, W. H. : Plane dike-breach due to overtopping: effects of

sediment, dike height and discharge, *Journal of Hydraulic Research*, IAHR, Vol. 50, No. 6, pp. 576-586, 2012.

5) LaRocque, L. A., Elkholy, M., Chaudhry, M. H. and Imran, J. : Experiments on urban flooding caused by a levee breach, *Journal of Hydraulic Engineering*, ASCE, Vol. 139, No. 9, pp. 960-973, 2013.
6) Nishimoto, N., Shimizu, Y. and Aoki, K. : Numerical simulation of bed variation considering the curvature of stream line in a meandering channel, *Japanese Journal of JSCE*, Vol.1992, No. 456, pp. 11-20, 1992. (in Japanese)
7) Mizutani, H., Nakagawa, H., Yoden, T., Kawaike, K. and Zhang, H. : Numerical modelling of river embankment failure due to overtopping flow considering infiltration effects, *Journal of Hydraulic Research*, IAHR, Vol. 51, No. 6, pp. 681-695, 2013.
8) Kakinuma, T. and Shimizu, Y. : Large-scale experiment and numerical modeling of a riverine levee breach, *Journal of Hydraulic Engineering*, ASCE, Vol. 140, 04014039, pp. 1-9, 2014.
9) Zenno, H., Iwasaki, T., Shimizu, Y. and Kimura, I. : Computations of real scale experiment on levee breach with a 2D shallow flow model, *Proceedings of the 34th IAHR world congress*, IAHR, pp. 491-498, 2011.
10) Yu, M., Deng, Y., Qin, L., Wang, D. and Chen, Y. : Numerical simulation of levee breach flows under complex boundary conditions, *Journal of Hydrodynamics*, Vol. 21, No. 5, pp. 633-639, 2009.
11) Onda, S., Hosoda T., Jaćimović, N. and Kimura, I. : Numerical modelling of simultaneous overtopping and seepage flows with application to dike breaching, *Journal of Hydraulic Research*, IAHR, Vol. 57, No. 1, pp. 13-25, 2019.
12) Onda, S., Shimizu, K. and Yamaguchi, R. : Numerical Simulation of levee breaching due to overtopping flows considering suspended sediment, *Journal of Japan Society of Civil Engineers, Ser. B1 (Hydraulic Engineering)*, Vol. 77, No. 2, pp. 703-708, 2021. (in Japanese)
13) Kajikawa, Y. : Study on numerical analysis methods for localized scouring phenomena in rivers, *doctor thesis*, *Tottori University*, 2005. (in Japanese)
14) Colombini, M. : Revisiting the linear theory of sand dune formation, *Journal of Fluid Mechanics*, Vol. 502, pp. 1-16, 2004.

Chapter 6

Conclusions

6.1 Conclusions

In this study, a porous approach and a sediment transport model were developed based on the existing generalized curvilinear coordinate flow model, enabling the simulation of seepage flow and bed formation. Chapter 3 utilizes this model to explore the phenomenon of the side weir flow in both straight and curved channels; Chapter 4 delves into the dynamics of lateral seepage flow and dam break phenomena on a permeable bed, as well as open channel flow with bottom suction and open channel flow on a curved permeable bed; Chapter 5 discusses the formation of bars in meandering channels and the process of dike breaching. In the following, a summary of the discussions in each chapter and the insights derived from numerical analyses are presented, culminating in the conclusions of this study.

1. **Side Weir Flows in Open Channels**:

(1) In the context of the straight channel, simulations under three different experimental conditions were conducted. Case 1 has the widest weir width L= 0.2 (m) and a weir height of w = 2.5 (cm). Case 2, in comparison to Case 1, possesses half the weir width L= 0.1 (m). Case 3, relative to Case 2, is characterized by the absence of a weir height, with w = 0 (cm).

Upon comparing the simulation results of the three cases, a spiral flow in the latter half of the side weir can be observed in each case. This spiral flow is likely induced by the elevation of the water surface, leading to increased pressure and, consequently, the generation of flow under the action of a pressure gradient. Moreover, even in a straight channel, the presence of a side weir can give rise to secondary flows downstream of the weir, normally observed in curved channels.

(2) In the simulations of the curved channel, a total of 6 cases were examined. Cases 1, 2, and 3 share the same weir height of w = 3.5 (cm) but differ in their flow rates,

which are 0.0042 (m^3/s), 0.003 (m^3/s), and 0.002 (m^3/s), respectively. Cases 4, 5, and 6, on the other hand, feature a weir height of $w = 0$ (cm) with flow rates maintained consistently at 0.0042 (m^3/s), 0.003 (m^3/s), and 0.002 (m^3/s), aligning with the flow rates of Case 1, 2, and 3.

The Reynolds-Averaged Navier-Stokes (RANS) model demonstrated commendable proficiency in replicating water surface variations and flow velocity distributions observed in experiments. However, slight variations were observed in specific cases, notably near Section 3 in Case 6.

Despite these discrepancies, the model accurately reproduces the overflow rate's trend in relation to varying relative weir heights, emphasizing the substantial influence this height has on determining flow characteristics. For instance, a lower relative weir height ($w/B = 0$) showed a prominent formation of separation zones downstream, with the overflow's impact being particularly discernible in shaping secondary flows. Contrastingly, a higher relative weir height ($w/B = 0.175$) exhibited characteristics similar to single-bend flows, underscoring the importance of gravity as a driving factor.

In the domain of secondary flow dynamics within the side weir region, the structure of these flows is significantly influenced by the relative height of the weir. For greater relative weir heights, exemplified by $w/B = 0.175$, the secondary flow patterns both upstream and downstream, alongside the water surface profile adjacent to the lateral overflow, exhibit characteristics akin to those observed in single channel bend flows. Notably, this includes phenomena such as the superelevation at the outer bank. Variations in flow rate predominantly affect the velocity and extent of water surface superelevation but do not substantially alter the overall structure of the secondary flow. Conversely, in instances where the relative weir height is diminished to $w/B = 0$, there is a marked divergence in the behavior of secondary flows downstream when compared to those upstream, which remain largely unaffected by the change in weir height. Downstream, the intense overflow exerts a significant impact, constricting the secondary flows to a mere corner of the outer bank and preventing their extension toward the inner bank. This observation underscores the necessity to prioritize considerations of potential damage from lateral overflow to the weir structure over alterations in near-bed flows. Such findings delineate the

intricacies of flow dynamics near side weirs and illuminate the complex interplay between structural parameters and flow behavior.

2. **Flows Over Permeable Porous Beds**:

(1) This study presents a numerical model that adeptly simulates both surface and seepage flows upon a permeable porous bed, a capability corroborated by the congruence between the simulated water surface profiles and empirical observations. The integration of a porous media approach within the model facilitates the concurrent simulation of surface and seepage flows, thereby successfully delineating the substantial effect of seepage on the velocity distribution proximate to the permeable riverbed substrate.

(2) Furthermore, within the confines of a curved open channel where seepage flows are minimal, the model retains its predictive accuracy, offering reliable simulations of the intricate flow dynamics, as well as the attendant water surface contours and velocity distributions.

(3) The model's performance suggests that the role of suction, particularly within the context of infiltration processes through beds of fine sand a common component of natural riverbeds is of significant importance. Forthcoming research endeavors aim to refine the model by assimilating the impact of suction in unsaturated porous media, thereby augmenting the model's predictive precision.

3. **Bar Formation and Dike Breaching**:

(1) In the analysis of bar formation, this model replicated the typical sediment transport phenomena observed in meandering rivers, with sediment deposition forming bars on the outer banks and erosion occurring on the inner banks. A comparison with previous numerical results indicates that simulations utilizing this three-dimensional flow model combined with a two-dimensional sediment transport model yield better outcomes compared to those derived from two-dimensional flow models. This includes more accurate predictions of bar locations and erosion areas. This significant improvement is largely attributed to the three-dimensional flow model's enhanced capability to simulate the complex flow dynamics in meandering channels, thereby yielding more precise calculations of bed shear stresses.

(2) In the simulation of dike breaching phenomena, the utilization of curvilinear coordinates enabled the initial mesh to conform precisely to the surface shape of the dike. Additionally, the mesh near the surface could be refined as needed, allowing for a more accurate simulation of the initial flow over the dike slope. Comparison with experimental data demonstrates that the simulation effectively replicates the dike breaching phenomenon and the internal seepage processes within the dike. This is particularly evident in the simulation of the top erosion of the dike, which closely aligns with experimental observations. The simulation successfully captures the characteristic rapid erosion at the onset, followed by a gradual slowdown, a feature attributed to the variations in flow velocity at the dike's crest.

In conclusion, this research explores the multifaceted capabilities of the three-dimensional numerical model in addressing different hydrodynamic scenarios. While it excelled in several areas, the insights gained also paved the way for further refinements, promising even more accurate and comprehensive simulations in future hydrodynamic research.

6.2 Recommendation for future study

In the of simulating bar formation and dike breaching, this study has heretofore exclusively accounted for bed load sediment transport. The suspended load — sediment particles that are maintained in the river flow by the turbulent flow — has not been comprehensively integrated into the current model. During dike breaching experiments, a considerable quantity of sand is observed to be entrained at the berm, suggesting that the post-overflow morphology of the dike is significantly influenced by suspended sediments. Moreover, natural fluvial systems feature bed materials comprising various of grain sizes, many of which contribute to the suspended load. To enhance the model's accuracy and predictive capacity, the incorporation of a suspended load module is imperative.

Additionally, the treatment of turbulent kinetic energy k, dissipation rate ε, and shear stress within the riverbed and wall boundaries are currently addressed using wall functions. While this approach yields satisfactory results within the logarithmic layer, it

may not suffice as the computational cell center distances from the bed exceed the log layer, particularly during bed deformation. As such, alternative methodologies should be contemplated for the accurate computation of shear stress near the riverbed, thereby refining the numerical simulation's veracity.

Lastly, due to the current utilization of a fixed grid, the grid gradually ceases to conform to the terrain following deformation of the riverbed. Therefore, future research will contemplate modifying the grid at certain intervals to realign it with the evolving riverbed.